# Control techniques in spin based quantum computation

by

Hemant Katiyar

A thesis
presented to the University of Waterloo
in fulfillment of the
thesis requirement for the degree of
Doctor of Philosophy
in
Physics(Quantum Information)

Waterloo, Ontario, Canada, 2019

This thesis consists of material all of which I authored or co-authored: see Statement of Contributions included in the thesis. This is a true copy of the thesis, including any required final revisions, as accepted by my examiners.

I understand that my thesis may be made electronically available to the public.

## Statement of contribution

NOTE: Supervision and contribution from Prof. Raymond Laflamme should be assumed in all of the below. And contributors to the work with non-overlapping contributions with Hemant Katiyar are not mentioned.

1. Chapter 3

   - All the experiments were designed and performed by Hemant Katiyar(H.K.).
   - Error analysis and augmenting the inequalities were a collaborative effort by all the authors.

2. Chapter 4

   - H.K. Dawei Lu, Annie Park,Guanru Feng, and Hang li designed the control techniques used in the experiment.
   - H.K. designed the circuit for preparation of 12-qubit pseudo-pure state shown in Figure 4.3.
   - The classical simulation for the feasibility of the pulse sequence was performed by H.K. along with SSGRAPE pulses calculated for the experiments.
   - Testing of sample to gain Hamiltonian information was a collaborative effort of H.K., Dawei Lu, Annie Park,Guanru Feng, and Hang li.
   - Dawei Lu, H.K., Keren Li conceived the control technique of readout pulse sequence.

3. Chapter 5

   - Guanru Feng, Franklin Chao, H.K. conceived the idea of the experiment and designed the control techniques.
   - H.K. and Guanru feng suggested the idea of Slepian basis, thus reducing the number of gradient calculations.
   - H.K. performed part of the experiments.
   - H.K. proved that transfer function does not severely affect the optimization process on a quantum processor.

4. Chapter 6

- H.K. conceived the idea and performed the simulations (and to be performed experiment).

- H.K. along with Pooya Ronagh optimized the algorithm to be implemented.

- H.K. proved the theoretical results.

These work are published as

- Chapter 3 : Katiyar, Hemant, Aharon Brodutch, Dawei Lu, and Raymond Laflamme. "Experimental violation of the Leggett–Garg inequality in a three-level system." New Journal of Physics 19, no. 2 (2017): 023033.

- Chapter 4 : Lu, Dawei, Keren Li, Jun Li, Hemant Katiyar, Annie Jihyun Park, Guanru Feng, Tao Xin et al. "Enhancing quantum control by bootstrapping a quantum processor of 12 qubits." NPJ Quantum Information 3, no. 1 (2017): 45.

- Chapter 5 : Feng, Guanru, Franklin H. Cho, Hemant Katiyar, Jun Li, Dawei Lu, Jonathan Baugh, and Raymond Laflamme. "Gradient-based closed-loop quantum optimal control in a solid-state two-qubit system." Physical Review A 98, no. 5 (2018): 052341.

- Chapter 6 : Yet to be published.

**Abstract**

Working on quantum systems entail different interests, for example, working on fundamental understanding of quantum systems also lay foundation for better quantum computation techniques. A test for whether a system is behaving quantum mechanically or classically is devised by Leggett and Garg in form of inequalities, called Leggett-Garg Inequalities (LGI). Such Inequalities are violated by a system whose evolution is governed by quantum mechanics. A precise experiment to violate LGIs require a guarantee that the measurement does not affect the system or its future dynamics. These Inequalities were proposed for dichotomic systems,systems which can have two outcomes. Here we present an LG experiment on a three-level quantum system, which theoretically have larger quantum upper bound than that of a two-level quantum system. This larger violation also provides a bigger buffer to taking in account of the various experimental imperfections.

Performing a quantum computing task requires precise level of control to initialize, perform and measure the quantum system. With increasing size of the quantum processor the challenge is to maintain optimal control. Nuclear Magnetic Resonance (NMR) has always been a very faithful test-bed for quantum processing ideas. In NMR, we perform Radio Frequency (RF) pulses to control and steer the system to the desired state. Most used method to derive the exact frequency and amplitude of these pulses for a given task is based on gradient. Although systematic, one have to simulate these pulses on a classical computer first, which makes the task very inefficient. We report a a way of performing optimization with a hybrid quantum-classical scheme. This scheme helps us perform classically harder computational tasks on the quantum processor. We optimize pulses which drive our system from 7-coherence state to 12-coherence state on a 12-qubit NMR processor.

Electron Spin Resonance (ESR) employs the same techniques as of NMR but having advantage in larger polarization compared to later. Although this does not imply better control, cause the frequency at which pulses are required to control an ESR system fall into microwave region. Microwave frequency are harder to control electronically, thus making it harder for performing ESR quantum computing. The hybrid scheme used in NMR experiment relies on some ideal pulses which are needed to be optimized classically. We alleviate this requirement by using finite difference method of calculating gradient. We compare these methods with the earlier methods to show the superiority of such a scheme.

State-to-state transfer pulses are sufficient for most of the quantum computing task, but, an universal quantum information implementation requires state independent pulses. The techniques used in optimizing state-to-state pulses can be modified to optimize for a

state independent pulse. We show that this methods scale polynomially with the number of qubits and is general in terms of its implementation. We further reduce the resource requirement by using a NMR related implementation.

# Acknowledgments

First and foremost, I am very grateful to my supervisor Prof. Raymond Laflamme for his guidance, help and support throughout this degree. His approach during the degree of providing the complete independence in choosing the problem and the pace at which to solve them, has been a great education.

All persons are affected by their surrounding, even more if it offers them what they aspire. Working in the Ray's group has given me an opportunity to work with some really talented and hard-working individuals. I think with their company, I myself am becoming somewhat hard-working person, though I have been told it's hardly noticeable. Two people whom I will remain in debt are Dawei Lu and Gaunru Feng. I can say that they have been my unofficial co-supervisor, and were always there to bounce ideas or help. Discussing about experiments with Annie Park have always been fruitful. Franklin's knowledge of ESR hardware is of great help and an invaluable resource. Aharon Brodutch taught me how to look at experimental data differently. Taking reading courses with Brandon Buonacorsi helped a lot in ESR understanding. John Peterson's company and looking at problems very differently has been a learning experience. Pooya Ronagh's knowledge of machine learning has been a great resource.

I would like to thank IQC/Uwaterloo administrative staff for helping with all the paper work and queries, I especially thanks Judy McDonnell, Jeannie Bairos, Wendy Reibel and Jan Venne.

I thank Nayeli RB, Shayan Majidy, Michael Chen, JunAn Lin, Stefanie Beale, Marian Berek, for many discussions throughout the years. I am grateful to the friends in Waterloo I made as well as those back home and around the world.

Lastly, I would like to thank my parents and my sister for endless love and support.

# Table of Contents

# List of Tables

# List of Figures

# Chapter 1

# Introduction

Quantum mechanical system behave very differently from classical systems. Various phenomena of quantum regime does not show up when system scales to be in a classical regime. One such phenomena is superposition, everyday objects do not exist simultaneously in two different states. Schrödinger's cat [1], simultaneously dead and alive, is never seen in a classical world. Where is this point when going from microscopic objects to a macroscopic object the rules of quantum mechanics stop applying, and if there exists such macroscopic objects how can we demonstrate their presence. To answer the former, there is no known theoretical limit, for the latter, Leggett and Garg [2] formulated a test which can demonstrate presence of quantum behavior in macroscopic objects. They started by formulating a condition based on our intuition of everyday objects: *(i)* a classical system remains in one or the other well defined possible states, macroscopic realism, *(ii)* the measurement reveals this state without disturbing it or its future dynamics, non-invasive measurements. If a macroscopic system which satisfies the above criteria failed to conform to the conditions laid by Leggett and Garg, called Leggett-Garg inequalities(LGIs) it does not follow classical laws.

These LGIs take values between $-3$ and 1 for a classical system, but a quantum mechanical system can obtain a value as big as 1.5. It was believed that this maximal violation is independent of the number of macroscopically distinct states of the system due to the fact that the measurements are dichotomic. However, Budroni and Emary [3], showed that this is only true if the measurements follow the naive Lúders update rule. In a more general setting, it is possible to observe larger violations by going to higher dimensional systems, up to the algebraic maximum of 3.

An important requirement of performing these test is a guarantee that the measure-

ments do not disturb the system or its future dynamics, or in other words measurements are non-invasive. If they are not satisfied a skeptic can always appeal to them as the reason of violation. However, when an experiment of such a test is performed the violation is much smaller than the theory expects, which is fairly explained by decoherence and *slight* invasiveness of measurements. If one takes in account all the errors it becomes a very hard task to convince a skeptic that it is a *true* violation. This is where higher dimensional systems can be utilized, they have much higher theoretical violation and give a large buffer to explain all the experimental imperfections and thus we are left with a value which is inconceivable by classical systems. We perform such an experiment on a spin-1 system and achieve the highest violation of LGIs known to be achieved experimentally, to the best of our knowledge. The a rigorous error analysis follows to prove that we truly violate the LGIs. The hope is this will provide a gateway to a true test of LGIs where macroscopic systems are show to follow quantum behavior. This work is presented in chapter 3.

Next, we take a turn towards quantum information processing (QIP) tasks. QIP promises of speeding up various computing task as compared to a classical processor. Many examples of such a promise has already been demonstrated, most famous being, ability of efficiently factor large numbers. Gates are implemented in any quantum processor by controlling few variable parameters, for example, in a Nuclear Magnetic Resonance (NMR) system these variables are amplitude, frequency, and phase or the Radio Frequency (RF) pulses. To achieve a high fidelity gate an exact knowledge of these parameters are required. GRadient Ascent Pulse Engineering (GRAPE) has been the most used technique for getting these variables for a specific gate [4]. The drawback being the pulses have to be simulated on a classical computer to obtain the variables.

As we are constantly improving both theory and hardwares performances in QIP community, we need to control more and more number of qubits. Jun Li [5] came up with a method to perform the task of obtaining these variables on the quantum processor itself, thus greatly reducing the resources needed. The method of optimization on quantum processor doesn't also promises a relatively easier control for higher number of qubits, it also diminishes the pre-required knowledge of information needed. Such as some experimental imperfections are not needed to be characterized due to the procedure taking care of them by itself. We use this technique to drive a 12 qubit NMR processor to create a 12-coherent state, $Z^{\otimes 12}$. Our experiments is one of the few experiments with more than 10 qubit coherence observed, the previous ones being [6, 7, 8]. This work is presented in chapter 4.

Reforming the optimization on the quantum processor takes care of inaccuracies in our knowledge of the Hamiltonian. This becomes very useful when we perform these techniques on and Electron Spin Resonance (ESR) processor. An ESR system is highly attractive

prospects for QIP tasks, algorithmic cooling, a way to boost the polarization of the spin finds its ideal test bed in ESR. On the other hand an ESR processor is relatively harder to control then an NMR. In an ESR processor the frequencies of the pulses lie in the microwave region. Microwaves are harder to control electronically, resulting in limiting bandwidth of the resonator. Hence a transfer function, which can be understood as a function which maps the applied pulses to the pulses seen by the quantum processor, plays a vital role in designing pulses. An accurate knowledge of the transfer function is required if one wants to simulate the control parameters on the classical computer. This limitation can be waived depending on how the transfer function behaves. Jun Li's [5] method, though ground breaking, requires some local rotation pulses optimized on a classical processor which requires perfect knowledge of Hamiltonian. Another method proposed in [9], utilized finite difference to calculate the gradients for optimization procedure. We utilize these methods and provide an overview and comparison of how they behave experimentally. Although, 2 qubits may sound a small number of qubits, its really hard to control them in ESR systems, mainly due to imperfect knowledge of Hamiltonian, presence of a transfer function, high bandwidth control needed. We perform an experiment on a 2 qubit processor (one electron-one nucleus) and compare the two methods (closed loop and open loop) of obtaining a desired state from an initial state. This work is presented in chapter 5.

Finding pulse that takes some initial state to a desired final state is enough for many QIP tasks, for example algorithmic cooling only requires state-to-state pulses. But, a universal quantum computing requires gates which can perform independent of the state. With the inspiration of performing an optimization on a quantum processor itself we ask the question whether it is possible to perform an optimization involving finding a quantum gate rather that a state-to-state gate. In first look, it seems an exponentially hard and not experimentally feasible problem for higher number of qubits. A state independent quantum gate can be found as a state-to-state pulse which performs correct state to state transfers for all the elements of the basis, which grows exponentially with the number of qubits. However, if we take advantage of the Pauli matrix algebra the number of experiments grows polynomially. We present these finding in chapter 6.

3

# Chapter 2

# Backgrounds

## 2.1 Introduction to Nuclear Magnetic Resonance quantum computing

A nuclei having non-zero spin result in energy splitting when placed in an external magnetic field, this effect is called the Zeeman effect. Most common nuclei used for Nuclear Magnetic Resonance (NMR) quantum information processing(QIP) are spin-1/2, resulting in 2 energy levels, which can be encoded as $|0\rangle$ and $|1\rangle$ analogous to $0, 1$ in a classical computer. In this chapter, we describe the dynamics of spin-1/2 nuclei. Techniques of NMR were well known before we started using its for QIP tasks, which makes the characterization of molecules for the computing purposes a relatively easier task. Moreover, the principles of other spin-based techniques can be understood by a good understanding of NMR. In the following section we will briefly describe the basics of NMR QIP.

### 2.1.1 Hamiltonian

The magnetic moment of the nuclei interact with the external magnetic field resulting in the energy level splitting. The magnetic moment of a nuclear spin is,

$$\vec{\mu} = \gamma \vec{I} \tag{2.1}$$

where , $\gamma$ is the gyromagnetic ratio of the nucleus and $\vec{I}$ is the spin angular momentum operator. The exact form of the operator is,

$$I_i = \frac{\hbar}{2}\sigma_i, \tag{2.2}$$

where, $\sigma_i$ are Pauli matrices and $i \in$ x,y,z.

The Zeeman Hamiltonian or the interaction of nucleus with an external Magnetic field, $\vec{B}$ is given by,

$$H_{Zeeman} = -\vec{\mu} \cdot \vec{B'} \tag{2.3}$$

Here, $\vec{B'}$ is the magnetic field that the nuclei sees. These differ from the external magnetic field slightly due to the fact that nucleus is surrounded by an electron cloud and they shield the nuclei, also if multiple spins are presents the magnetic field due to electron clouds of the other nuclei also affect the local magnetic field. We can write $\vec{B'} = (1+\Delta)\vec{B}$ where $\Delta$ represents a variation from the external magnetic field to local felt. From eq. 2.1 and 2.2 in the units of $\hbar$, we can write,

$$H_{Zeeman} = -\gamma(1+\Delta)\vec{I} \cdot \vec{B} \tag{2.4}$$

In a typical NMR setup the external magnetic field is applied along the $\hat{z}$ direction, *i.e.* $\vec{B} = B_0\hat{z}$. This implies we can write Zeeman interaction as,

$$H_z = -\gamma(1+\Delta)B_0 I_z = -\omega_0 I_z \tag{2.5}$$

where, $\omega_0$ is called the precession frequency or the Larmor frequency.

Nuclear spins inside a molecule are coupled together through chemical bonds, the coupling is a result of interaction of bonding electrons with the nucleus magnetization. It is an indirect coupling mediated through the electrons, and thus depends upon the bond length, angle. It is often termed as indirect spin-spin coupling or J-coupling and for 2 spins coupled with a strength, $J$ is written as

$$H_J = 2\pi J\vec{I^1} \cdot \vec{I^2}. \tag{2.6}$$

Where the superscripts denote the Spin angular momentum operator for different nuclei. Using the above information one can write the total Hamiltonian for N spin NMR system as [10],

$$H_0 = -\sum_{k=1}^{N} \omega_0^k I_z^k + 2\pi \sum_{i,j=1:N,i<j} J_{ij} \vec{I^i} \cdot \vec{I^j} \tag{2.7}$$

The dipole-dipole interactions averages to zero in a liquid state due to rapid tumbling of the molecule. In the weak coupling regime, when the difference in the Larmor frequency is much bigger than J coupling between them we can approximate, $\vec{I_i} \cdot \vec{I^j} = I_z^i I_z^j$, which is valid for molecules used in this thesis.

The control is achieved by applying the magnetic field (which results in pulses in radio frequency regime) in $\hat{x}$ and $\hat{y}$ direction. The control Hamiltonian on the $i$th nuclei is then written as,

$$H_{ext}^i = \omega cos(\omega_0 t + \phi)I_x + \omega sin(\omega_0 t + \phi)I_y \tag{2.8}$$

where, $\omega$ is propotional to the stregth of Magnetic field in $\vec{x}, \vec{y}$ direction, The control Hamiltonian in rotating frame, (rotating at the Larmor frequency) is [10],

$$H_{ext}^i = \omega cos(\phi)I_x + \omega sin(\phi)I_y. \tag{2.9}$$

Using specifically defined pulse sequence we can selectively turn "off" parts of the internal (eq. 2.7) and external (eq. 2.9) Hamiltonian. This enables us to apply rotation in any direction or a controlled-$z$ rotation. Thus providing a way of universal quantum computing. In practice, as the number of spins increases the selective control becomes harder [11, 12].

*Homonuclear and Heteronuclear molecule* - If all the nuclei are of same chemical species the sample is homonuclear, if the molecule consists of more than one type the sample is heteronuclear. Since the different nuclei of a heteronuclear molecule have Larmor frequency which are far, the different species of nuclei can be controlled separately. This increases the control potential of the molecule.

*Concentration of the sample* - The desired molecule is dissolved in solvent, usually an organic compound with hydrogen replaced with deuterium. The solvent serves the purpose of locking the sample, the lock monitors the Larmor frequency of deuterium and adjust the current in the superconducting coil to maintain a fixed frequency. Solvent also help dilute the sample, which is necessary since a highly concentrated sample result in a phenomena called radiation damping [13].

## 2.1.2 Initial state

Boltzmann distribution for an ensemble of spins gives, the number of spins in an energy state, E at the temperature T [10], by

$$exp(-E/k_BT)/Z \tag{2.10}$$

where $k_B$ is the Boltzmann constant, and $Z$ is the partition function. That implies, the equilibrium density matrix can be written as,

$$\rho_{eq} = exp(-H_0/k_BT)/Tr(exp(-H_0/k_BT)), \tag{2.11}$$

where, $H_0$ is the internal Hamiltonian as defined in eq. (2.7). In high temperature, $E \ll k_BT$, we can approximate $\rho_{eq}$,

$$\begin{aligned}
\rho_{eq} &= exp(-H_0/k_BT)/Tr(exp(-H_0/k_BT)) \\
&\approx (\mathbb{1} - H_0/k_BT)/Tr(\mathbb{1} - H_0/k_BT) \\
&\approx \mathbb{1}/N - H_0/Nk_BT.
\end{aligned} \tag{2.12}$$

The first part is identity and any unitary application will not change it, so most of the time we work with non-identity part of the density matrix, termed as deviation density matrix, $\rho_\Delta$

$$\rho_\Delta = -\frac{H_0}{Nk_BT} = -\sum_{k=1}^{N} \frac{\hbar\omega_0^k}{Nk_BT} I_z^k. \tag{2.13}$$

*Pseudo Pure state :*  The thermal equilibrium state can be transformed to a pseudo-pure state through non-unitary processes using standard NMR techniques of temporal or spatial averaging [14, 15] :

$$\rho_{pps} = (1 - \epsilon)\mathbb{1} + \epsilon\rho_{pure} \tag{2.14}$$

where , $\rho_{pure}$ represents a pure density matrix. So in reality the state for NMR systems is a mixed state but one can ignore the identity part since it doesn't evolve and we can solely focus on the deviation part.

## 2.1.3 Measurements

NMR is an ensemble quantum computing technique, the reason being the magnetic moment of a single spin is not measurable directly with the current NMR instruments, however,

many identical copies of the spins are present in a sample and the magnetic moment of this ensemble is measurable. When the magnetic moments of these identical spins are rotated to $x - y$ plane, it start precessing around the external magnetic field (in $z$ direction). The precessing moments induce current in the coil that has is axis in $x - y$ plane. This magnetization is expressed as the expectation values of observables in $x - y$ direction

$$M_{x(y)}(t) \propto e^{(-t/T_2^*)} Tr(\rho(t)\sigma_{x(y)}) \tag{2.15}$$

This signal is referred as Free Induction Decay (FID) and a NMR spectrum is obtained by the Fourier transform of this signal. The signal decay with time due magnetic field inhomogeneities and intrinsic relaxation ($T_2$).

## 2.2 Introduction to electron spin resonance quantum computing

The Electron Spin Resonance (ESR) quantum computation is very similar to NMR case, an electron placed in a magnetic field undergoes splitting in the energy levels. But there are some extra terms in the Hamiltonian as compared to previously described liquid state NMR. From here on we will describe the Hamiltonian of a coupled system consisting of an electron and a nuclei.

### 2.2.1 Hamiltonian, states and measurement

The Zeeman interaction term similar to nuclei case, for an external magnetic field applied in the $\hat{z}$ direction is written as $H_{Zeeman} = \mu_b \mathbf{g} B S_z$, where $S_z$ is the angular momentum operator conventionally represented by $S$ for electron and by $I$ for nuclei. $\mathbf{g}$ is the electron g-factor and is represented by 2nd rank tensor, since it depends on the orientation of molecule with respect to external magnetic field.

The Hyperfine interaction between the electron and the nuclear spin is described as [16],

$$H_{HF} = \vec{S} \cdot \mathbf{A} \cdot \vec{I}, \tag{2.16}$$

where $\mathbf{A}$ is the hyperfine tensor. The hyperfine coupling have two contributions, isotropic part, which comes from electron spin density at the nucleus, and anisotropic part, which is a result of electron-nuclear dipole-dipole interaction.

Therefore total Hamiltonian of an electron coupled to a spin-1/2 nuclei with isotropic $g$ tensor and anisotropic hyperfine coupling can be written as [16],

$$
\begin{aligned}
H &= \omega_S S_z + \omega_I I_z + \vec{S} \cdot \mathbf{A} \cdot \vec{I} \\
&\approx \omega_S S_z + \omega_I I_z + A S_z I_z + B_x S_z I_x + B_y S_z I_y,
\end{aligned}
\tag{2.17}
$$

where $A = A_{zz}, B_x = A_{zx}$, and $B_y = A_{zy}$. The second line on the above equation we make a secular approximation thus neglecting $S_x$ and $S_y$ terms. Without any loss of generality a unitary transformation with $exp(-i\phi I_z)$ where, $\phi = arctan(-B_y/B_x)$ can be applied which defines a new x-axis for the nuclei subspace,

$$
H = \omega_S S_z + \omega_I I_z + A S_z I_z + B S_z I_x
\tag{2.18}
$$

with $B = \sqrt{(B_x^2 + B_y^2)}$, This Hamiltonian can be diagonalized with the unitary transformation produced by,

$$
U = exp(-i(\xi I_y + \eta 2 S_Z I_y))
\tag{2.19}
$$

where, $\xi = (\eta_\alpha + \eta_\beta)/2$ and $\eta = (\eta_\alpha - \eta_\beta)/2$. $\eta_\alpha$ and $\eta_\beta$ are the angles defining the two nuclear quantization axis with respect to external magnetic field with $\alpha, \beta$ representing lower and higher energy respectively, and are given by,

$$
\eta_\alpha = \arctan\left(\frac{-B}{A + 2\omega_I}\right) \quad \& \quad \eta_\beta = \arctan\left(\frac{-B}{A - 2\omega_I}\right).
\tag{2.20}
$$

This results in diagonal Hamiltonian,

$$
H^d = \omega_S S_z + (\omega_+/2) I_z + (\omega_-/2) 2 S_z I_z
\tag{2.21}
$$

where, $\omega_\pm$ are the addition and subtraction of nuclear frequencies. Explicitly, the four eigenstates are [16],

$$
\begin{aligned}
|1\rangle &= \cos\left(\frac{\eta_\alpha}{2}\right)|\alpha\alpha\rangle - \sin\left(\frac{\eta_\alpha}{2}\right)|\alpha\beta\rangle \\
|2\rangle &= \sin\left(\frac{\eta_\alpha}{2}\right)|\alpha\alpha\rangle + \cos\left(\frac{\eta_\alpha}{2}\right)|\alpha\beta\rangle \\
|3\rangle &= \cos\left(\frac{\eta_\alpha}{2}\right)|\beta\alpha\rangle - \sin\left(\frac{\eta_\alpha}{2}\right)|\beta\beta\rangle \\
|4\rangle &= \sin\left(\frac{\eta_\alpha}{2}\right)|\beta\alpha\rangle + \cos\left(\frac{\eta_\alpha}{2}\right)|\beta\beta\rangle
\end{aligned}
\tag{2.22}
$$

The two nuclear frequencies can be expressed as,

$$\omega_{12} = \left(\omega_I + \frac{A}{2}\right)\cos\eta_\alpha - \frac{B}{2}\sin\eta_\alpha$$
$$\omega_{34} = \left(\omega_I - \frac{A}{2}\right)\cos\eta_\beta + \frac{B}{2}\sin\eta_\beta \tag{2.23}$$

Thus, $\omega_{pm} = \omega_{12} \pm \omega_{34}$. The four eigenvalues corresponding to the eigenstates in eq. 2.22 are,

$$\begin{aligned}
\epsilon_1 &= \frac{\omega_S}{2} + \frac{\omega_{12}}{2} \\
\epsilon_2 &= \frac{\omega_S}{2} - \frac{\omega_{12}}{2} \\
\epsilon_3 &= -\frac{\omega_S}{2} + \frac{\omega_{34}}{2} \\
\epsilon_4 &= -\frac{\omega_S}{2} - \frac{\omega_{34}}{2}.
\end{aligned} \tag{2.24}$$

### 2.2.2 Initial state

The thermal state, similar to NMR case is given by Boltzmann distribution, That implies, the equilibrium density matrix can be written as [16] ,

$$\rho_{eq} = exp(-H/k_BT)/Tr(exp(-H/k_BT)). \tag{2.25}$$

In high temperature, $E \ll k_BT$, we can approximate $\rho_{eq}$,

$$\begin{aligned}
\rho_{eq} &= exp(-H/k_BT)/Tr(exp(-H/k_BT)) \\
&\approx (\mathbb{1} - H/k_BT)/Tr(\mathbb{1} - H/k_BT) \\
&\approx \mathbb{1}/N - H/Nk_BT.
\end{aligned} \tag{2.26}$$

where $H$ is given by eq. (2.18). The first term in eq. (2.18) dominates due to electron gyromagnetic ratio being much bigger than that of a nuclei ($|\gamma_e| \approx 700\gamma_H, |\gamma_e| \approx 2800\gamma_C$). Thus,

$$\rho_{eq} \approx \frac{\mathbb{1}}{N} - \frac{1}{Nk_BT}H = \frac{\mathbb{1}}{N} - \frac{\hbar\omega_S}{Nk_BT}S_z \tag{2.27}$$

The deviation density matrix similar to NMR is , $\rho_\Delta = -S_z$. The measurements are similar to the NMR system measuring the expectation values of $x, y$ Pauli operators.

# Chapter 3

# Violation of Leggett-Garg Inequality in 3-level system

## 3.1 Introduction

Part of what makes quantum mechanics so exciting and unbelievable is that macroscopic objects do not show the properties that is exhibited by the microscopic objects. One such property being superposition, which loosely speaking states objects can be in two different states at any point in time. We do not see such a thing in macroscopic world but microscopic entities like photons, electrons, nuclei etc. are superimposed. There is, however, no known theoretical limit on the size of objects that can be observed in an arbitrary superposition of two states and it is conceivable that we will one day be able to isolate large objects from the environment, such that they can be in what we may call a macroscopic superposition state(macroscopic coherence). The Leggett-Garg (LG) experiment [2] and some extensions [17, 18] allow us to test the assumption that a given system confined to a discrete set of *classically observable* states is never in a superposition of these states. The experiment leads to an inequality that, under some reasonable assumptions, cannot be violated when the system is in a definite classically observable state at all times, but can be violated when it is superposition of these states.

Unlike Bell's inequality, the assumptions regarding the Leggett-Garg inequality (LGI) depend on the physical system and the experimental setup. Of the three fundamental assumptions: (A1) macroscopic realism (MR): *the system cannot be in a superposition of the classically observable state*, (A2) non-invasive measurability (NIM): *It is possible to measure the macroscopic system without disturbing it*, and (A3) induction: *the future*

*cannot influence the past*, only the last is independent of the experimental setup. The LGI is therefore a test of MR under a set of reasonable assumptions about the system, in particular a version of NIM. The violation of the inequality leads to the conclusion that either MR or one of the other assumptions is incorrect [19]. The aim of a well-designed experiment is therefore to convince a skeptic that the incorrect assumption is probably MR, i.e. the system is in a superposition of classically observable states sometime during its evolution.

One way to avoid invasive measurements is to use ideal negative result measurement (INRM). In an INRM the detector registers a 'click' if the system is in one specific state, otherwise it does not interact with the system. If the detector clicks, the result is discarded, if it does not click, we infer that the system is in the orthogonal subspace and keep the result. The assumption is that a probe cannot influence the system unless they interact. By keeping only the negative (no click) results we can then enforce NIM.

In the standard LG experiment a parameter $K_3$ is classically constrained to take values between $-3$ and $1$, whereas quantum mechanics predicts possible violations of up to $1.5$, giving a narrow margin for experimental errors. It has recently been noted [18, 20] that in order to convince a skeptic that the reasonable assumptions are indeed reasonable, the assumptions need to be tested and the inequality must be adjusted accordingly. Consequently the margin for error gets reduced even further. Until recently it was believed that the maximal violation of $K_3$ is independent of the number of possible macroscopically distinct states of the system due to the fact that the measurements are dichotomic. However, Budroni and Emary [3] showed that this is only true if the measurements follow the naive Lüders update rule. Lüders update rule states that a system with degenerate eigenstates is unaffected by the measurement thus the system remains in superposition after the measurement [21]. In a more general setting, provided by Von Neumann, where such a superposition is not preserved [22], it is possible to observe larger violations by going to higher dimensional systems, up to the algebraic maximum of 3. While such measurements give a bigger margin for errors, it was not clear how to construct them using INRMs.

Various experimental violations LGI have been performed [23, 24, 25, 26, 27, 28, 29, 30, 31, 32, 33, 34, 35, 36] on two level systems. INRMs were used to perform non-invasive measurements in [33, 34, 35]. Knee et al. [33] performed the first experiment where the LGI was modified to include imperfections in the (quantum) measurement device. George et al. [36] performed the first test of realism (albeit, not macroscopic) that also included a test of measurement disturbance. Their main result was a demonstration of the three box game, a pre and post selection paradox that can be used to violate a LGI. Theirs was also the first experiment to violate a LGI on a three level system, however unlike our experiment their measurement scheme followed the Lüders update rule and had a theoretical upper

bound of $K_3 \leq 1.44$. Moreover, their measurements were not INRMs. The assumptions that go into experiments of this type were discussed in [19]. A modification of Leggett-Garg experiment, depending on the measurement distribution was recently introduced in [18]. To the best of our knowledge our experiment and one in [18] are the only Leggett-Garg experiments where the LGI is corrected for the measurement disturbance.

In this work we demonstrate the first violation of the LGI with an experiment that has a theoretical bound beyond $K_3 = 1.5$. We present results of a set of experiments performed on an ensemble of 3-level systems in liquid-state nuclear magnetic resonance (NMR) and provide a natural method for performing the experiment using INRMs. The inequality is corrected for a number of non trivial assumptions about the state of the systems and the measurement device, in particular the LGI is corrected to account for non ideal measurements.

## 3.2   The Leggett-Garg test.

Consider a system which is evolving under certain Hamiltonian. We decide to perform dichotomic measurements of an observable $Q$, at some time $t_i$ represented as $Q_i$, that can perfectly distinguish between two states of a system. The outcomes of these measurements are denoted as $q_i^{(1)} = +1$ and $q_i^{(2)} = -1$. In a macrorealistic system, the outcomes $q_i^{(l)}$ ($l = 1, 2$, the dichotimic outcomes) represent the *real* state of the system, i.e. if the result was $q_i^{(l)}$ we can infer that the system was in the state corresponding to $q_i^{(l)}$ at time $t_i$. A test of macrorealism is a test of this hypothesis. For LG test, one chooses three distinct times to perform a measurement and three independent experiments. In each of the three experiments we start with the same state, and then perform measurements on two of the three chosen times as shown in Fig. 3.1. These three independent experiments are performed many times to estimate the probabilities of being in different possible states. Using these probabilities one can calculate the two time correlations of the measurements,

$$C_{ij} = \sum_{l,m} q_i^{(l)} q_j^{(m)} P(q_i^{(l)}, q_j^{(m)}),$$

(3.1)

where $q_i^{(l)}$ ($l = 1, 2$) means the $l^{th}$ outcome of measurement performed at $t_i$.

The 3-measurement LG string is

$$K_3 = C_{12} + C_{23} - C_{13}.$$

(3.2)

13
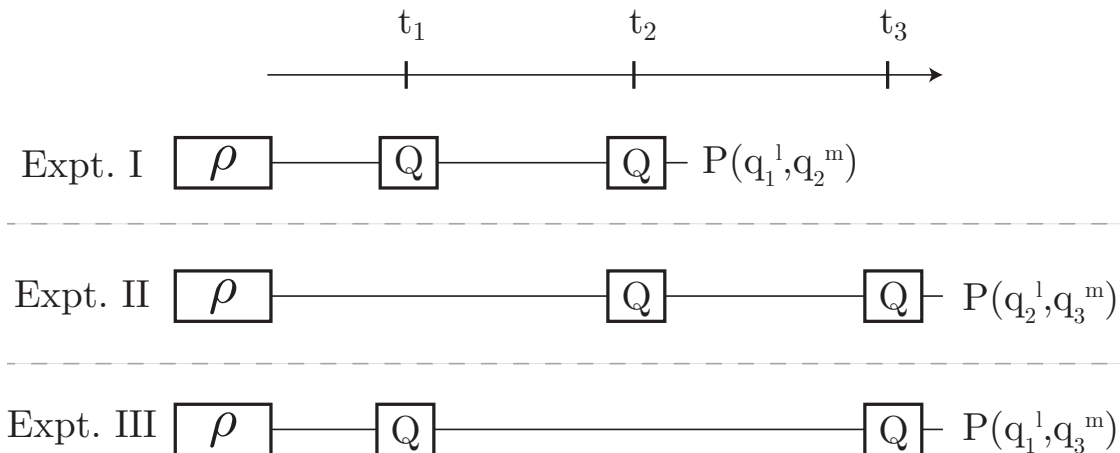
Figure 3.1: Scheme for LG test. Three experiments are performed such that in each experiment the dichotomic observable $Q$ is measured at two different times. The experiments are performed many number of times to obtain the probabilities for the correlations and anti-correlations between two measurements. The results are used to calculate the LG string in Eq. (3.2).

If we assume that the measurements do not disturb the system (NIM assumption) and the system is classical (i.e. macrorealistic), the value of $K_3$ is bounded by $-3 \leq K_3 \leq 1$. On the other hand, if the system is quantum it is possible to choose the evolution times between measurements in such a way that $K_3$ will go beyond 1, violating the LGI that $K_3 \leq 1$. The quantum bound for $K_3$ is 1.5 for a 2-level system [17]. More general systems have the same bound if the measurements follow the Lüders update rule which is natural for these types of experiments. According to the Lüders rule the dichotomic measurement projects the state of the system into one of two orthogonal subspaces corresponding to the $\pm 1$ measurement results. While this projection is invasive when the system is quantum, it is theoretically non-invasive if we assume MR. In performing the LG test, we must however consider the possible objection of a skeptic who may object to our assumption that the measurement indeed follows the Lüders rule. To counter such an argument, LG suggested that the experiment is carried out using ideal negative result measurements (INRMs). INRMs are implemented by measuring the system at a given time ($t_i$), and asking the question whether the system is in a particular state (say that state corresponds to $q_i^{(1)} = +1$). If the answer is no, we confirmed that the system is in the other state, thus gaining the information of the state of the system with interacting with it. This post-

selecting on negative outcomes is what allow us to infer the state of the system, e.g. by finding that the system is not in a $q_i^{(1)} = +1$ state we infer that it must be in a $q_i^{(2)} = -1$ state.

The original LG test considered only 2-level systems. Recently Budroni and Emary [3] showed that if one relaxes the assumption that the measurement follows the Lüders update rule, and instead one allows a more general update rule which also destroys some of the phase information within the $\pm 1$ subspaces, then the quantum bound on $K_3$ could be extended to a value that depends on the dimension of the system, and goes asymptoticly to the algebraic maximum of 3. For a 3-level system, such measurements can lead to the value $K_3 = 1.7566$, when the observable $Q = -|0\rangle\langle 0| + |1\rangle\langle 1| + |2\rangle\langle 2|$ and the measurement acts like a complete dephasing channel. However, the channel seems to be more invasive than necessary and can raise questions about the validity of NIM. For example in an INRM the update rule for a negative result on the state $|0\rangle$ would project the system into the $|1\rangle, |2\rangle$ subspace without dephasing, following the Lüders rule. The proposal in [3] would require an additional dephasing step. In such a case, it is harder to justify the violation of the LGI as a violation of MR. However, as we show below, the channel can be implemented using INRMs.

## 3.3 Measuring the Probabilities using INRMs.

The scheme for performing the modified LGI measurement is based on using three INRMs, one for each of the possible states. The measurement is registered on an ancillary qubit initially in the state $|0\rangle$. When performing the INRM of the system state $|j\rangle$, the ancilla remains in the state $|0\rangle$ if the system is in $|j\rangle$ and rotates to $|1\rangle$ otherwise[1]. The three gates below correspond to the three types of measurements.

$$\mathrm{CG}_0 = |0\rangle\langle 0| \otimes \mathbb{1} + |1\rangle\langle 1| \otimes X + |2\rangle\langle 2| \otimes X, \tag{3.3}$$

$$\mathrm{CG}_1 = |0\rangle\langle 0| \otimes X + |1\rangle\langle 1| \otimes \mathbb{1} + |2\rangle\langle 2| \otimes X, \tag{3.4}$$

$$\mathrm{CG}_2 = |0\rangle\langle 0| \otimes X + |1\rangle\langle 1| \otimes X + |2\rangle\langle 2| \otimes \mathbb{1}. \tag{3.5}$$

---

[1]Note that these INRMs are only ideal if one trusts the quantum mechanical description of the gates

Consider, for example, the application of $CG_0$ on the following general state of system and ancilla being in state $|0\rangle$

$$
\begin{bmatrix} P_0 & a & b \\ a^\dagger & P_1 & c \\ b^\dagger & c^\dagger & P_2 \end{bmatrix}_S \otimes \begin{bmatrix} 1 & 0 \\ 0 & 0 \end{bmatrix}_A \xrightarrow{CG_0} \begin{bmatrix} P_0 & a & 0 & 0 & 0 & b \\ a^\dagger & 0 & 0 & 0 & 0 & c \\ 0 & a & 0 & 0 & 0 & 0 \\ 0 & 0 & 0 & P_1 & 0 & 0 \\ 0 & a & 0 & 0 & 0 & 0 \\ b^\dagger & c^\dagger & 0 & 0 & 0 & P_2 \end{bmatrix}_{SA} ,
$$

where $a, b$ and $c$ are the off-diagonal elements of the system's density matrix. The diagonal elements of the ancilla after tracing out system are $P_0, P_1 + P_2$. Thus we can measure $P_0$ non-invasively. Similarly for $CG_1$ and $CG_2$ after the similar procedure, the diagonal elements of ancilla are $P_1, P_0 + P_2$ and $P_2, P_0 + P_1$ respectively, which enables a way of measuring $P_1$ and $P_2$ non-invasively. The measurement at the end of the experiment is not required to be non-invasive since we are not worried about the future dynamics of the system. After the second evolution of the system, we measure the diagonal elements of the combined ancilla and system state. The elements corresponding to state $|00\rangle_{SA}, |10\rangle_{SA}$, and $|20\rangle_{SA}$ are post-selected. These elements correspond to probabilities, $P(i,0)$, $P(i,1)$, and $P(i,2)$ respectively when $CG_i$ gate is applied, where $i = 0, 1, 2$ corresponds to the three states of the system.This scheme is illustrated in Fig. 3.2.

Each single measurement described above follows the Lüders update rule. However, since we are post-selecting, we end up with only part of the quantum channel (i.e. a subchannel) that corresponds to the negative result. i.e for each qubit-qutrit channel in eqs 3.3-3.5 we prepare the ancilla in the $|0\rangle$ state and post select it in the $|0\rangle$ state to produce a subchannel represented by a Krauss operator $\mathbb{K}_i = |i\rangle\langle i|$. Adding the three subchannels that we post-select on, effectively creates a measurement that does not follow the Lüders update rule. Instead the effective trace-preserving channel that describes the evolution during the measurement is represented by $\mathbb{K}_i$. Nevertheless the measurement is an INRM.

## 3.4   Experimental implementation and results.

The experiments are carried out at the ambient temperature on a Bruker DRX 700MHz NMR spectrometer. As described earlier, a spin-1 system and a spin-1/2 ancilla are needed to perform the non-invasive measurements. In the experiments, we use two spin-1/2 nuclei
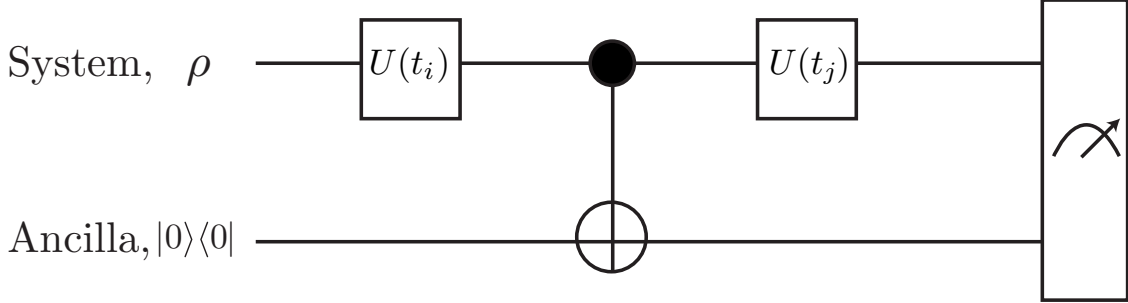
Figure 3.2: General Scheme for a single run of the LG test with an INRM. We start with the system in some state $\rho$ and ancilla in $|0\rangle\langle 0|$. The two evolution times $t_i$ and $t_j$ depend on which of the three experiments is performed (see Fig. 3.1). The controlled gates are the ones given in eqs 3.3, 3.4, and 3.5, are the first measurement performed (one of three possible INRMs), and it is non-invasive if nothing happens, i.e the state of the ancilla is unchanged. The last measurement is not necessarily non-invasive since we are not concerned about the future dynamics of the system. The results are post-selected to include only the instances when the INRM was successful, i.e. the situations where the ancilla is in the state $|0\rangle\langle 0|$. For each measurement setting in Fig. 3.1, we perform three runs, one for each state of the system.

to simulate the dynamics of the spin-1 system via the Clebsch-Gordan approach [37], which transforms a space consisting of two spin-1/2 particles to another space consisting of one spin-1 and one spin-0 particle. This transformation defining the spin-1 in terms of two spin-1/2 particles are (triplets) $|0\rangle_s = |00\rangle$, $|1\rangle_s = (|01\rangle + |10\rangle)/\sqrt{2}$, and $|2\rangle_s = |11\rangle$, as well as the spin-0 (singlet) state $|s\rangle = (|01\rangle - |10\rangle)/\sqrt{2}$. This basis for convenience will be called triplet-singlet (TS) basis and we employ TS basis notation to describe the system state unless otherwise specified.

Therefore, we need three qubits to implement the experiment. The sample is chosen as $^{13}$C-labeled trans-crotonic acid dissolved in acetone-d6. The molecular structure, Hamiltonian parameters and the relaxation times ($T_1$ and $T_2$) are shown in Fig. 3.3, where $C_2$ and $C_3$ are used to simulate the dynamics of the spin-1 system and $C_4$ as the ancilla. The spatial averaging method [38] is adopted to initialize the 3-qubit NMR system into the pseudo-pure state (PPS)

$$\rho_{pps} = \frac{1-\epsilon}{8}\mathbb{I} + \epsilon|0\rangle\langle 0|_s \otimes |0\rangle\langle 0|, \tag{3.6}$$

17

|     | C1     | C2     | C3     | C4     |
| --- | ------ | ------ | ------ | ------ |
| C1  | -2989  |        |        |        |
| C2  | 41.62  | -25459 |        |        |
| C3  | 1.46   | 69.66  | -21592 |        |
| C4  | 7.02   | 1.18   | 72.16  | -29342 |
| T1  | 1.02   | 0.92   | 0.87   | 0.94   |
| T2  | 5.7    | 5.3    | 5.6    | 10.2   |

**Crotonic Acid**



Figure 3.3: $^{13}$C-labeled trans-crotonic acid. The table shows the resonance frequencies (diagonal elements, in hertz), the J-coupling constants (off-diagonal elements, in hertz), and the relaxation times $T_1$ and $T_2$ (in seconds). $C_2$ and $C_3$ are used to simulate the dynamics of the spin-1 system, and $C_4$ is used as the ancilla that records the INRMs.

where $\mathbb{I}$ is identity and $\epsilon \approx 10^{-5}$ is the polarization. The NMR circuit of the PPS preparation is shown in Fig. 3.4. Note that the PPS in TS basis is same as in computational basis.

The Hamiltonian of the spin-1 system during the free evolutions in Fig. 3.2 is chosen as $\mathcal{H}_{sys} = -\Omega\sigma_x^{s_1}/2$, where $\Omega$ is set as 1 kHz and $\sigma_x^{s_1}$ is the Pauli operator in the spin-1 representation. The propagator at time $t_i$ is thus

$$U(t_i) = e^{-i2\pi\mathcal{H}_{sys}t_i}. \tag{3.7}$$

We prove the equivalence of the two basis:

The Clebsch-Gordan coefficient matrix is,

$$U_B = \begin{bmatrix} 1 & 0 & 0 & 0 \\ 0 & 1/\sqrt{2} & 1/\sqrt{2} & 0 \\ 0 & 0 & 0 & 1 \\ 1 & 1/\sqrt{2} & -1/\sqrt{2} & 0 \end{bmatrix}. \tag{3.8}$$
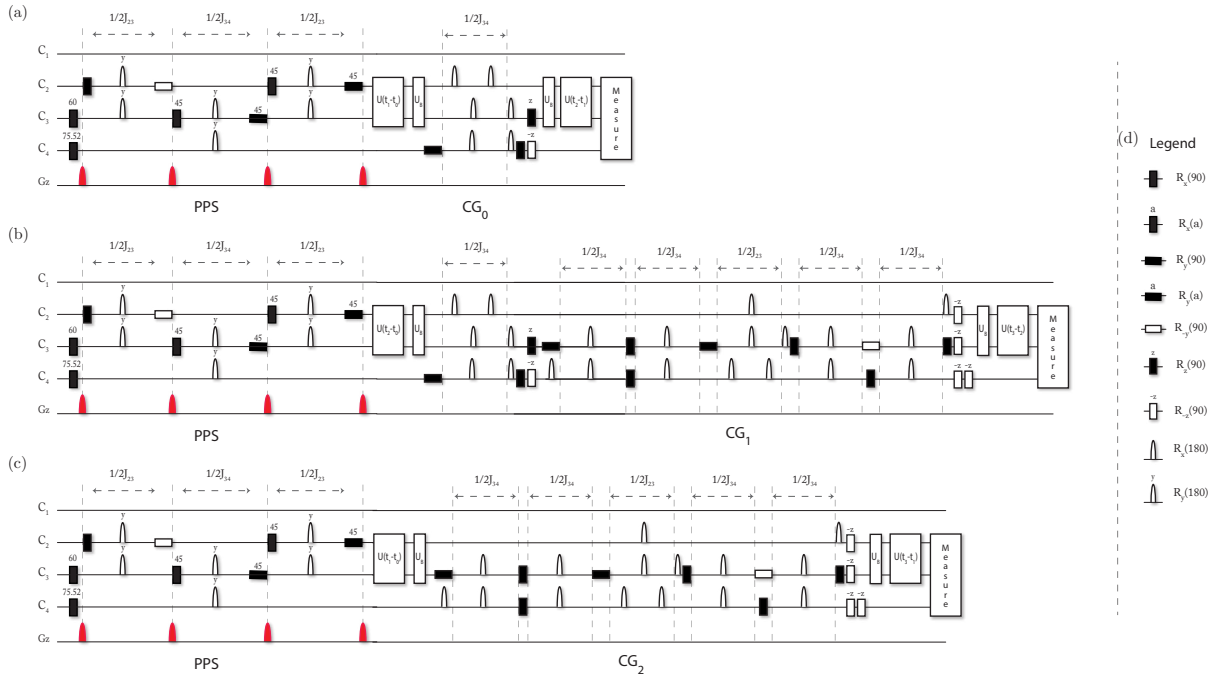
Figure 3.4: Pulse sequence for the measurement of $P(q_1, q_2)$, the different sequences corresponds to when the control gate used is (a) $CG_0$,(b) $CG_1$, and (c) $CG_2$. These gates are defined in eqns (3.3), (3.4), and (3.3) respectively. The gate $U_B$ is the Clebsch-Gordan matrix. The first four rows correspond to the pulses acting on different nuclei, and the last row represents the $z$-gradient field.

19

$U_B$ transforms computational basis to TS basis:

$$\begin{aligned}
U_B|00\rangle &= |00\rangle \equiv |0\rangle_s \\
U_B|01\rangle &= \frac{1}{\sqrt{2}}(|01\rangle + |10\rangle) \equiv |1\rangle_s \\
U_B|11\rangle &= |11\rangle \equiv |2\rangle_s \\
U_B|10\rangle &= \frac{1}{\sqrt{2}}(|01\rangle - |10\rangle) \equiv |s\rangle
\end{aligned} \tag{3.9}$$

We want the evolution under the spin-1 Pauli operator

$$\sigma_x^{s_1} = \frac{1}{\sqrt{2}} \begin{bmatrix} 0 & 1 & 0 \\ 1 & 0 & 1 \\ 0 & 1 & 0 \end{bmatrix}. \tag{3.10}$$

This can be achieved by evolution under $I_x^{12} = (\sigma_x \otimes \mathbb{I} + \mathbb{I} \otimes \sigma_x)/2$ in the computational basis. The matrix form of $I_x^{12}$ in computational basis is,

$$I_x^{12} = \frac{1}{2} \begin{bmatrix} 0 & 1 & 1 & 0 \\ 1 & 0 & 0 & 1 \\ 1 & 0 & 0 & 1 \\ 0 & 1 & 1 & 0 \end{bmatrix}, \tag{3.11}$$

And when one changes the basis to TS,

$$I_{x-TS}^{12} = U_B I_x^{12} U_B^\dagger = \frac{1}{\sqrt{2}} \begin{bmatrix} 0 & 1 & 0 & 0 \\ 1 & 0 & 1 & 0 \\ 0 & 1 & 0 & 0 \\ 0 & 0 & 0 & 0 \end{bmatrix}. = \begin{bmatrix} \sigma_x^{s_1} & \begin{matrix} 0 \\ 0 \\ 0 \end{matrix} \\ 0 \ 0 \ 0 & 0 \end{bmatrix} \tag{3.12}$$

Which, in the triplets acts equivalently to the desired evolution.

In the experiment, the three different times are chosen as $t_1 = 0.5$ ms, $t_2 = \tau + t_1$, and $t_3 = \tau + t_2$ respectively, and the experiments are conducted for a few values of $\tau$ as shown in Fig. 3.5. The observable to be measured is chosen as $Q = -|0\rangle\langle 0|_s + |1\rangle\langle 1|_s + |2\rangle\langle 2|_s$, which is equivalent to measuring the diagonal elements of the density matrix. Ideally, the maximal value of $K_3$ should be obtained at $\tau = 0.208$ ms, and the following tests of non-invasiveness are performed at this optimal point.

The controlled gates in Fig. 3.2 are decomposed into single-qubit rotations and delays,

and the pulse sequence of the entire experiment is illustrated in Fig. 3.4. All pulses are realized by the gradient ascent pulse engineering (GRAPE) technique [39, 40, 4], and are robust against the $B_1$ inhomogeneity with the fidelity over 0.997. The $\pi/2$ and $\pi$ pulses are of length 1 ms. The observable $Q$ is measured by performing diagonal tomography in the spin-1 subspace without considering the spin-0 component [41].

The values of $K_3$ for different $\tau$ are shown in Fig. 3.5, where the blue curve is the theoretical prediction, green circles are the simulated results with the $T_1$, $T_2$ and pulse imperfections incorporated, and red crosses are the experimental results. At the point of the maximum violation, $\tau = 0.208$ ms, the experimental values of correlations are $C_{12} = 0.542 \pm 0.021$, $C_{23} = 0.294 \pm 0.016$, and $C_{13} = -0.676 \pm 0.003$, respectively. It leads to the experimental value of $K_3 = 1.511 \pm 0.027$, consistence with the simulated result 1.495. In contrast, the ideal value of the maximum violation is 1.757, and the discrepancy ($\approx 0.246$) between the experimental and ideal value is dominated by the $T_1$, $T_2$ relaxation, as the pulse imperfections merely contribute around 0.01 loss of the ideal value. $T_1$, $T_2$ relaxation simulation were performed by solving the Lindblad equation for a general noise, the explicit calculations are shown in Appendix B of [42]. Full experimental data is shown in Table 3.1
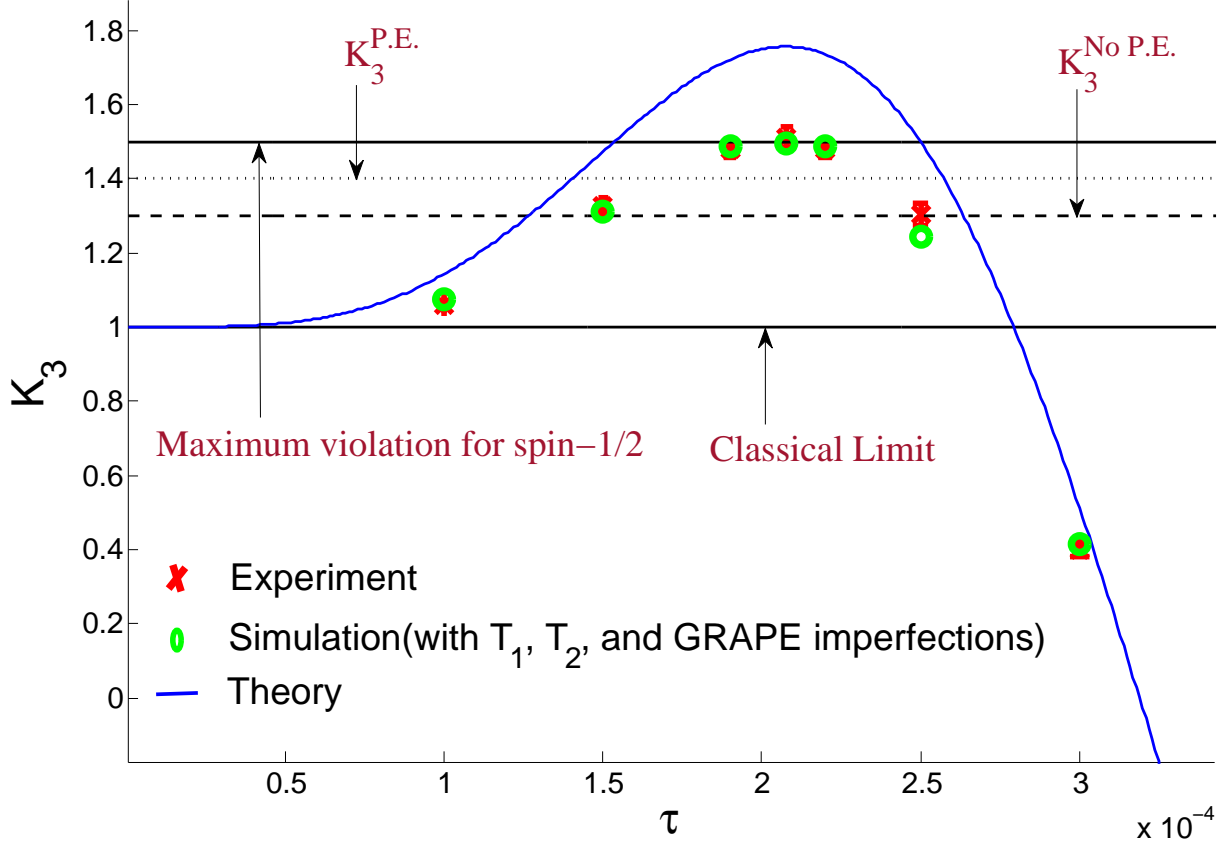
Figure 3.5: Experimental values of $K_3$ (red crosses) along with the ideal quantum prediction (blue curve) and simulated results (green circles). $\tau$ is the tunable time between measurements, i.e. $\tau = t_2 - t_1 = t_3 - t_2$. A violation of the LGI means the value of $K_3$ goes beyond 1 which is the classical limit. The maximum violation in a 3-level system is $K_3 \approx 1.757$ when choosing $\tau = 0.208$ ms. In experiment, decoherence limits our maximum violation around $K_3 = 1.511 \pm 0.027$. $K_3^{P.E.}$ and $K_3^{NoP.E.}$ corresponds to modification on inequality when including preparation error and not including them. These values are defined in more detail in the text.

| | Measure at time, $t_1$ and $t_2$ | | | Measure at time, $t_2$ and $t_3$ | | | Measure at time, $t_1$ and $t_3$ | | |
|---|---|---|---|---|---|---|---|---|---|
| | Theory | Sim | Exp | Theory | Sim | Exp | Theory | Sim | Exp |
| 00 | 0.0000 | 0.0003 | $0.0317 \pm 0.0134$ | 0.0778 | 0.0765 | $0.0949 \pm 0.0025$ | 0.0000 | 0.0306 | $0.0289 \pm 0.0033$ |
| 01 | 0.0000 | 0.0333 | $0.0703 \pm 0.0054$ | 0.0636 | 0.0758 | $0.0497 \pm 0.0028$ | 0.0000 | 0.0007 | $0.0486 \pm 0.0018$ |
| 02 | 0.0000 | 0.0131 | $0.0020 \pm 0.0029$ | 0.0186 | 0.0021 | $0.0090 \pm 0.0001$ | 0.0000 | 0.0001 | $0.0033 \pm 0.0020$ |
| 10 | 0.0000 | 0.0174 | $0.0142 \pm 0.0027$ | 0.2170 | 0.2036 | $0.1876 \pm 0.0047$ | 0.0000 | 0.0467 | $0.0090 \pm 0.0041$ |
| 11 | 0.0000 | 0.0253 | $0.0755 \pm 0.0038$ | 0.0318 | 0.0183 | $0.0325 \pm 0.0079$ | 0.0000 | 0.0030 | $0.0410 \pm 0.0022$ |
| 12 | 0.0000 | 0.0195 | $0.0027 \pm 0.0010$ | 0.2170 | 0.2294 | $0.2331 \pm 0.0043$ | 0.0000 | 0.0048 | $0.0009 \pm 0.0006$ |
| 20 | 0.1364 | 0.1487 | $0.1680 \pm 0.0005$ | 0.0542 | 0.0781 | $0.1175 \pm 0.0112$ | 0.8682 | 0.7771 | $0.7925 \pm 0.0054$ |
| 21 | 0.4659 | 0.4061 | $0.3616 \pm 0.0026$ | 0.1853 | 0.1681 | $0.1713 \pm 0.0024$ | 0.1272 | 0.1372 | $0.1064 \pm 0.0013$ |
| 22 | 0.3977 | 0.3378 | $0.3245 \pm 0.0010$ | 0.1582 | 0.1497 | $0.1261 \pm 0.0038$ | 0.0046 | 0.0144 | $0.0004 \pm 0.0002$ |
| sum | 1 | 1.0015 | 1.0504 | 1 | 1.0029 | 1.0217 | 1 | 1.0146 | 1.0309 |

Table 3.1: **Experimental results for the setting that leads to a maximal LG violation.** Each table shows the result for a single setting (see Fig. 3.1). The row index denotes the two measurement outcomes and the three values (Theory, Sim, Exp) correspond to the probabilities for these outcomes in theory, simulation and experiment respectively. (For example the row 01 represents the probability that the result was 0 in the first measurement and 1 in the second *i.e.* $P(0, 1)$). We then use these probabilities to calculate correlation as defined in eq. (3.1), which finally is used to get the value of $K_3$ using eq. (3.2). The decoherence during the experiment and simulations boosts some values and diminishes some. Since the results are post-selected, the probabilities in the simulation and experiment do not add up to 1.

## 3.5 Experimental test of assumptions.

In getting the theoretical bound of $K_3$ we have made a number of implicit assumptions about our experimental system, in which the most notable assumption is INRMs. Since it is possible to modify the LGI by taking into account any deviations from these assumptions, our experiment is supplemented by another set of experiments to test (i) the invasiveness of the intermediate measurements and loss, (ii) preparation errors, and (iii) malicious losses. We also discuss the possibility of dark counts. An additional assumption about the pseudo-pure state is discussed in section 3.6.

First we quantify how much the system is disturbed due to the imperfect controlled gates. Ideally these controlled gates should not disturb the system when it is in a fixed state $|0\rangle_s, |1\rangle_s, |2\rangle_s$ or $|s\rangle$, but in practice they do disturb the system due to the long application time and pulse imperfections. Moreover, the three controlled gates are distinct and are expected to have different back actions on the system even after the negative results are post-selected in the INRMs. Explicitly, $CG_0$ is a direct J-coupling gate, $CG_2$ involves two SWAP gates and $CG_1$ is a combination of the two. The experimental lengths

of $CG_0$, $CG_1$ and $CG_2$ are about 40 ms, 116 ms and 76 ms, respectively. In attempt to quantify how much the system is disturbed by INRMs, we perform the following two types of experiments: (a) start with either $|0\rangle_s$, $|1\rangle_s$, or $|2\rangle_s$, evolve the system for a fixed time and measure the probabilities; (b) start with either $|0\rangle_s$, $|1\rangle_s$, or $|2\rangle_s$, apply the controlled gate,evolve the system for the same amount of fixed time and measure the probabilities. Ideally, the results from the two experiments should match perfectly, but they indeed have variations in the presence of errors. Table 3.2 shows the experimental results and their contribution to the inequality is discussed in next section.

In testing non-invasiveness we can calculate the correlation, $C$, value when the starting state is $|p\rangle_s (p = 0, 1, 2)$ using eq. (3.1))

$$C_{|p=0\rangle} = P(0,0) - P(0,1) - P(0,2)$$
$$C_{|p=1,2\rangle} = -P(p,0) + P(p,1) + P(p,2) \tag{3.13}$$

Now the difference between the $C$ value when we apply the gate vs no gate is the disturbance induced by our measurements. This $\Delta C$ values contribute thrice in calculation of LGI (eq.3.2). Since it contributes 2 times positively and one time negatively, we define the following modification over the original inequality

$$KM1 = -\min(\Delta C \pm P.E., 0) + 2\max(\Delta C \pm P.E., 0) \tag{3.14}$$

where $P.E.$ is the preparation error, i.e. contribution to correlation due initial state deviating from the expected.

The values of probabilities which were not used in eq.(3.13) are the probabilities corresponding to the red color rows of Table 3.2 and thus are considered as loses. The lowest value when we apply no gate is considered non malicious since it is independent of the gate and/or initial state. The difference between the highest and lowest give the range for the possible malicious errors. Now this is the value for one evolution, in the LG experiment there are 5 such evolutions (two for each of the experiments giving $C_{13}$ and $C_{23}$ and one for the experiment giving $C_{12}$), hence the total malicious loss($Mal$) if 5 times the difference (see Table. 3.2).

With these modifications, we modify the original inequality on $K_3$ to

$$K_3^{P.E.} \leq 1 + KM1 + Mal = 1 + 0.1936 + 0.2095 = 1.4031 \tag{3.15}$$

We note that while this value takes the imperfections in preparation into account in the worst possible way, it is extremely unlikely that these preparation errors decrease the

| | Starting state = $|0\rangle\langle0|$ | | Starting state = $|1\rangle\langle1|$ | | Starting state = $|2\rangle\langle2|$ | |
|---|---|---|---|---|---|---|
| | $NG$ | CG$_0$ | $NG$ | CG$_1$ | $NG$ | CG$_2$ |
| 00 | 0.3885±0.0022 | 0.3582±0.0021 | 0.4297±0.0017 | 0.4133±0.0034 | 0.1343±0.0012 | 0.1570±0.0015 |
| 01 | 0.0001±0.0002 | 0.0323±0.0040 | 0.0071±0.0012 | 0.0273±0.0016 | 0.0001±0.0003 | 0.0164±0.0023 |
| 10 | 0.4143±0.0055 | 0.3974±0.0023 | 0.0521±0.0023 | 0.0570±0.0013 | 0.4023±0.0028 | 0.3637±0.0026 |
| 11 | 0.0006±0.0007 | 0.0147±0.0012 | 0.0091±0.0032 | 0.0293±0.0019 | 0.0290±0.0022 | 0.0472±0.0018 |
| S0 | 0.0525±0.0026 | 0.0370±0.0067 | 0.0745±0.0022 | 0.0672±0.0028 | 0.0656±0.0026 | 0.0721±0.0014 |
| S1 | 0.0003±0.0002 | 0.0011±0.0018 | 0.0040±0.0002 | 0.0021±0.0001 | 0.0004±0.0002 | 0.0002±0.0002 |
| 20 | 0.1428±0.0025 | 0.1351±0.0029 | 0.4219±0.0019 | 0.4031±0.0031 | 0.3680±0.0017 | 0.3431±0.0012 |
| 21 | 0.0009±0.0003 | 0.0242±0.0021 | 0.0016±0.0002 | 0.0007±0.0003 | 0.0003±0.0006 | 0.0002±0.0001 |

Table 3.2: **Experimental results for the test on non-invasiveness.** Each of the three tables shows the result of the experiments in which we either don't apply the gate or apply the gate before evolution, when starting with the state mentioned on the top. The rows corresponds to the probabilities of the state denoted in first column. The first and second index in first column corresponds to the state of system and ancilla respectively. CG$_i$ stands for the gate applied and $NG$, when no gate is applied. Ideally the column $NG$ should contain positive values only for the states $|00\rangle, |10\rangle$ and $|20\rangle$ (in blue), all other values are treated as losses since they are lost in post-selection. Moreover, for an INRM the columns NG and $CG_i$ should match, the discrepancies between these columns at the post selected values (blue) are used to give an upper bound on the possible deviation from $K_3$ due to the measurement procedure.

discrepancy between the ideal measurements and the actual measurements. A slightly more liberal version of the inequality would read

$$
\begin{aligned}
KM1 = & -\min(\Delta C, 0) + 2\max(\Delta C, 0) \qquad (3.16) \\
K_3^{NoP.E.} \leq & \quad 1 + KM1 + Mal \\
= & \quad 1 + 0.0912 + 0.2095 = 1.3007
\end{aligned}
$$

Finally, we must account for the sources of errors that lead to *dark counts*, i.e an artificial increase in the probabilities that are post selected. There are two possible sources for this kind of error. First the measurements are not perfect and there are situations where the ancilla does not rotate to $|1\rangle$ when it should, leading to a false reading of $|0\rangle$. Second, there are situations where a system in the singlet state goes back into one of the triplet states. The margin for the violation leaves us with an upper bound on the tolerance of the violation for possible dark counts, assuming these behave in the most malicious way

| | Starting state $= |0\rangle\langle 0|$ | | Starting state $= |1\rangle\langle 1|$ | | Starting state $= |2\rangle\langle 2|$ | |
|---|---|---|---|---|---|---|
| | $NG$ | $CG_0$ | $NG$ | $CG_1$ | $NG$ | $CG_2$ |
| $Q$ | -0.1686 | -0.1743 | 0.0443 | 0.0468 | 0.6360 | 0.5498 |
| $\Delta Q = Q_G - Q_{NG}$ | $-0.0057$ | | 0.0025 | | $-0.0862$ | |
| P.E. | 0.0187 | | 0.0436 | | 0.0152 | |
| $\Delta Q -$P.E. | $-0.0244$ | | $-0.0411$ | | $-0.1014$ | |
| $\Delta Q +$P.E. | 0.0130 | | 0.0461 | | $-0.0710$ | |
| $KM1$ | 0.1936 | | | | | |
| $Non.Mal$ | 0.0544 | | | | | |
| $Mal$ | $0.0419 * 5 = 0.2095$ | | | | | |

Table 3.3: **Summary of imperfections calculated in the test of non-invasiveness.** The table list various modification made to the original LG as explained in text. Loss is calculated using the discarded values in an experiment where we don't expect to discard any values in post-selection (the red columns in table 3.2 are discarded in post selection, and the loss is the sum of these values). $Q$ is calculated using equation-(3.13), $\Delta Q$ is the difference of $Q$ values when the gate is applied and when it is not. For an INRM and the setup used $\Delta Q = 0$ and any deviation from 0 could theoretically boost $K_3$ even in a MR system. P.E. stands for preparation error, i.e the probability that the prepared starting state is not the desired starting state. KM1 is the maximal boost to $K_3$ due to measurement error, as defined in equation-(3.14). The losses are broken into two types. Non-Malicious (Non. Mal.) are the losses that appear irrespective of the specific experiment. Malicious ( Mal) are the losses that may depend on the choice of experiment. We assume the malicious losses are chosen in such a way that they boost the calculated value $K_3$ by as much as possible.

possible. Based on eq. (3.16, 3.15) the experiment can tolerate malicious errors in dark counts that will produce an artificial increase of the calculated value up 0.2 depending on how we account for preparation errors in the test of non-invasiveness.

## 3.6 The pseudo pure state dynamics.

In an NMR experiment we have access to pseudo-pure states, to verify that this does not effect the credibility of the result, we perform the Leggett-Garg experiment starting from an identity state instead of $|0\rangle$ for the system. If starting from an identity state the end state remains identity it has no contribution in the Leggett-Garg inequality. The spectra

for the Leggett Garg test on the identity was compared with a reference spectra of an initial thermal state (see fig. 3.6) to ensure that the contribution of the signal is below the level of precision used in the experiment. This approach to handling the PPS state is very different from the *venality* approach introduced in [33]. Venality, is the fraction of ancilla that was incorrectly prepared thus resulting in the false reading. Venality is only suitable for systems where the polarization is high enough to handle adversarial noise.
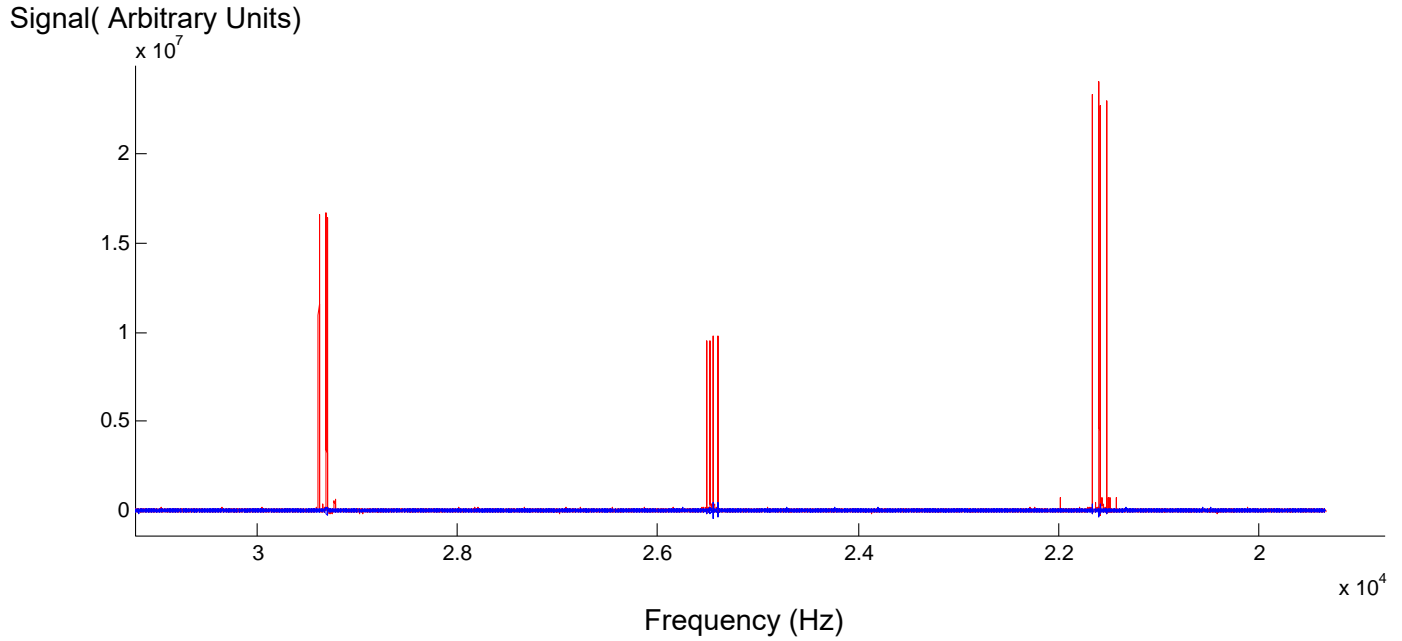


Figure 3.6: **The spectra for the LG experiment with the identity as the initial state**. The blue spectra is the signal for a run of the Leggett-Garg experiment with the identity as the initial state. The red spectra is the initial thermal state which is given as a reference. Note that while an identity will give a flat spectrum at 0, the flat spectrum does not guarantee that the state is the identity. To verify that this is the identity we rotated the state before the final measurement and produced the same flat spectrum for different observables.

27

## 3.7   Discussion.

The motivation behind a LG experiment is to test macroscopic realism, i.e try to refute MR for a *macroscopic* system or at least convince a skeptic that MR assumption is implausible. While the NMR sample that we use can be considered macroscopic, the individual molecules are still in the microscopic domain, moreover there is little doubt that the individual nuclear spins can be in a superposition state. In that respect it is not too surprising that the LGI is violated, and indeed its violation tells us nothing new about macroscopic realism. We do, however, learn that we can control the systems well enough to violate the inequality and that the qutrit used can pass some quantum tests under reasonable assumptions. The violation of a LGI does not rule out the existence of a hidden variable model and indeed a skeptic could simply argue that our system behaves strangely due to the existence of hidden variables that are influenced by our choice of measurements. For liquid state NMR we already know that such a model exists [43]. Moreover we purposely discarded some of the experimental data as part of the experiment, i.e the spectrum generated at the end of each experiment could be used to generate more than the six probabilities we discussed (the off diagonal elements in the density matrix).

Since we are not, strictly speaking, testing MR, our main result is not the violation per-se but rather the methods used to achieve the violation, the discussion of possible errors in the experiment and the demonstration of their experimental relevance. Such a discussion has been missing from much of the experimental literature to date (see [18, 33, 36] for exceptions). The LG test cannot be performed without some assumptions about the physical systems involved and, in particular, the inner workings of the measurements that we assume are non invasive. These assumptions must be tested, as they can lead to artificial violations of the inequality. In our experiment we tested particular malicious scenarios that, although unlikely, must be taken into account and discussed before they are rejected (experimentally or theoretically). We note that both our simulated predictions and experimental results (see Fig. 3.5) show that such artificial violations are unlikely in our system, consequently we believe that although many previous experiments did not include a careful analyses of possible errors, the violations of LGI in those experiments would probably hold even if imperfections were taken into account.

We have made a fair sampling approximation, since we can only measure the part of the system i.e. big part of our system is in identity state, we assume that the measurable part represent the rest. Without the approximation we cannot violate LGI at typical room temperature NMR.

*Conclusion.* We demonstrated a violation of 3-level LGI. Non-invasive measurements, an essential requirement when performing a LG test were carried out using negative result

measurements. We quantified the deviation from the assumption that the measurements are non-disturbing and modified the LGI accordingly. We also took in account other errors that can occur in the experiment and used them to modify the original inequality. These modifications resulted in increasing the classical bound and making our violation significantly smaller (but still beyond the error margins). We emphasize that the margin of violation between quantum and classical upper bound is greater when a 3-level system is tested (compared to a 2-level system). In practice the actual margin is quite low when various errors are taken in account and the use of the modified (non Lüders) measurement scheme allowed us to observe the violation despite many imperfections. The difference in experimental value from theoretical is due to the T1 and T2 decay, these errors can be avoided in different systems, for example if the couplings are strong, the gate lengths will be short. It would be a challenge to the quantum control community to observe a violation larger than 0.5 above the classical bound (modified for imperfections), however the real challenge remains to demonstrate such violations in macroscopic systems.

# Chapter 4

# Enhancing quantum control by bootstrapping a quantum processor of 12 qubits

## 4.1 Introduction

A quantum gate is implemented on a quantum processor by controlling some experimental parameters, these parameters depends on the type of quantum processor. In a Nuclear Magnetic Resonance (NMR) quantum processor the gates are implemented by Radio Frequency(RF) pulses, and the variable controlling these composite RF pulses are the phases,frequency and amplitudes of the individual pulses. There exists many ways to optimize for these variables, but most powerful and used method is gradient ascent pulse engineering (GRAPE), which as the name suggest calculate gradient of the optimization function to iteratively update the control parameters [44]. GRAPE is used in wide variety of quantum computing implementations including NMR [45], electron spin resonance(ESR) [46], nitrogen-vacancy(NV) centers in diamond [47, 48], superconducting circuits [49, 50], and ion traps [51, 52].

The difficulty of using these methods for optimizing quantum gates is that they require full system simulation of the quantum system, which becomes an exponentially harder task as the size of the system grows. Other than that, the fidelity of implementation depends on the knowledge of Hamiltonian and inhomogeneities of the implementation apparatus. Here we consider the task of optimizing a control field that will drive the quantum system from a fixed input state $\rho_i$ to a desired target state $\rho_f$. At each iteration $k$ of the GRAPE, the

algorithm computes the evolution of the initial state of the system under a RF pulse, which results in a final state $\tilde{\rho}$ and then the value of fitness function $f = tr(\tilde{\rho}\rho_f)$ is calculated. Where $\rho_f$ is the desired state. If the fitness function is not of desired value, it then computes the gradient $g$, to be use in updating the pulse control parameters. In every iteration of the algorithm a quantum evolution has to be simulated which requires exponentiating and multiplying $2^n \times 2^n$ matrices, which becomes harder and harder as $n$ increases.

Recently, Li et al. [5] and later Rebentrost et al. [53] showed that a quantum processor can be used to calculate $f$ and $g$ efficiently. A technique called measurement-based quantum feedback control (MQFC) enables direct measurement of $f$ and $g$ (see Fig. 4.1), allowing the quantum processor to optimize its own pulses. MQFC addresses both the issues of scalability and control inaccuracies due to imperfect system characterization [54, 55]. Moreover, this technique is transferable to any implementation in which control fields steer the system evolution and measurement in a standard basis is possible. In this work, we implement MQFC on a 12-qubit NMR quantum processor, and in particular demonstrate for the first time that MQFC enhances the control precision by about 10% due to its self-feedback property. Furthermore, by creating the 12-coherent state we demonstrate the capability of our quantum processor to function as a universal 12-qubit quantum processor with high-fidelity individual controls.

## 4.2 Theory

In NMR as shown in eq. (2.13) the unnormalized deviation density matrices are refereed as 'states'. To distinguish them from the Hamiltonian, we use capital X, Y, and Z to denote states and $\sigma_x$, $\sigma_y$ and $\sigma_z$ to denote Hamiltonians, while they both refer to the same set of Pauli matrices.

### 4.2.1 Quantum processor.

In our NMR quantum processor, the liquid-state sample is per-$^{13}$C labeled (1S,4S,5S)-7,7-dichloro-6-oxo-2-thiabicyclo[3.2.0]heptane-4-carboxylic acid dissolved in d6-acetone, which forms a 12-qubit register. The 12 qubits are denoted by nuclear spins $C_1$ to $C_7$ ($^{13}$C-labeled) as qubits 1 to 7, and $H_1$ to $H_5$ as qubits 8 to 12 in the molecule shown by Fig. 4.5a. When placed in a static $z$-magnetic field, the values of Hamiltonian parameters can be found in Fig. 4.2.
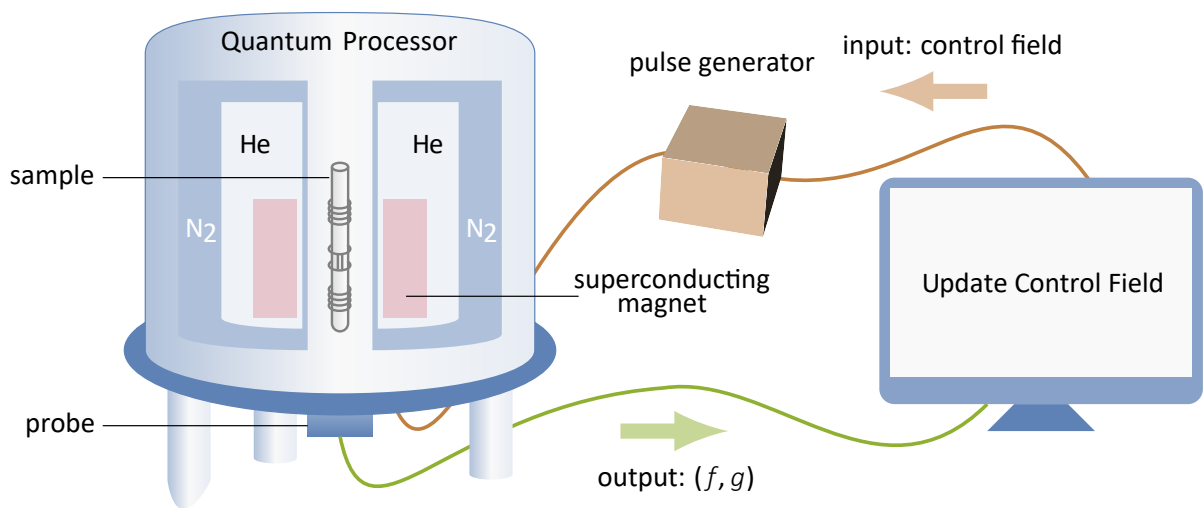
Figure 4.1: MQFC process for optimizing a control field. Starting from an initial guess, a shaped pulse is created from the pulse generator and then applied to the sample. The fidelity function $f$ of the control pulse and its gradient $g$ are directly measured on the quantum processor, where $g$ is used for updating the control field till that sufficiently high fidelity $f$ has been achieved.

| | C1 | C2 | C3 | C4 | C5 | C6 | C7 | H1 | H2 | H3 | H4 | H5 |
|---|---|---|---|---|---|---|---|---|---|---|---|---|
| **C1** | 30020 | | | | | | | | | | | |
| **C2** | 57.58 | 8779 | | | | | | | | | | |
| **C3** | -2.00 | 32.70 | 6245 | | | | | | | | | |
| **C4** | 0 | 0.30 | 0 | 10333 | | | | | | | | |
| **C5** | -1.25 | 2.62 | 1.11 | 33.16 | 15745 | | | | | | | |
| **C6** | 5.54 | -1.66 | 0 | -3.53 | 33.16 | 34381 | | | | | | |
| **C7** | 1.25 | 37.48 | 0.94 | 29.02 | 21.75 | 34.57 | 11928 | | | | | |
| **H1** | 0 | 0 | 2.36 | 166.6 | 4.06 | 5.39 | 8.61 | 3310 | | | | |
| **H2** | 4.41 | 1.86 | 146.6 | 2.37 | 0 | 0 | 0 | 0 | 2468 | | | |
| **H3** | 1.81 | 3.71 | 146.6 | 2.37 | 0 | 0 | 0 | 0.18 | -12.41 | 2158 | | |
| **H4** | -13.19 | 133.6 | -6.97 | 6.23 | 0 | 5.39 | 3.78 | -0.68 | 1.28 | 6.00 | 2692 | |
| **H5** | 7.87 | -8.35 | 3.35 | 8.13 | 2.36 | 8.52 | 148.5 | 8.46 | -1.06 | -0.36 | 1.30 | 3649 |
| $T_1$ | 7.99 | 3.61 | 1.83 | 3.72 | 9.89 | 7.80 | 3.64 | 3.83 | 2.13 | 2.28 | 2.65 | 3.47 |
| $T_2^*$ | 0.40 | 0.31 | 0.44 | 0.25 | 0.25 | 0.40 | 0.38 | 0.29 | 0.39 | 0.34 | 0.15 | 0.30 |

C-13 labeled 12-qubit system

Dichloro–cyclobutanone
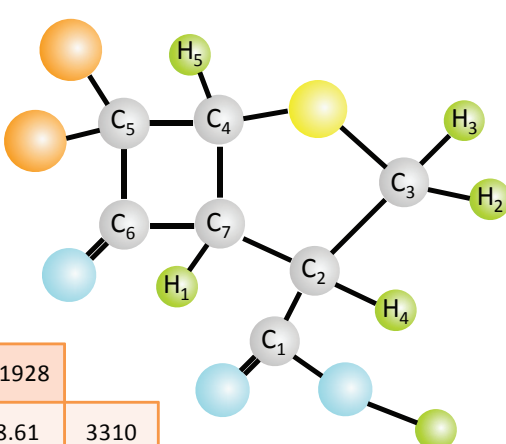


Figure 4.2: . Molecular structure and Hamiltonian parameters of per- [13]C labeled (1S,4S,5S)-7,7-dichloro-6-oxo-2-thiabicyclo[3.2.0]heptane-4-carboxylic acid. $C_1$ to $C_7$, and $H_1$ to $H_5$ denote the 12 qubits from qubit 1 to qubit 12, respectively. The diagonal elements are the chemical shifts (in Hz), and the off-diagonal elements are the J-couplings between two spins (in Hz). The relaxation times T1 and T2 (in seconds) are also listed at bottom.

The control Hamiltonian is due to the transverse control field applied in the $x$-$y$ plane, which is often digitized into $M$ slices with slice length $\Delta t$. In each slice, there are four constant control parameters, leading to a control Hamiltonian in the form of

$$\mathcal{H}_c[m] = \mathrm{B}_x^{\mathrm{C}}[m] \sum_{i=1}^{7} \sigma_x^i + \mathrm{B}_y^{\mathrm{C}}[m] \sum_{i=1}^{7} \sigma_y^i \tag{4.1}$$
$$+\mathrm{B}_x^{\mathrm{H}}[m] \sum_{j=8}^{12} \sigma_x^j + \mathrm{B}_y^{\mathrm{H}}[m] \sum_{j=8}^{12} \sigma_y^j,$$

where, for example, $\mathrm{B}_x^{\mathrm{C}}[m]$ means the $x$-component of the $m$th slice of control field in the $^{13}$C channel. The superscript H stands for $^1H$ channel.

The dynamics of the NMR system is governed by internal ($\mathcal{H}_s$) and control ($\mathcal{H}_c$) Hamiltonian simultaneously, which implies the propagator is

$$U_1^M = U_M U_{M-1} \cdots U_1, \tag{4.2}$$

where

$$U_m = e^{-i(\mathcal{H}_s + \mathcal{H}_c[m])\Delta t}. \tag{4.3}$$

and the shorthand,

$$U_m^M = U_M U_{M-1} \cdots U_m. \tag{4.4}$$

The essence of NMR quantum information processing is to optimize a control field, i.e. find a sequence of $\mathrm{B}_{x,y}[m]$, such that one can precisely realize a quantum gate or drive the system to a target state according to Eq. (4.2).

## 4.2.2 Fundamentals of the GRAPE algorithm.

To implement a particular target gate or state we need to find an optimal $\mathrm{B}_{x,y}[m]$. One of the most prominent optimization algorithms to date is the GRAPE algorithm [44] which was developed for the design of optimal control pulses in NMR spectroscopy. Here, we explain the basic principle of GRAPE by considering the problem of state engineering in the absence of relaxation.

Suppose the initial state of the spin system is $\rho_i$, and the target output state is $\rho_f$. After applying a $M$-slice trial control pulse, the system will evolve to

$$\tilde{\rho} = U_1^M (\rho_i) = U_1^M \rho_i U_1^{M\dagger}. \tag{4.5}$$

The fitness function defined as $f = \text{tr}(\rho_f \tilde{\rho})$ serves as a metric for the control fidelity, with the form

$$f = \text{tr}(\rho_f \tilde{\rho}) = \text{tr}\left(U_1^M\left(\rho_i\right) \cdot \rho_f\right). \tag{4.6}$$

To find the optimum value of $f$ we calculate the gradient function to the first order

$$g_{x,y}[m] = \frac{\partial f}{\partial \text{B}_{x,y}[m]}$$

$$\approx \sum_{k=1}^{n} \text{tr}\left(-i\Delta t \cdot U_{m+1}^M\left[\sigma_{x,y}^k, U_1^m\left(\rho_i\right)\right] U_{m+1}^{M\dagger} \cdot \rho_f\right), \tag{4.7}$$

where, $k$ runs over different spins, $n$ is total number of spins, and $\left[\sigma_{x,y}^k, U_1^m\left(\rho_i\right)\right]$ is the commutator between $\sigma_{x,y}^k$ and $U_1^m\left(\rho_i\right)$. We may increase the fitness function $f$ by using the gradient iteration rule

$$\text{B}_{x,y}[m] \leftarrow \text{B}_{x,y}[m] + \epsilon \cdot g_{x,y}[m], \tag{4.8}$$

where $\epsilon$ is a suitably chosen step size.

The GRAPE algorithm proceeds as follows on a classical computer:

*1.* start from an initial guess control $\text{B}_{x,y}[m]$;

*2.* calculate $\tilde{\rho}$ according to Eq. (4.5);

*3.* evaluate fitness function $f = \text{tr}(\rho_f \tilde{\rho})$;

*4.* if $f$ does not reach our preset value, evaluate gradient function $g$ according to Eq. (4.7);

*5.* update control variables according to Eq. (4.8), then go to step *2.*

### 4.2.3 MQFC optimization.

The GRAPE algorithm requires the calculation of $U_1^M$, i.e., the dynamics of the system. This step is inefficient on a classical computer when the size of the system is large. In contrast, the scheme of MQFC optimization provides an alternative way which enables direct measurement of $f$ and $g$ in the experimental manner, or explicitly, via the quantum evolution and measurement of the quantum processor.

Without loss of generality, let us discuss the scenario of ensemble quantum computing. e.g., NMR quantum computing, where the state is usually written as a traceless deviation

density matrix and a single-shot measurement is sufficient to get the expected value of an observable. For other systems that use the computational basis or projective measurement, the following procedure needs to be slightly modified and more repetitions may be required to get the estimate of $f$ and $g$.

Measuring $f$ is straightforward. For an $n$-qubit system, the total number of elements in the Pauli basis is $4^n - 1$ (without the identity term). If the target state $\rho_f$ has some decomposition, say, $\rho_f = \sum_{\gamma=1}^{\mathcal{G}} x_\gamma P_\gamma$ with respect to the Pauli basis, then the fitness function is

$$f = \operatorname{tr}(\tilde{\rho}\rho_f) = \sum_{\gamma=1}^{\mathcal{G}} x_r \operatorname{tr}(\tilde{\rho} P_r). \tag{4.9}$$

Here, $1 \leq \mathcal{G} \leq 4^n$ denotes the number of nonzero components, $P_\gamma$ is the $\gamma$-th element of the Pauli basis, and $x_\gamma$ is its corresponding coefficient.

Therefore, $\mathcal{G}$ experiments are required to estimate $f$. In the $\gamma$-th experiment, we just need to apply the control field to the initial state $\rho_i$ and measure the expectation value $\langle P_\gamma \rangle$ of $\tilde{\rho}$. For a generic $\rho_f$ that contains all $\mathcal{G} = 4^n - 1$ Pauli terms, measuring $f$ in experiment is equivalent to carrying out full state tomography, and is thus inefficient. However, many tasks require the creation of a *simple* target state where $\mathcal{G}$ is quite small. For instance, if we aim to prepare the 12-coherent state $\rho_f = Z^{\otimes 12}$, one measurement is sufficient to obtain $f$.

Measuring $g$ requires us to realize the commutator $[\sigma_{x,y}^k, \cdot]$ inside Eq. (4.7). In fact [5],

$$\left[\sigma_{x,y}^k, \rho\right] = i\left(\mathcal{R}_{x,y}^k(\rho) - \overline{\mathcal{R}}_{x,y}^k(\rho)\right), \tag{4.10}$$

in which $\mathcal{R}_{x,y}^k(\rho)$ and $\overline{\mathcal{R}}_{x,y}^k(\rho)$ mean a selective $\pi/2$ rotation and $-\pi/2$ of the $k$-th qubit about $x$ or $y$ axis acting on state $\rho$, respectively. By substituting Eq. (4.10) into Eq. (4.7), we get

$$\begin{aligned} g_{x,y}[m] &= \Delta t \sum_{k=1}^{n} \operatorname{tr}\left\{\left(U_{m+1}^M \mathcal{R}_{x,y}^k U_1^m\right)(\rho_i) \cdot \rho_f\right\} \\ &- \Delta t \sum_{k=1}^{n} \operatorname{tr}\left\{\left(U_{m+1}^M \overline{\mathcal{R}}_{x,y}^k U_1^m\right)(\rho_i) \cdot \rho_f\right\}. \end{aligned} \tag{4.11}$$

The terms on the right-hand side are very similar to the measurement of $f$ in Eq. (4.6), and the only difference is the local $\pm\pi/2$ pulse inserted between slices $m$ and $m+1$. Explicitly, the $m$-th component of $g_{x,y}$ is a weighted sum of $4n\mathcal{G}$ measurement quantities, where 4 comes from the $\pm\pi/2$ pulses about the $x$ and $y$ axes, $n$ from the sum over all the qubits,

36
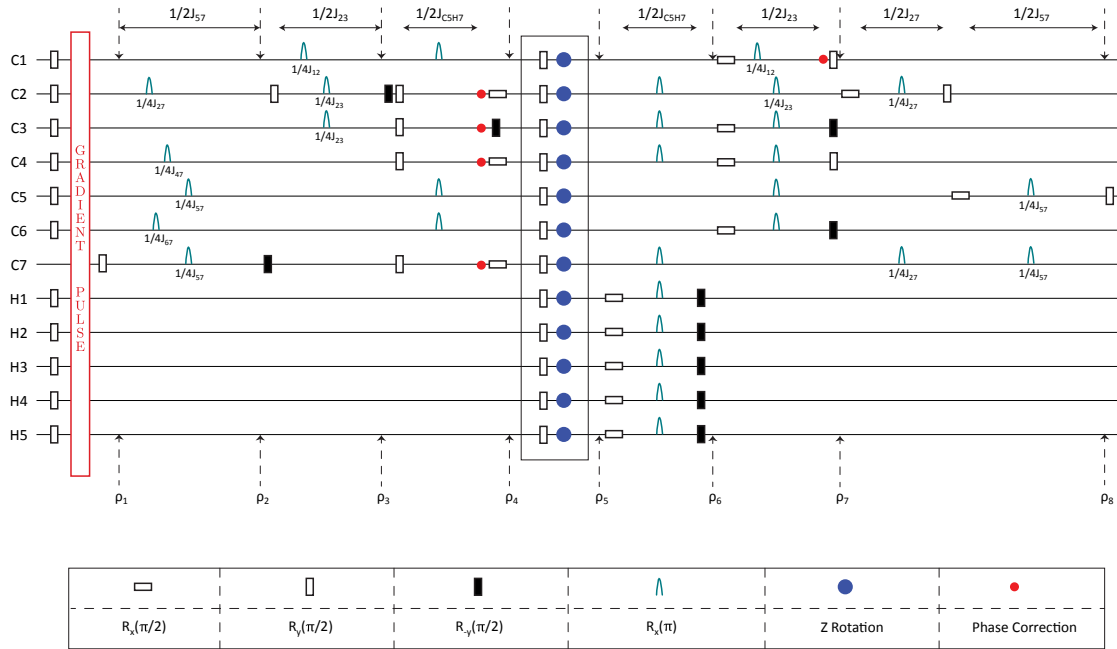
Figure 4.3: Quantum circuit to create a pseudo-pure state.

and $\mathcal{G}$ from the measurement of $f$. In each experiment, compared to the way of measuring $f$, we just need to insert a local $\pi/2$ pulse after the $m$-th slice evolution. Provided that all the qubits are well individually addressed, high fidelities are attainable in implementing these local $\pi/2$ rotations.

In summary, we need $4n\mathcal{G}M$ experiments in total to perform the gradient measurement, which is linear in the number of qubits for our case of target state being 12-coherence state.

## 4.3 Experiment

### 4.3.1 Experimental MQFC optimization.

The circuit to prepare the pseudo pure state on 12-qubits is shown in Fig. 4.3. It was designed by making an approximation that the big couplings of all the $^1H$ with the corresponding $^{13}C$ were assumed to be equal to 148 Hz. The reason for assumption is that the $^1H$ chemical shifts are too close thus their individual control is very hard to achieve, also it simplified and shortened the circuit. This obviously had a trade-off in the fidelity even before the non-ideal pulses and experimental imperfections. The result of this approximation on fidelities at different point in the circuit is shown in Fig. 4.4.

Now we turn to the experiment where the MQFC optimization is used to create the 12-coherent state in the 12-qubit quantum processor. The 12-coherent state is the state

$$I^{\pm} = I_x \pm iI_y$$

$$A_1 = \cos[2\pi(\omega_1 - O_1)/2]_{C7H5} - i\sin[2\pi(\omega_1 - O_1)/2]_{C7H5}$$

$$A_5 = \cos[2\pi(\omega_5 - O_1)/2]_{C7H5} - i\sin[2\pi(\omega_5 - O_1)/2]_{C7H5}$$

$$A_6 = \cos[2\pi(\omega_6 - O_1)/2]_{C7H5} - i\sin[2\pi(\omega_6 - O_1)/2]_{C7H5}$$

$$A_7 = \{\cos[2\pi(\omega_7 - O_1)/2]_{23}] + i\sin[2\pi(\omega_7 - O_1)/2]_{23}]\ \prod_{k=8}^{12}\{\cos[\pi J_{7k}/2]_{23}] + i\sin[\pi J_{7k}/2]_{23}]\}^*$$

$$B_5 = \{\cos[2\pi(\omega_5 - O_1)/2]_{27}] + i\sin[2\pi(\omega_5 - O_1)/2]_{27}]\}^*\ \prod_{k \neq 2,5,7}\{\cos[\pi J_{5k}/2]_{27}] + i\sin[\pi J_{5k}/2]_{27}]\}$$

| Simulated Fidelity | State |
|---|---|
| 1 | $\rho_1 = Z_7$ |
| 1 | $\rho_2 = Z_2 Z_4 Z_5 Z_6 Z_7$ |
| 1 | $\rho_3 = Z_1 Z_2 Z_3 Z_4 Z_5 Z_6 Z_7$ |
| 0.95 | $\rho_4 = Z_1 Z_2 Z_3 Z_4 Z_5 Z_6 Z_7 Z_8 Z_9 Z_{10} Z_{11} Z_{12}$ |
| 0.9511 | $\rho_5 = \prod_{i=1}^{12} I_i^+ + \prod_{i=1}^{12} I_i^-$ |
| 0.8717 | $\rho_6 = (A_1 A_5 A_6 I_1^+ I_2^- I_3^- I_4^- I_5^+ I_6^+ I_7^- + A'_1 A'_5 A'_6 I_1^+ I_2^+ I_3 I_4^+ I_5^- I_6^- I_7^+)|00000\rangle$ |
| 0.8570 | $\rho_7 = (A_1 A_5 A_6 A_7 I_2^+ I_5^- I_7^- + A'_1 A'_5 A'_6 A'_7 I_2^- I_5^+ I_7^+)|000000000\rangle$ |
| 0.8570 | $\rho_8 = (A_1 A_5 A_6 A_7 B_5 I_7^- + A'_1 A'_5 A'_6 A'_7 B'_5 I_7^+)|000000000000\rangle$ |

Figure 4.4: Fidelities and states at different stages of the pseudo-pure state preparation. $I_{x,y} = \sigma_{x,y}/2$, where, $\sigma_{x,y}$ are Pauli-$x, y$ matrices. $\omega_i$ is the chemical shifts of the $i^{th}$ spin, and $O_1$ is the frequency of the rotating frame. J refers to the coupling strength between the nuclei mentioned as the subscript.

labeled $\rho_4$ in Fig. 4.3. This part of the circuit is shown in Fig. 4.5c and MQFC optimization is utilized to reach 12-coherent state ($Z^{\otimes 12}$) from $Z^{\otimes 7} \bullet I^{\otimes 5}$. First, let us clarify that all other pulses except the MQFC pulse throughout our experiments are local rotations, which are generated from a subsystem-based gradient ascent pulse engineering (SSGRAPE) approach [45]. It is a technical improvement of the original GRAPE for our particular implementation, but does not address its poor scalability issue.

We would like to stress at first that SSGRAPE is still a classical algorithm and thus cannot address the scalability issues of GRAPE. Even though, SSGRAPE is an important modification to the original GRAPE algorithm, which can improve the timescale of calculating GRAPE pulses dramatically by defining subsystems based on the Hamiltonian of the molecule. For example, in our 12-qubit system, we define two subsystems each consisting of six spins, $S_A$ consisting of ($C_1$, $C_2$, $C_3$, $H_2$, $H_3$, $H_4$) and $S_B$ consisting of ($C_4$, $C_5$, $C_6$, $C_7$, $H_1$, $H_5$). This division of system is artificial, in the sense we assume none of the spins is $S_A$ have coupling with spins in $S_B$. From Fig. 4.2 and the relevant parameters, it can be seen that the two subsystems are isolated to a good approximation. Both internal and external Hamiltonians in $S_A$ and $S_B$ can be determined by tracing out the other subsystem. For a target operator, say $U_{tar} = R_x^1(\pi/2)$, it can be decomposed into two operators

$$U_{tar}^A = R_x^1\left(\frac{\pi}{2}\right), \quad U_{tar}^B = I, \tag{4.12}$$

where $U_{tar}^A$ and $U_{tar}^B$ are unitary operators of dimension $2^6 \times 2^6$, and $U_{tar} = U_{tar}^A \otimes U_{tar}^B$. Therefore, the 12-qubit GRAPE optimization problem can be treated as two 6-qubit problems, and SSGRAPE attempts to optimize a shaped pulse which can realize $U_{tar}^A$ and $U_{tar}^B$ simultaneously. In brief, the SSGRAPE technique greatly reduces the computation time since the optimization space is of two subspaces of 6-qubits rather than a 12-qubit space. The problem scales exponentially with the number of qubits, hence two 6-qubits space is much more faster. It is worth emphasizing that it does not fundamentally solve the scalability issue.

Another requirement of adopting SSGRAPE is that the target unitary operator can be effectively decomposed using subsystems and does not involve interactions between subsystems. In our 12-qubit experiment, this condition holds for every operator. We list all the SSGRAPE-optimized shaped pulses that are needed in the experiment, as shown in Table 4.1. We also simulated the fidelity of each pulse in the full 12-qubit system. That is, each pulse was found using SSGRAPE in the two 6-qubit subsystems, but then simulated on the full system. All local pulses are over 99.7% fidelity in simulation, which demonstrates that SSGRAPE is a valid pulse searching method for our 12-qubit system. What makes the MQFC scheme remarkable is that, it does not involve the computationally
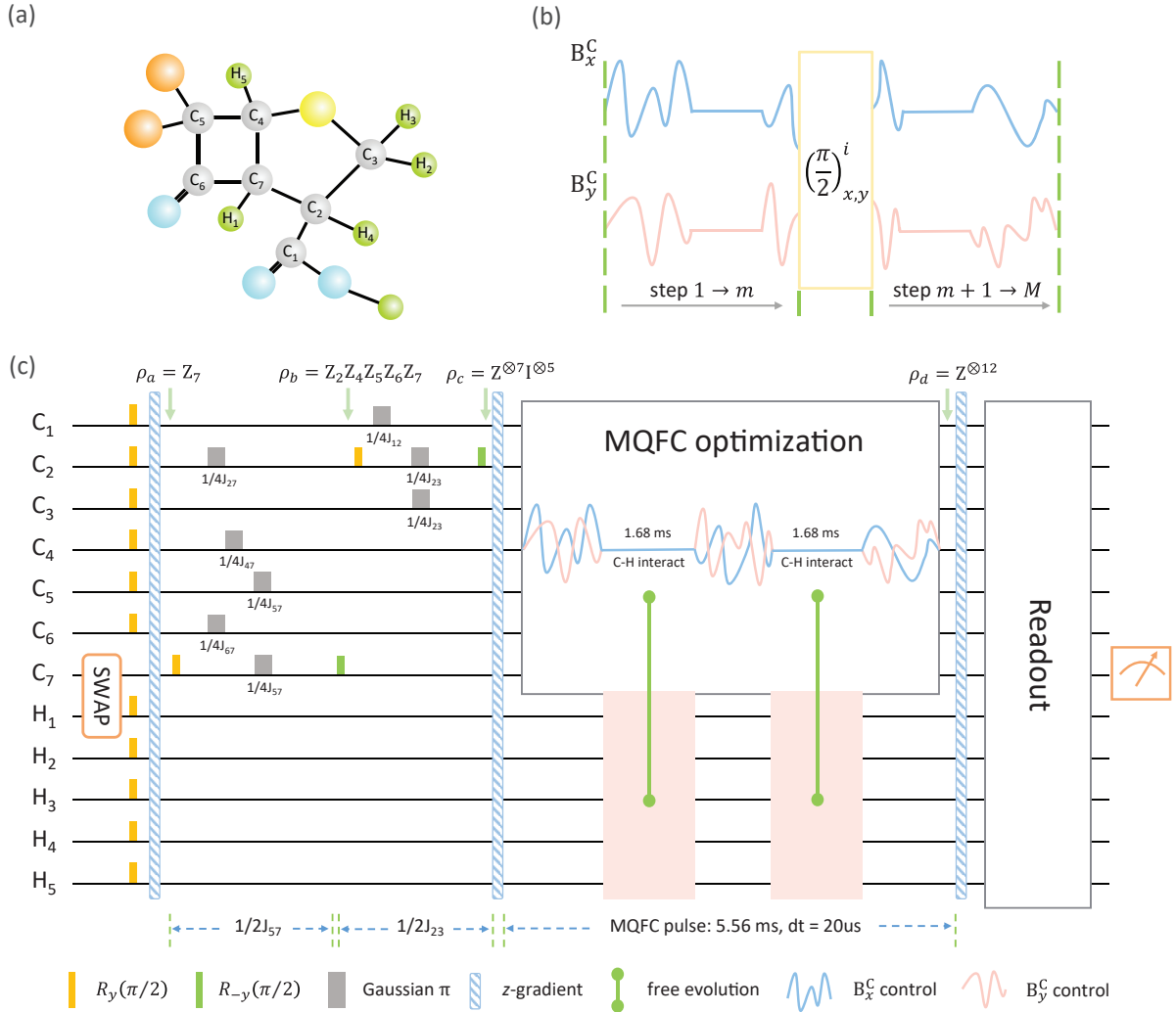
Figure 4.5: MQFC scheme in creating 12-coherence. **a** Molecular structure of the 12-qubit quantum processor. **b** Schematic of measuring the $m$-th step gradient $g_{x,y}[m]$. A $\pi/2$ rotation about $x(y)$-axis for qubit $i$ is inserted between the $m$-th and $(m+1)$-th slices. **c** Quantum circuit that evolves the system from the thermal equilibrium to 12-coherence, where MQFC is applied on 7-coherence $Z^{\otimes 7}I^{\otimes 5}$.

40

| Operator | Length | Simulated Fidelity | No. of Slices | $\Delta t$ |
|---|---|---|---|---|
| $C_7H_5 - SWAP$ | 8 ms | 99.0% | 400 | 20 $\mu$s |
| $R_y^{1-6,8-12}(\pi/2)$ | 1 ms | 99.8% | 100 | 10 $\mu$s |
| $R_y^7(\pi/2)$ | 1 ms | 99.9% | 100 | 10 $\mu$s |
| $R_x^2(\pi)$ | 2 ms | 99.8% | 200 | 10 $\mu$s |
| $R_x^6(\pi)$ | 2 ms | 99.8% | 200 | 10 $\mu$s |
| $R_x^4(\pi)$ | 2 ms | 99.7% | 200 | 10 $\mu$s |
| $R_x^{5,7}(\pi)$ | 2 ms | 99.8% | 200 | 10 $\mu$s |
| $R_{-y}^7(\pi/2)$ | 1 ms | 99.9% | 100 | 10 $\mu$s |
| $R_y^2(\pi/2)$ | 1 ms | 99.9% | 100 | 10 $\mu$s |
| $R_x^1(\pi)$ | 2 ms | 99.8% | 200 | 10 $\mu$s |
| $R_x^{2,3}(\pi)$ | 2 ms | 99.8% | 200 | 10 $\mu$s |
| $R_{-y}^2(\pi/2)$ | 1 ms | 99.9% | 100 | 10 $\mu$s |

Table 4.1: Shaped pulse optimized by SSGRAPE during the 12-coherence creation. The pulses are listed in the order of their appearances in Fig. 2(c). Although the pulses are found with the subsystem method, the fidelities reported here are calculated on the full 12-qubit system.

expensive classical simulation of the $2^{12}$-dimensional quantum dynamics in the course of optimization.

For our optimization task, GRAPE is a powerful tool, but handling 12 qubits is near the limit of capability for a typical laptop computer. In contrast, MQFC is capable of overcoming this difficulty in certain cases. Taking our experiment as an example, MQFC is able to solve the problem of finding a control field that evolves single-coherence $ZI^{\otimes 11}$ into 12-coherence $Z^{\otimes 12}$ in a time that scales linearly with the number of qubits. The entire experimental procedure is depicted in Fig. 4.5c.

First, we prepare 7-coherence $Z^{\otimes 7}I^{\otimes 5}$ on the seven $^{13}$C spins, using the sequence in Fig. 4.5c before the *MQFC optimization* box. This procedure, benchmarked in our previous work [56], is mainly done with the aid of SSGRAPE. Subsequently, we create $Z^{\otimes 12}$ via MQFC on the quantum processor, which is the main focus of this work. We attempt to optimize a control field, namely a shaped radio frequency (r.f.) pulse, to evolve the system from the input $\rho_i = Z^{\otimes 7}I^{\otimes 5}$ to the output $\rho_f = Z^{\otimes 12}$. Our control field, as shown in the *MQFC optimization* box, is divided into five parts: three parts to realize local rotations, and two free evolutions to let $^{13}$C qubits interact with $^1$H qubits for the purpose of generating higher coherence. The circuit shown in Fig. 4.3 going from state $\rho_3 \to \rho_4$ have three sections of local rotations and two free evolutions. This served as a guess for this sequence. The whole control field is digitized into $M = 278$ slices with $\Delta t = 20$ $\mu$s width, while 110 slices are for three sub-pulses and 168 slices remain zero to realize the

two 1.68 ms free evolutions. The total dynamics of the pulse is given by $U_1^M$ in Eq. (4.2).

The fitness function is defined as $f = tr(\rho_f \tilde{\rho})$, a metric for the control fidelity, where $\tilde{\rho} = U_1^M(\rho_i)$ is the experimental state and $\rho_f = Z^{\otimes 12}$ is the target. In our experiment, only one measurement of the expectation value of $\langle Z^{\otimes 12} \rangle$ suffices to attain $f$ after each iteration. If $f$ does not hit our preset value with the current control field, we navigate the control field along its gradient $g$. In fact, to measure $g_x[m]$ (the same for $g_y[m]$) which is the gradient of slice $m$, we just need three steps: insert a local $\pm\pi/2$ pulse on every qubit about $x$-axis between slice $m$ and $m+1$; apply this new control field to the initial state $\rho_i$ and measure $f$ (see Fig. 4.5b); compute $g_x[m]$ by directly combining these $\pm\pi/2$-inserted results via Eq. (4.11). As long as the accurate local $\pm\pi/2$ pulses are available for each qubit, $g$ can be measured on a quantum processor. In experiment, we have designed a 1 ms $\pi/2$ pulse on every $^{13}$C nucleus with the simulated fidelity over 99.7%. Having the gradient, we can update the control field and continue the MQFC procedure until a desired $f$ is attained.

### 4.3.2    Direct observation of 12-coherence.

After the preparation of the 12-coherent state, the next step is to observe it. In NMR spectroscopy, multiple coherence is hard to be observed directly in a one-dimensional spectrum, i.e., by flipping the target spin to the $x$-$y$ plane while others remain in Z. If all coupling between the target spin and other spins can be resolved, such observation is feasible. For example, in a two-qubit system, we can flip spin one to X to observe ZZ. In fact, XZ can be written as

$$XZ = X \otimes |0\rangle\langle 0| - X \otimes |1\rangle\langle 1|. \tag{4.13}$$

The first term $X \otimes |0\rangle\langle 0|$ leads to a positive peak at $\nu_1 - J_{12}/2$ in the spectrum, as the $J$-coupling term shifts the frequency of qubit 1 by $-J_{12}/2$. Analogously, the second term $X \otimes |1\rangle\langle 1|$ leads to a negative (due to the minus sign before the term) peak at $\nu_1 + J_{12}/2$. Generally, these two peaks can be resolved in the spectrum as long as $J$ is large enough to separate them in frequencies. However, to observe multiple coherence, this requirement is of great challenge, since all $J$-couplings between the target spin and other spins should be sufficiently large to prevent the annihilations of positive and negative peaks. As a result, two-dimensional spectra and special techniques are usually employed to observe multiple coherence in conventional NMR spectroscopy.

For the purpose of NMR quantum computing, it is certainly better if one can read out multiple coherence directly in a one-dimensional spectrum, as one-dimensional spectrum reflects the state information more intuitively and reduces experimental running time
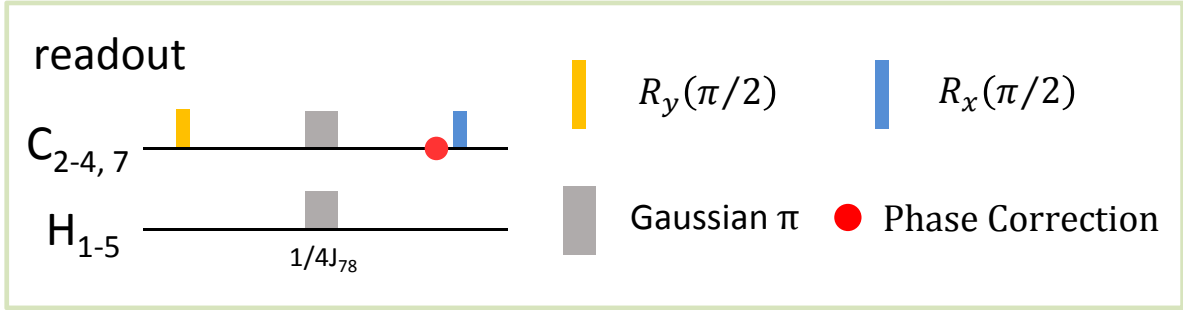
Figure 4.6: Readout sequence to boost the SNR of the $C_7$ spectrum. It transforms the $^1H$ spins from Z to identity and thus enables the decoupling of $^1H$ channel. The phase correction compensates for the chemical shift evolutions, after which all relevant spins are along the $y$-axis. In principle, this technique improves the SNR by a factor of 32, and makes the measurement of $f$ or $g$ practical using one scan.

remarkably compared to the two-dimensional spectroscopy. In our 12-qubit processor, although there are a few couplings as small as 0.01 Hz, a direct observation of 12-coherence $Z^{\otimes 12}$ is still available on $C_7$. Figure 4.7a exhibits a strong agreement between experimental observation 12-coherence with merely 32 scans and the simulation, after rescaling the experimental result by 1.21 times to compensate for decoherence. Our experiment provides a valid evidence that our 12-qubit processor possesses excellent individual controllability and the potential to be a universal 12-qubit quantum processor.

## 4.3.3 Readout sequence.

Although the direct observation of 12-coherence with 32 scans in Fig. 4.7a demonstrates our control precision, it is not suitable for the many experimental runs during the optimization since 32 scans leads to a great time cost. One solution is to decouple the five $^1H$ spins to boost the signal-to-noise ratio (SNR) by $2^5 = 32$ times, which exactly compensates for the required scan number. We have designed a readout pulse sequence to realize it as shown in Fig. 4.6.

The local pulses in the readout sequence are computed by SSGRAPE, and the sequence is implemented before every measurement. The phase correction is a $z$-rotation to neutralize the unwanted chemical shift rotation during the free evolution. If the state is $Z^{\otimes 12}$, the five $^1H$ spins will be evolved to the identity state after the readout sequence, and the

43

decoupling of $^1$H leads to the C$_7$ spectrum as shown in Fig. 4.7b, which is measured with a single scan. We then use spectrum fitting to obtain the signal's amplitude and phase, and thus the value of $\langle Z^{\otimes 12} \rangle$.

This readout sequence induces errors in terms of decoherence and pulse imperfections. For the former one, through our simulation we find that it leads to about 30% signal loss, which is reasonable since multi-coherence is exceptionally vulnerable to decoherence. Therefore, this factor is taken into account for all the measurement results, that is, the measured values are rescaled by about 1.3. With respect to the pulse imperfection, it consists of two parts: the imperfection of the sequence itself, i.e., some approximations when we design this simple readout sequence, and the infidelities in implementing the pulses. In total, 3.5% error arises in simulation. We use this value as the uncertainty of the experimental value of $\langle Z^{\otimes 12} \rangle$, namely, the error bars in Fig. 4.7c.

### 4.3.4 Experimental results.

Figure 4.7b shows the spectrum of $\tilde{\rho}$ after the readout stage for each odd iteration. The peak intensities correspond to the value of $f = tr(Z^{\otimes 12}\tilde{\rho})$, which clearly shows that MQFC increases $f$ during the optimization. This demonstrates that MQFC is a practical technique for designing control fields in large quantum systems.

Our experiment also exhibits MQFC's ability of correcting unknown experimental errors. To demonstrate this improvement, we implement another group of 12-coherence-creating experiments, where all experimental settings are the same except that the pulse is generated from the classical SSGRAPE method other than the MQFC approach. We then compare these two groups of experiments. Figure 4.7c illustrates the result of SS-GRAPE and MQFC pulses both in simulation and experiment. Focusing on the final result at iteration 9 in Fig. 4.7d, in experiment SSGRAPE finally creates a 12-coherence with $f = 0.703 \pm 0.034$, whereas MQFC pulse creates $f = 0.795 \pm 0.027$. This experimental improvement (nearly 10%) disagrees with simulation, as in simulation MQFC (0.830) is even worse than SSGRAPE (0.931). The errors(standard deviation) were obtained by repeating the experiment few number of times and taking in account the noise.

Considering that MQFC is a feedback-control process, some incomplete knowledge of the experimental quantum process, such as the nonlinearity of the pulse generator or imprecision of the molecular Hamiltonian, may be inherently corrected during the optimization. Indeed, the experiment clearly suggests that MQFC is advantageous in terms of correcting errors from unknown sources. Furthermore, we simulate the decoherence effect during the procedure, and find that the upper bound of $tr(Z^{\otimes 12}\tilde{\rho})$ in the presence of dephasing noise is about 0.824. Note that our MQFC result finally reaches 0.795, which is very close to this bound, demonstrating that our control of this 12-qubit processor is close to the theoretical prediction after accounting for decoherence.

To numerically simulate the decoherence effect in our 12-qubit system, we first make the following assumptions: the environment is Markovian; only the $T_2^*$ dephasing mechanism is taken into account since $T_1$ effect is negligible in our circuit; the dephasing noise is independent between all qubits; the dissipator and the total Hamiltonian commute in each pulse slice as $\Delta t = 20$ $\mu$s is small. With these assumptions, we solve the master equation in two steps for each $\Delta t$: evolve the system by the propagator in Eq. (4.2), and subsequently apply the dephasing noise for $\Delta t$ which is an exponential decay of off-diagonal elements in the density matrix. The typical length of simulating our 12-qubit experiment in the presence of dephasing noise is in the magnitude of days on a desktop computer. The simulation shows that at most $F_{dec} = 0.824$ of $Z^{\otimes 12}$ can be achieved with the 5.56 ms MQFC pulse applied on $Z^{\otimes 7}I^{\otimes 5}$, which is reasonable as high-order coherence is very
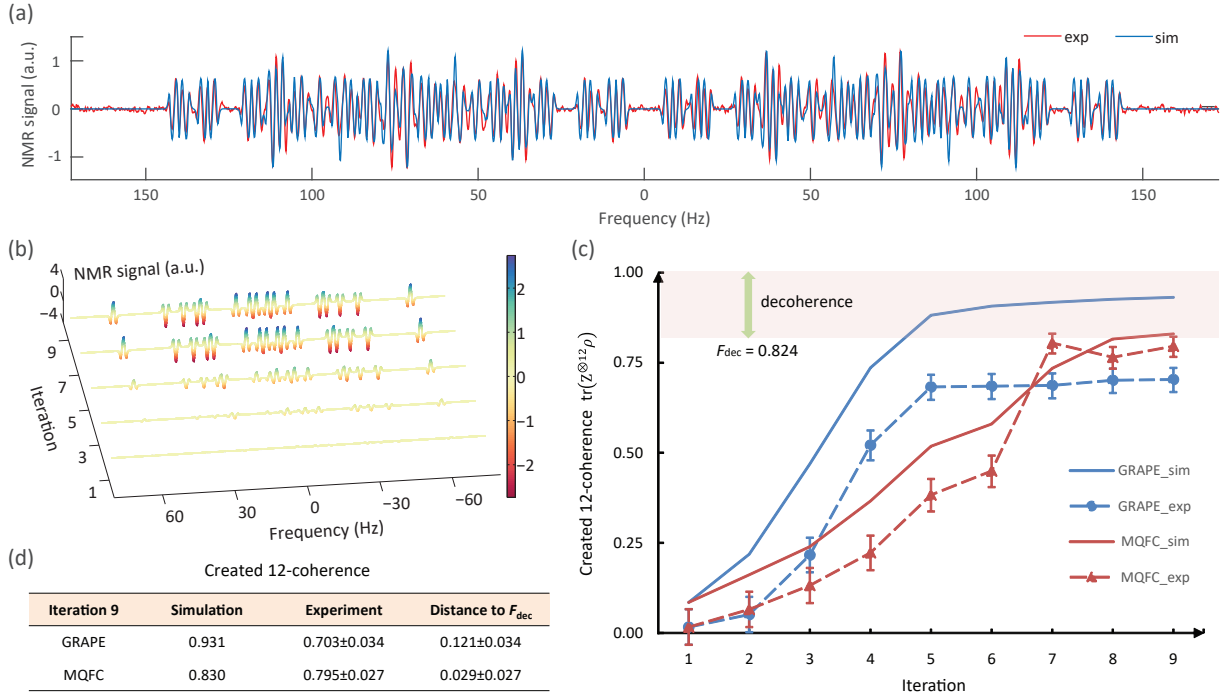
Figure 4.7: Experimentally created 12-coherence using MQFC. **a** Direct observation of the created 12-coherence in one-dimensional NMR spectrum (red), where $C_7$ is the probe qubit. Simulated spectrum (blue) is also plotted. The experimental result is rescaled by 1.21 times to compensate for the decoherence effect for better visualization. **b** Spectra of 12-coherence after each odd iteration during the MQFC optimization. Unlike the direct observation, a readout technique is applied to gain a higher resolution. A color scale indicates peak intensities. The height of the peaks is proportional to the value of created 12-coherence. **c** Comparison between GRAPE (blue) and MQFC (red) optimizations, both in simulation (solid; without decoherence accounted) and experiment (dashed). $F_{dec}$ is the numerical simulation of decoherence during the 12-coherence creation. Compared to the GRAPE algorithm, MQFC optimization is worse in simulation, but better in experiment. The error bars are plotted by the infidelity of the readout pulse. **d** Results at iteration 9. The experimental 12-coherence reaches 0.795 using MQFC which approaches the $F_{dec} = 0.824$ bound, while GRAPE only leads to 0.703 (i.e., 0.121 lower than $F_{dec}$) in experiment.

46

vulnerable to the dephasing noise. Alternatively speaking, the upper bound of the MQFC experimental result is 0.824, since the optimization procedure does not include the function of robustness against dephasing noise yet.

## 4.4 Discussion

### 4.4.1 Scalability.

One major concern about control methods is their scalability with the number of qubits $n$. Our MQFC protocol involves a single experiment to measure $f$ and $4nM$ experiments to measure $g$ for each iteration, where $n$ is the number of qubits and $M$ is the number of slices the time domain is discretized into. Assuming each experiment takes $\tau_{exp}$ time, the MQFC in total consumes $T_{it} = (4nM + 1)\tau_{exp}$ for each iteration. For comparison, one has to deal with massive $2^n \times 2^n$ matrix multiplications and exponentials using GRAPE on a classical computer. The speed-up comes from the fact that MQFC utilizes the evolution of the quantum system instead of computing the system's dynamics when evaluating $f$ and $g$.

For other potential problems when scaling up the GRAPE technique, MQFC confronts similar difficulties, such as how to effectively represent a generic target state, how to choose a good initial guess, how to determine the pulse parameters before optimization, and how many iterations are needed to reach a satisfactory fidelity. Unfortunately, experimental observation of running time versus number of qubits is not likely in NMR, since changing the number of qubits would usually require a different sample with different characteristics. So we cannot experimentally compare the scaling of MQFC versus GRAPE, instead we must be satisfied with the fact that MQFC performs well at the 12-qubit level and should theoretically scale better than GRAPE under standard assumptions.

One may also ask if there could be other classical algorithms that scale as well (or better than) MQFC. This question remains open, but it seems very unlikely – the gradient calculation is based on the dynamics as shown in Eq. (4.2), i.e., the expected classical algorithm needs to simulate the dynamics of an NMR system in an efficient way. Even when boiling down to our particular state engineering task, as far as we can tell, there is no known numerical method [57, 58, 59] to simplify such an optimization, despite extensive work on the subject since the early days of experimental quantum computing. Moreover, MQFC can correct unknown errors to some extent, while open-loop algorithms should require knowledge about the noise spectrum in advance, which is usually impractical for large quantum systems. In this sense, another potential application of MQFC is to demonstrate the quantum computing supremacy [60], where initial endeavors have been made in other systems, for example in a recent five-photon boson sampling experiment [61].

### 4.4.2 Comparison with previous work.

MQFC was originally introduced in Ref. [5] where it was implemented on a 7-qubit NMR processor. There are two significant improvements in our work. First, our work clearly demonstrates the superiority of MQFC in correcting unknown errors with around 10% fidelity boost compared to the best classical optimization result, while in the 7-qubit experiment no improvement was observed. The reason could be that the characterization of a 7-qubit system is much more accurate than a 12-qubit one, indicating that MQFC should be more powerful when dealing with large systems as the knowledge of larger systems are more likely to be incomplete. Second, our 12-qubit experiment lies at the cutting edge of present experimental quantum computing, and the capability of individual controls at this qubit number is state-of-the-art. As a comparison, in a recent work [62], the 10-qubit entanglement in a superconducting circuit is created with fidelity 0.668 using *global* control. Moreover, we demonstrated that at the 12-qubit level, the algorithm is already fast enough to justify its use as a tool in the lab. Other experiments where a large number of qubits were entangled are [6, 7, 8].

In summary, we have created a 12-coherence state on an NMR quantum processor using MQFC. Our experimental procedure and result, in particular the direct observation of 12-coherence with one qubit as the probe, signify the capability of our quantum processor to serve as a universal 12-qubit quantum processor with high-fidelity individual controls on each qubit. In terms of control field optimization, our experiment demonstrates two superiorities in efficiency and experimental performance of MQFC beyond its classical counterpart. MQFC requires a running time that scales linearly with the number of qubits, and yields about 10% improvement compared to the best result via classical optimization. This optimization approach could be exceptionally useful in a large system with incomplete characterization, and is readily transferable to other systems such as superconducting circuits or nitrogen-vacancy centers in diamond. We expect that, as experiments involving more than 10 qubits become more common, quantum feedback methods such as MQFC will become standard tools in quantum computing labs.

# Chapter 5

# Closed loop quantum control

## 5.1 Introduction

Quantum computers are believed to outperform classical computers in solving certain problems [63]. However, turning theory into practice will require quantum processors that are resilient to noise. Fault tolerance theory assumes reasonable noise models and requires low error rates below a threshold level. Quantum optimal control [64, 44, 65] is a useful tool to devise high fidelity control pulses that satisfy the threshold condition, and great progress has been made in different device architectures, e.g. superconducting qubits, quantum dots, ion traps, and nitrogen-vacancy centers [66, 67, 68, 69].

There are two broad classes of quantum optimal control: open-loop and closed-loop. Open-loop quantum control typically relies on accurate modelling of the system Hamiltonian and control parameters, therefore it may no longer produce expected result in realistic settings, e.g. effects due to the hardware tranfer function [70, 71, 72]. In such cases, on one hand, open-loop optimization considering uncertainties in system and control Hamiltonians is being studied [73]; on the other hand, better performance can be achieved from closed-loop quantum control [74, 64, 75, 76, 77]. Moreover, closed-loop quantum control combines the use of both classical and quantum resources in a way that the calculation remains efficient when the size of the system Hilbert space becomes classically intractable.

In the context of closed-loop quantum optimal control, both gradient-based and gradient-free search algorithms have been investigated [9, 74, 76, 77, 78, 79, 80]. Generally speaking, gradient-free algorithms converge slowly compared to gradient-based algorithms [81]. Gradient-based algorithms can be classified into two categories: model-free [9] and model-

dependent [74, 79]. In their hybrid quantum-classical approach (HQCA), Li et al. [74] developed a scheme for measuring gradients based on the knowledge of the system Hamiltonian model, assuming a flat hardware transfer function. HQCA was successfully demonstrated in liquid-state nuclear magnetic resonance (NMR) [74, 75] where the transfer functions are relatively flat over the control frequency range, and improvement on control fidelity compared to open-loop control was observed. Ferrie et al. [9] utilized a model-free algorithm stemming from the finite-difference (FD) method which uses finite differences to approximate derivatives/gradients. They also compared their FD method with gradient-free simplex or Nelder-Mead algorithm [76, 77, 78] and numerically showed that their method is more robust to control noise and requires fewer resources.

We experimentally investigated the two gradient-based closed-loop quantum control approaches, HQCA and FD, in a solid-state electron spin resonance (ESR) two-qubit system. The ensemble two-qubit system consists of hyperfine coupled electron and nuclear spins. This system combines advantages of electron spins and nuclear spins, i.e. large thermal polarization and fast control of electron spins, and long coherence time of nuclear spins. It has been shown that universal quantum control using only microwave excitation in this system is possible [82, 46, 83]. However, achieving high fidelity quantum control in a bulk ESR system is challenging. One reason is the limited frequency bandwidth of a conventional microwave resonator [72]. Hence, when designing optimal control pulses for ESR systems, the hardware transfer function cannot usually be ignored. The HQCA method does not explicitly consider the transfer function, so it is important to test its performance experimentally and compare it with the FD method, which in principle accounts for the transfer function. We used two basis sets for the FD method, linear and Slepain [84, 85, 86]. The Slepian basis is designed for limited control bandwidth, and therefore can give further insights regarding the effects of the transfer function bandwidth. Finally, open-loop quantum optimal control using the first-order gradient ascent method was also implemented for comparison. In general, higher fidelities were observed with closed-loop control. Although the HQCA and FD methods showed similar experimental performance, we used simulations to find favorable conditions for each method. When the error in our system is dominated by the transfer function, the FD method performs better. When the error in our system is dominated by the randomly fluctuating measurement noise which results in errors in the measured gradients, the HQCA method performs better.

## 5.2 Two methods for deriving gradients

The control problem we consider here is to prepare a desired state starting from a given initial quantum state. We choose the state fidelity defined in Eq. (5.1) as the metric to evaluate the control quality,

$$F = \text{Tr}\left[U(T)\rho_i U(T)^\dagger \rho_f\right]/2^n, \tag{5.1}$$

where $\rho_i$ and $\rho_f$ are the initial and target states, respectively, $T$ is the total duration of the control sequence, and $n$ is the number of qubits. $U(t)$ is the unitary evolution of the spin system in the presence of the system's internal Hamiltonian $H_0$ and control Hamiltonian $H_c\left(\mathbf{u}(t)\right)$, and hence satisfies:

$$\dot{U}(t) = -i\left[H_0 + H_c\left(\mathbf{u}(t)\right)\right]U(t)$$
$$U(0) = I^{\otimes n}. \tag{5.2}$$

Here $\mathbf{u}(t)$ is the collection of control parameters, e.g. control field amplitudes, and $I$ is the 2-dimensional identity operator. The goal is to maximize the fidelity defined in Eq. (5.1).

Gradient ascent pulse engineering (GRAPE) [44] is a well-known iterative numerical method to solve the optimization problem, where at the $q^{\text{th}}$ iteration the control parameters are updated by

$$\mathbf{u}^{q+1} = \mathbf{u}^q + c_q \mathbf{g}^q, \tag{5.3}$$

where $\mathbf{g}^q$ is the gradient of $F$ with respect to the control parameters $\mathbf{u}^q$ and $c_q$ is an adaptive step size. Convergence happens at certain local optima and the solution can be accepted once the desired $F$ is realized with the parameters $\mathbf{u}^q$. In this paper, we refer to a class of numerical optimization methods which uses classical resources to calculate the fidelity $F$ and its gradients $\mathbf{g}^q$ as open-loop quantum optimal control.

One drawback of open-loop quantum optimal control is that it relies on accurate determination of $H_0$ and $H_c$, which can be difficult to obtain in real systems. Moreover, numerical methods become impractical when the size of the system is larger than a handful of qubits [75]. To address such issues, Li et al. proposed a closed-loop quantum optimal control scheme known as HQCA which utilizes the quantum system under control as a quantum simulator in calculating the gradient $\mathbf{g}^q$. In the following, we briefly describe the method.

The HQCA approach can be applied to many quantum systems. Here, we take the

spin-based magnetic resonance as an example. Consider a common control Hamiltonian in magnetic resonance systems, where the control magnetic field is in the transverse plane relative to the static magnetic field, i.e. in the $x$-$y$ plane:

$$H_c(m) = \Sigma_{l=1}^{N} \left[ u_{x,l}(m)\sigma_x^l + u_{y,l}(m)\sigma_y^l \right], \tag{5.4}$$

where $N$ is the number of spins that can be excited by the resonant alternating current (AC) magnetic field, $\sigma_\alpha^l$ is the Pauli operator of the $l^{\text{th}}$ spin, and $u_{\alpha,l}(m)$ is the piecewise constant control amplitude ($\alpha = x$ or $y$) for the $m^{th}$ piece. The unitary generated by the total Hamiltonian $H=H_0+H_c$ is then given by

$$U(T) = \Pi_{m=1}^{M} e^{-i\Delta t[H_0 + H_c(m)]}, \tag{5.5}$$

where $\Delta t$ is the time step and $M$ is the total number of segments of $u_{\alpha,l}(m)$. The gradient at the $q^{\text{th}}$ iteration, $\mathbf{g}^q$, is then defined as the partial derivative of $F$ with respect to $u_{\alpha,l}$:

$$\mathbf{g}^q \equiv \left[ \frac{\partial F}{\partial u_{x,l}(m)}, \frac{\partial F}{\partial u_{y,l}(m)} \right]. \tag{5.6}$$

As proposed by Ref. [74], combining Eqs. (5.1) and (5.5) gives

$$\frac{\partial F}{\partial u_{\alpha,l}(m)} \approx \Delta t \frac{\text{Tr}\left[\rho_{+\alpha}^l(m)\rho_f\right] - \text{Tr}\left[\rho_{-\alpha}^l(m)\rho_f\right]}{2^n}, \tag{5.7}$$

where $\rho_{\pm\alpha}^l(m) = U_{m+1}^M R_\alpha^l(\pm\frac{\pi}{2})U_1^m \rho_i \left[U_{m+1}^M R_\alpha^l(\pm\frac{\pi}{2})U_1^m\right]^\dagger$. This means that $\mathbf{g}^q$ can be experimentally measured by inserting $\pi/2$ rotations $R_\alpha^l(\frac{\pi}{2})$ and $R_\alpha^l(-\frac{\pi}{2})$ into the control pulse $U$. Since $\mathbf{g}^q$ is a $2NM$ dimensional vector, if we consider one experiment as containing the preparation of an initial state, implementation of the pulse and measurement over a chosen basis element, then at each iteration $4NMP$ experiments are required to obtain $\mathbf{g}^q$. Here, $P$ is the number of Pauli elements with non-zero coefficients that compose the target state $\rho_f$.

Figure 5.1 shows the schematic of how closed-loop quantum optimal control is performed iteratively. While the HQCA method is a good choice for large systems with uncertain Hamiltonians [74, 75], it does not account for hardware transfer function. In case the bandwidth of the hardware transfer function is much narrower than the intended bandwidth of the inserted $\pi/2$ rotation pulse, the scheme can fail. Even if the $\pi/2$ pulse functions properly, HQCA measures $\partial F/\partial\tilde{u}$ instead of $\partial F/\partial u$ (see Fig. 5.1), where $\tilde{u}$ represents the distorted pulse. Compared to the radio-frequency regime typical of NMR, the microwave
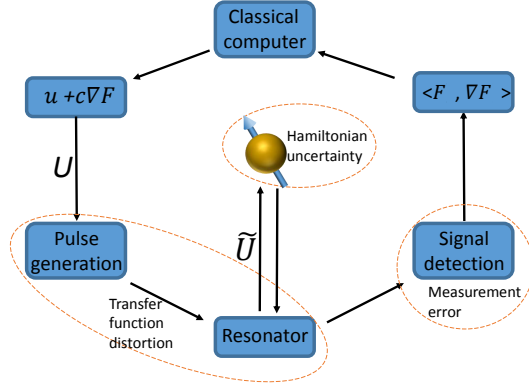
Figure 5.1: Flow diagram of gradient-based closed-loop optimal control as applied to ESR. Arrows label the direction of information flow. Error sources are labeled using orange dash-line circles. Both the HQCA and FD methods can compensate for the control errors caused by the uncertainty in the system Hamiltonian. Theoretically, the FD method finds the gradient $\partial F/\partial u$, while HQCA finds the gradient $\partial F/\partial \tilde{u}$. The pulse shape represented by $\tilde{u}$ is distorted by the hardware.

transfer function relevant to ESR experiments tends to be much less uniform over the frequency range of interest. Thus, we consider another method of closed-loop control that can take these effects into account: the FD method. It uses finite differences to approximate the derivatives when an analytic expression of the gradient function is not available. If we write $\mathbf{u}^q = (u_{x,1}^q, u_{y,1}^q, \ldots, u_{x,N}^q, u_{y,N}^q)$ as the $q^{\text{th}}$ control amplitude parameters, $\mathbf{g}^q$ can be expressed as

$$
\mathbf{g}^q = \Sigma_k g_k^q \mathbf{v}^k, 1 \leq k \leq 2NM
$$
$$
g_k^q \approx \frac{F(\mathbf{u}^q + \Delta u_k^q \mathbf{v}^k) - F(\mathbf{u}^q - \Delta u_k^q \mathbf{v}^k)}{2\Delta u_k^q}. \tag{5.8}
$$

Here $\{\mathbf{v}^k\}$ is a basis set that spans the parameter space and $\Delta u_k^q$ is a properly chosen difference value [9]. In ref. [9] this properly chosen value is $\Delta u_k^q(j) = 1/(j+1)^{1/6}$, where $j$ is the iteration number. To obtain the complete gradient vector $\mathbf{g}^q$, similar to the HQCA method, a total of $4NMP$ measurements are needed at each iteration. As the gradients are estimated directly from state fidelity measurements, distortions of the pulse due to the transfer function are accounted for in the process. This method is useful when the hardware transfer function is strongly frequency dependent or is not accurately known.

In Ref. [9], the authors simulated a closed-loop (*in-situ*) optimization scheme based on the FD method. Instead of using a complete basis set per iteration, they acquired gradient and performed optimization only with one random element of the basis set at a time. This results in fewer experiments per iteration, but convergence is slow if the random elements are not well chosen. In this work, we use two different basis sets: the first is a complete basis set in the time domain with a dimension of $2NM$ (we call it the linear basis), and the second is the Slepian basis [84, 85, 86]. The Slepian basis can be constructed to have fewer elements than $2NM$ with narrower control bandwidth, and is thus suitable for applications when the bandwidth is experimentally limited. Roughly speaking, the Slepian basis set is a low-pass filtered version of the linear basis as the elements of the Slepian basis exhibit much smoother amplitude changes in the time domain compared to the linear basis.

## 5.3   Experimental Results

Experiments were carried out using a custom pulsed ESR spectrometer operating at X-band. An arbitrary waveform generation (AWG) enables pulse shaping, and a loop-gap resonator with Q~100 allows excitation over a bandwidth ~100 MHz [87]. The sample we use is a single crystal of unlabeled malonic acid ($CH_2(COOH)_2$), where paramagnetic defects are created by gamma-ray irradiation [83]. Since the carbon atoms are not spin labeled, all hyperfine couplings involve surrounding hydrogen atoms (I=1/2), and up to 8 have been observed [88]. The general spin Hamiltonian can be written as

$$H_0 = \mu_B \boldsymbol{B_0^T} \cdot \boldsymbol{g} \cdot \boldsymbol{S} + \sum_{i=1}^{8} \left( \boldsymbol{S^T} \cdot \boldsymbol{A^i} \cdot \boldsymbol{I^i} - \mu_n g_n \boldsymbol{B_0^T} \cdot \boldsymbol{I^i} \right), \tag{5.9}$$

where $\mu_B$ is the Bohr magneton, $\mu_n$ is the nuclear magneton, $\boldsymbol{B_0} = B_0 \hat{z}$ is the externally applied magnetic field, $\boldsymbol{g}$ is the g-tensor of the electron spin, $g_n$ is the g-factor of the nuclear spin, $\boldsymbol{S} = (\hat{S}_x, \hat{S}_y, \hat{S}_z)$ is the electron spin operator, $\boldsymbol{A^i}$ and $\boldsymbol{I^i}$ are the hyperfine tensor and nuclear spin operator for the $i^{\text{th}}$ nuclear spin, respectively (vectors are in bold). The hyperfine coupling to the $\alpha$-proton dominates, as it is about 10 times stronger than the second largest coupling. Therefore, we neglect all other protons and write a simplified, two-spin Hamiltonian:

$$H_0 = \omega_I I_z + A S_z I_z + B S_z I_x. \tag{5.10}$$

This Hamiltonian is written in the rotating frame of the electron and makes use of the secular approximation. Here $A$ and $B$ are the secular and pseudo-secular hyperfine cou-
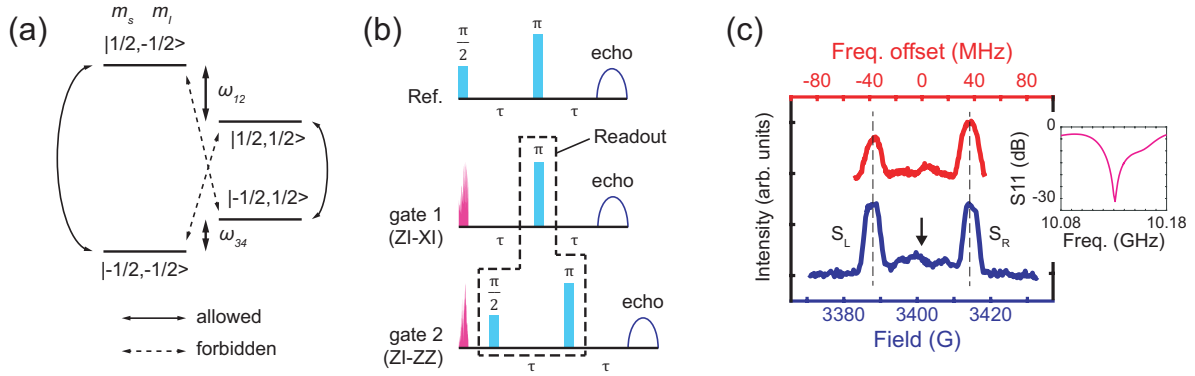
Figure 5.2: (a) Energy level diagram of the two-qubit system. Each level is designated by electron and nuclear spin quantum number, $m_s$ and $m_I$, respectively. (b) Pulse sequence used for the reference (spin echo), gate 1 (ZI to XI), and gate 2 (ZI to ZZ) measurement. For the reference and readout, 200 ns long square $\pi/2$ and $\pi$ pulses with excitation bandwidth of 5 MHz were used throughout the experiments, providing selective excitation of one allowed transition without affecting the other. The echo is formed after $\tau=1$ $\mu$s from the $\pi$ pulse. Phase cycling was implemented in gate 2 measurement to remove possible signal contributions from the transversal polarizations, which we do not want to measure. (c) ESR spectra acquired by sweeping the magnetic field (blue, lower trace) and frequency (red, upper trace) using the reference spin echo sequence. For the field swept spectrum, the microwave pulse frequency is fixed at the resonance frequency of the loop-gap resonator, determined from a separate microwave reflection (S11) measurement as shown in the inset. For the frequency swept spectrum, $B_0$ is fixed at 3401 G (denoted by the arrow in the figure). Two strong signals at 3401±14 G or ±36 MHz ($S_L$ and $S_R$) correspond to the resonance condition of the two allowed ESR transitions. The unequal intensities obtained in the frequency swept spectrum are due to the frequency dependence of the spectrometer's transfer function.

plings, respectively, and $\omega_I = \mu_n g_n B_0$ is the nuclear Zeeman frequency. At X-band where the strength of the static magnetic field ($B_0$) is around 0.34 T for $g \sim 2$, $|\omega_I| \sim 14.5$ MHz. Diagonalizing $H_0$ gives

$$H_0^d = \text{Diag} \left[ \frac{\omega_{12}}{2}, -\frac{\omega_{12}}{2}, \frac{\omega_{34}}{2}, -\frac{\omega_{34}}{2} \right]$$
$$|\omega_{12}| = \sqrt{(\omega_I + A/2)^2 + B^2/4}$$
$$|\omega_{34}| = \sqrt{(\omega_I - A/2)^2 + B^2/4}, \tag{5.11}$$

where the superscript '$d$' denotes the diagonal form. Figure 5.2(a) shows the energy level diagram for the hyperfine coupled electron-nuclear spin system. The nuclear frequencies $\omega_{12}$ and $\omega_{34}$ are given in Eq. (5.11). The hyperfine coupling is known to be strongly anisotropic [87], so the values of $A$ and $B$ depend on how the sample crystal is oriented with respect to $\boldsymbol{B_0}$. We chose an orientation in which $A \gg B$. Under such condition, it is more difficult to fully characterize the Hamiltonian experimentally compared to the cases when $A \sim B$. The uncertainty in the Hamiltonian provides a good testbed for comparing feedback control schemes.

As shown in Fig. 5.2(b), a spin echo sequence is utilized to read out the intensity of a particular ESR transition. When either the dc magnetic field, $B_0$, or the microwave frequency is varied to satisfy the resonance condition, strong peaks corresponding to the two allowed ESR transitions appear, as shown in Fig. 5.2(c). In addition, smaller signals from the forbidden transitions appear between the two strong allowed peaks.

From spectral fitting, the forbidden transition rates are estimated to be $<5\%$ of the allowed transition rates. The estimated range of $A$ and $B$ is $72 > |A| > 66$ MHz and $0 < |B| < 26$ MHz, where one constraint is that $|\omega_{12}| + |\omega_{34}| = 72$ MHz (separation of the two allowed transitions). Since the forbidden transition rates are small, no electron spin echo envelope modulation (ESEEM) signals were observed. The lack of information from an ESEEM experiment is a key reason that the Hamiltonian parameters cannot be determined more accurately in this orientation.

Finally, we test and compare open- and closed-loop quantum optimal control of two state-to-state gates on the two-qubit system described above. We denote the thermal equilibrium state by ZI, where the first (second) letter refers to the state of electron (nuclear) spin. Here, we use the deviation density matrix to describe a state, and X, Y, and Z stand for the Pauli matrices. Gate 1 is the transformation ZI$\rightarrow$XI, and gate 2 is the transformation ZI$\rightarrow$ZZ. Both target states only contain one Pauli element and thus $P=1$. Characterizing the control quality requires measurement of the final state. This is done

Step 1: Start with previous pulse

Step 2: For $k$=1:$k_{max}$, mesure $F^{k,\pm x}$

$k^{th}$    Ideally $R_x(\pm\pi/2)$

HQCA

Add or subtract $k^{th}$ basis vector in $x$-phase

FD          or

Linear        Slepian

Step 3: Compute gradients, $g_k \propto F^{k,+x} - F^{k,-x}$

Step 4: Sum over k to obtain final gradient $\mathbf{g}=\sum_k g_k \mathbf{v}^k$

*Waveforms corresponding to different basis sets $\mathbf{v}^k$

HQCA

Linear

Slepian

Step 5: Update pulse by adding $\mathbf{cg}$ to x-phase.
Similarly obtain gradient in y-phase.

Figure 5.3:    Process flow for optimizing closed-loop control.  Starting with the pulse obtained from previous iteration (Step 1; shown here is a square pulse as an example), two control qualities $F^{k,\pm x}$ are measured (Step 2) to calculate the gradient in a particular direction of a basis denoted as $\mathbf{v}^k$ (Step 3). For the HQCA method, a $\pm\pi/2$ rotation pulse around the $x$-axis ($R_x(\pm\pi/2)$; see Appendix B) is inserted at the $k^{th}$ segment. For the FD method, the pulse is perturbed by the addition/subtraction of a small amplitude vector proportional to the $k^{th}$ basis element in the $x$-phase. Steps 2 and 3 are repeated for all elements of the basis, and the final gradient is obtained by summing all gradients (Step 4). The pulse is updated by adding the final gradient in $x$-phase (Step 5). A similar procedure is carried out to obtain the final gradient in $y$-phase.  More details of the procedure, including information of different basis sets used, are given in the main text.
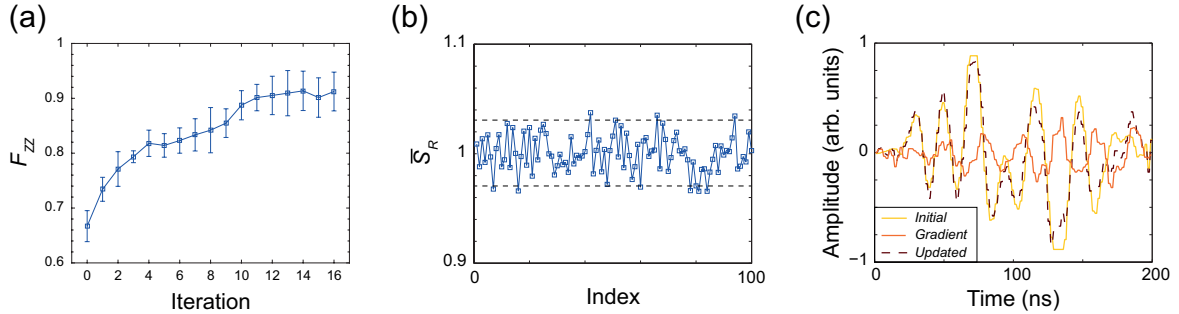
Figure 5.4: (a) $F_{\mathrm{ZZ}}$ as a function of the number of iterations (HQCA method). Here, the fidelity measurement for each pulse shape, together with the reference signal measurements, was repeated 5 times for the first 13 iterations and 50 times for the last 4 iterations. Each individual measurement was an average of 16,000 phase-cycled scans. The error bars indicate one standard deviation of the measurement results obtained over the repetitions (5 or 50). (b) Fluctuation of normalized reference signal intensity (here $\overline{S}_R$) during 100 repetitions. Dashed lines indicate $\pm 0.03$ deviation from the normalized mean. (c) Example of pulse update. The solid yellow (light gray) curve represents the initial $x$-phase shape. The solid orange (medium gray) curve is the experimentally measured gradient $\mathbf{g}$. The dashed brown (dark gray) curve is the updated pulse obtained by adding $c\mathbf{g}$.

via two separate, selective readouts of the allowed ESR transitions, which we denote $S_L$ and $S_R$ (see Fig. 5.2(b)). The selective readout is accomplished by fixing $B_0$ at the center of the spectrum and varying the pulse frequency using the AWG. To compensate for the transmission/receiver transfer function that is not flat, $S_L$ and $S_R$ must be properly normalized by their thermal reference signal intensity, $\overline{S}_L$ and $\overline{S}_R$. From Eq. (5.1) we can define the control quality for gates 1 and 2 as:

$$
\begin{aligned}
F_{\mathrm{XI}} &= \frac{1}{2}\left(S_L/\overline{S}_L + S_R/\overline{S}_R\right) \\
F_{\mathrm{ZZ}} &= \frac{1}{2}\left(S_L/\overline{S}_L - S_R/\overline{S}_R\right).
\end{aligned}
\tag{5.12}
$$

The minus sign in $F_{\mathrm{ZZ}}$ is due to the fact that the two allowed transition peaks have opposite sign in the ideal spectrum for the state ZZ. We note that while $F_{\mathrm{ZZ}}$ can be considered as the true state fidelity as defined in Eq. (5.1), $F_{\mathrm{XI}}$ should be treated as a relative measure only. The reason is that $F_{\mathrm{XI}}$ can be larger than 1 when gate 1 performs better in exciting the transitions than the square $\pi/2$ pulse used in the reference measurement (see Fig. 5.2(b)).

Figure 5.3 shows the general procedure of the closed-loop gate finding process. Below

describes each step in detail.

**Step 1:** We start with the pulse obtained from the previous iteration.

**Step 2:** Next, we measure two control qualities $F^{k,\pm x}$. For HQCA, the pulse is obtained by inserting a $\pm\pi/2$ rotation around the $x$-axis at the $k^{\text{th}}$ segment of the $x$-phase of the previous pulse (see Appendix B). For the $y$-phase pulse, a $\pm\pi/2$ rotation about the $y$-axis would be used. For the FD method, the the pulse is obtained by adding/subtracting a vector that is proportional to the $k^{\text{th}}$ basis vector from the $x$ or $y$-phase of the previous pulse. The index $k$ runs from 1 to the total number of pulse segments for the HQCA method, or from 1 to the size of the basis set $\mathbf{v}^k$ for the FD method.

**Step 3:** The $x$-phase gradient is given by $g_k \propto F^{k,+x} - F^{k,-x}$ (see Eq. (5.7) for HQCA or Eq. (5.8) for the FD method).

**Step 4:** By summing over all $k$, we obtain the full gradient for the current iteration in $x$-phase, $\mathbf{g} = \sum_k g_k \mathbf{v}^k$. For the HQCA method, $\mathbf{v}^k$ is a unit vector with the only non-zero element being 1 at the $k^{\text{th}}$ index, e.g. $\{0,0,1,0,...,0\}$ for $k=3$. For the FD method, it is the $k^{\text{th}}$ basis vector from a chosen set; in this paper we use linear and Slepian basis.

**Step 5:** We update the $x$-phase pulse from previous iteration by adding $c\mathbf{g}$. Here, $c$ is a scaling factor chosen to avoid over- or undershooting. The $y$-phase pulse is updated in a similar manner, after finding the $y$-phase gradient.

Figure 5.4 summarizes the closed-loop optimization of the $\text{ZI} \rightarrow \text{ZZ}$ pulse (gate 2). Similar to open-loop methods like GRAPE, the fidelity is seen to increase quickly in the first few iterations, but slows down and eventually saturates when the measured gradient becomes comparable to the shot noise. Although there is a convergence proof [9, 89] in case of noisy measurements, there are two problems in practice: (1) inaccuracy in measured gradients and (2) difficulty in verifying small improvements in $F$. Moreover, a long-term drift in measurements can prevent $F$ from reaching a convergence [9]. In practice, we found that there was no benefit in going beyond $\sim$15 iterations for the gates and protocols tested here, i.e. when the improvement in $F$ per iteration is smaller than the measurement noise.

Table 5.1 summarizes the final $F_{\text{XI}}$ and $F_{\text{ZZ}}$ obtained using three closed-loop optimal quantum control methods, (i) HQCA, (ii) FD with linear basis, and (iii) FD with Slepian basis. In addition, the results of open-loop control are presented. Here, the open-loop pulses were designed under three different conditions: (i) $A$=72 MHz, $B$=0 MHz, $\mathcal{T}$=1, (ii) $A$=66 MHz, $B$=26 MHz, $\mathcal{T}$=1, and (iii) $A$=66 MHz, $B$=26 MHz, $\mathcal{T}=\mathcal{T}_{meas}$. $\mathcal{T}$ denotes the transfer function, and $\mathcal{T}$=1 means that the pulses were designed under an ideal, flat transfer function. $\mathcal{T}=\mathcal{T}_{meas}$ indicates that the pulse design accounted for the experimentally measured transfer function (see Appendix E). In all the three conditions, a $\sim$10 MHz FWHM Larmor frequency distribution with the Lorentzian shape was considered. When designing the open-loop pulses, the gradients were calculated numerically using the FD

method and two basis sets, the linear and Slepian basis, were used for comparison with their closed-loop counterparts. All the designed open-loop pulses have a simulated control quality higher than 1.020 for gate 1 and higher than 0.990 for gate 2 under their specific design conditions. As mentioned earlier section, the control quality of gate 1 is greater than 1 because it is more efficient in exciting the transitions than the square $\pi/2$ pulse used in the reference measurement (see Fig. 5.2(b)).

First of all, we remark again that direct comparison of $F_{\mathrm{XI}}$ and $F_{\mathrm{ZZ}}$ is not proper as $F_{\mathrm{XI}}$ is not strictly a fidelity. For open-loop quantum optimal control, we observe higher $F$ when more accurate Hamiltonian parameters and realistic $\mathcal{T}$ are taken into consideration. However, closed-loop quantum optimal control methods still outperform the best open-loop results. Both closed-loop methods, HQCA and FD, produced similar control qualities under the experimental conditions tested here. However, simulations show that under different conditions, one method can perform better. This is described in the section below.

## 5.4 Simulations

Simulations were performed to further elucidate the roles of measurement noise and the spectrometer transfer function in limiting the final closed-loop control quality. In these simulations, the closed-loop optimization is performed in the same way as before, but with the experimental system response simulated by computer. The simulations were ended when the overall improvement after five successive iterations is smaller than 0.01. As shown in Table 5.2, the simulation results indicate that HQCA is more robust to the measurement noise than FD methods. We find that this increased robustness for HQCA is due to its larger gradients compared to the FD methods.

The effect of the transfer function on closed-loop optimization was also tested in simulations. When the bandwidth of the transfer function is about twice the spectral width, both HQCA and FD methods give similar results. However, when the bandwidth of the transfer function becomes similar to the width of the spectrum, FD methods become superior to HQCA. This is because the derivation of Eq. (5.7) assumes $\mathcal{T}=1$, and non-ideal $\mathcal{T}$ will cause imperfections in $R_\alpha(\pm\pi/2)$ and measured gradients. In real experiments, if the transfer function is unknown or has limited accuracy, the distorted gradients cannot be corrected properly and will slow down the search. However, the gradient measurements should not be affected by non-ideal $\mathcal{T}$ in FD methods as these effects are accounted for automatically.

Experimentally observed control qualities for gate 2 ($F_{\mathrm{ZZ}}$; see Eq. (5.12) and Table 5.1)

| | Closed-loop control | | | Open-loop control | | |
|---|---|---|---|---|---|---|
| | HQCA | FD (linear) | FD (Slepian) | $A$=72 MHz,$B$=0 MHz, $\mathcal{T}$=1 | $A$=66 MHz,$B$=26 MHz, $\mathcal{T}$=1 | $A$=66 MHz,$B$=26 MHz, $\mathcal{T}$=$\mathcal{T}_{meas}$ |
| $F_{\mathrm{XI}}$ | 0.968(39) | 0.993(46) | 1.010(40) | · | 0.946(40)$^\dagger$0.951(41)$^*$ | 0.955(37)$^\dagger$0.990(51)$^*$ |
| $F_{\mathrm{ZZ}}$ | 0.914(36) | 0.918(43) | 0.932(37) | 0.807(37)$^\dagger$0.799(37)$^*$ | 0.891(40)$^\dagger$0.883(45)$^*$ | 0.889(39)$^\dagger$0.902(43)$^*$ |

Table 5.1: Experimental control qualities for gate operations 1 and 2. For closed-loop control, results are given for HQCA, FD with linear basis, and FD with Slepian basis. For open-loop control, the Hamiltonian parameters were varied as well as whether or not the spectrometer transfer function is accounted for in pulse design. The numbers reported here are averages of 50 measurements, and given in the parentheses are standard deviations (e.g. 0.968(39)=0.968±0.039). $^\dagger$ The open-loop control pulses were designed using the full-bandwidth basis set. $^*$ The open-loop control pulses were designed using the limited-bandwidth basis set, i.e. the Slepian basis, with a control bandwidth of 120 MHz. It should be noted that direct comparison of $F_{\mathrm{XI}}$ and $F_{\mathrm{ZZ}}$ is not proper as $F_{\mathrm{XI}}$ is not strictly a fidelity (see the main text).

are considerably lower than values obtained in the simulations. Transverse and longitudinal relaxations ($T_2{\sim}4$ $\mu$s and $T_1{\sim}28$ $\mu$s) only give error of $\sim$2%, which does not fully explain the discrepancy. This could be due to several reasons.For closed-loop methods, one reason is that long-term drifts in the spectrometer components during experiment (single iteration takes $\sim$8-12 hours) may introduce error. This limited the total number of iterations performed in experiment, which was far fewer compared to the simulations. The neglect of small couplings to nearby proton spins, i.e. the use of a simplified 2-spin Hamiltonian, can partly explain the imperfect control obtained with both open- and closed-loop methods. Another possibility is that some components in the spectrometer transmission arm may exhibit small power non-linearities, so that $\mathcal{T}$ depends not only on frequency (as we assume) but also on microwave power.

## 5.5 Discussion

Two gradient-based closed-loop quantum control methods are experimentally demonstrated in a solid-state two-qubit system and compared with gradient-based open-loop control methods. The implemented closed-loop control methods outperform the open-loop methods when the information of the Hamiltonian and hardware transfer function lacks accuracy in our quantum system. The open-loop control can be further improved by taking into consideration of the uncertainties of the transfer function and the Hamiltonian (e.g. distributions of $A$, $B$, and small couplings with the environment) which will increase the classical resources needed for the open-loop pulse design exponentially.

| Noise | HQCA | FD (linear) | FD (Slepian) |
|---|---|---|---|
| ∼0.03 | 0.958(02) | 0.967(01) | 0.973(02) |
| ∼0.07 | 0.958(02) | 0.968(04) | 0.973(03) |
| ∼0.14 | 0.957(03) | 0.947(26) | 0.960(30) |
| ∼0.20 | 0.956(09) | 0.926(48) | 0.905(29) |

| FWHM | HQCA | FD (linear) | FD (Slepian) |
|---|---|---|---|
| ∼130MHz | 0.958 | 0.970 | 0.975 |
| ∼70MHz | 0.936 | 0.974 | 0.964 |

Table 5.2: Simulation results showing the effects of noise level and transfer function bandwidth on the control fidelities $F_{\mathrm{ZZ}}$ for gate 2. Noise: Zero-mean Gaussian random noise with a standard deviation ($\sigma$) of 0.03, 0.07, 0.14, and 0.20 was added to the ideal gradient measurements, where the reference measurements ($\overline{S}_L$ and $\overline{S}_R$) are normalized to 1. The averages and standard deviations of ten trials in each condition are given. Transfer function: In each case, the entire control pulse sequence was distorted according to a realistic transfer function with full width at half maximum (FWHM) of 130 and 70 MHz. In the simulation with different noise levels, the transfer function with 130 MHz FWHM was considered. Simulated pulse finding was stopped when the overall improvement over five successive iterations was smaller than 1%. $T_2$ was not included in this simulation.

Together with simulations, we find that for the closed-loop optimzation, HQCA works better than FD methods when shot noise in measurements is large enough to be the dominant error limiting the gradient search. When $\mathcal{T}$ is narrow and/or the control bandwidth is limited (often by hardware), FD methods can perform better than HQCA. With the bandwidth-limited Slepian basis set, the gradient finding procedure of the FD method can be made less time-consuming and the pulses generated may be friendlier to implement in experiment. Thus, starting with a viable open-loop quantum optimal control (e.g. GRAPE) pulse and running subsequent iterations of an appropriate closed-loop control protocol may be a good strategy to reach high control quality under realistic experimental conditions [76]. It should be mentioned that in the experimental setting of this work, the signal-to-noise ratio (SNR) is one of the major factors limiting the final control quality of the closed-loop methods (SNR~17 with 16,000 averaging). This also causes the closed-loop optimization processes to be more time-consuming than the open-loop counterparts. However, as mentioned earlier, our open-loop pulse design did not consider all of the factors to expedite the process. Moreover, the time consumption of open-loop control optimization process will increase exponentially with the system size, which is not the case with the closed-loop control process. Therefore, the time consumption is not a critical drawback of the closed-loop control. In the future, it may be of interest to combine the optimal random orientation method [89, 90] with the closed-loop quantum control methods for better efficiency of convergence rate.

# Chapter 6

# Finding Unitary gates on a quantum processor

## 6.1 Introduction

Although we see from the previous chapters that it is feasible to learn a pulse that takes a particular initial state to a desired final state *i.e.* an state-to-state pulse, a general quantum computing and information tasks needs an gate which is state independent. The inspiration for this work is finding out whether we can optimize a gate on a quantum computer itself. There is many advantages if one is able to do that, especially it will help when there is partial knowledge of Hamiltonian available or the experimental imperfections are not exactly known. Experimentally optimizing the gates would help us to perform universal quantum computing as well as the method can be used efficiently when the number of qubits increases.

The reason a gate optimization seems elusive is the fitness function associated with it, $f = tr(U_t \tilde{U})$, and gradient, $g$ associated with gate optimization is not directly measurable as in previous case [44]. So we ask the question given we can optimize only state-to-state pulses on a quantum computer how does one optimize general gates.

A naive way would be optimizing an state-to-state pulse that take all the basis to the states to the corresponding output states. This implies we would be optimizing for $4^n - 1$ states for a $n$ qubit system. Although possible for small number of qubits the problem the practicality will diminish with rather humble number of qubits. Although if we take advantage of the Pauli matrix algebra we can reduce the problem size to optimizing for $2n$

chosen basis states only. In the following we discuss how the basis optimization results in the gate optimization and how we take reduce the problem size.

## 6.2   Theory

Consider a one qubit system, and a desired unitary $U_t$ one wants to find. The action of this unitary on all the basis states is represented as:

$$X \xrightarrow{U_t} U_t X U_t^\dagger \equiv \rho_X$$
$$Y \xrightarrow{U_t} U_t Y U_t^\dagger \equiv \rho_Y$$
$$Z \xrightarrow{U_t} U_t Z U_t^\dagger \equiv \rho_Z \qquad (6.1)$$

As we only have access to state-to-state pulses optimization, if we can optimize for an unitary ($\tilde{U}$) that evolves all the basis states to the desired output state ($\rho_{X,Y,Z}$) simultaneously, we know there is only an unique operation $i.e.$ $U_t$ that does this transformation. Hence, $\tilde{U} = U_t$. The three fitness function we would be optimizing are,

$$tr(\tilde{U} X \tilde{U}^\dagger \rho_X)$$
$$tr(\tilde{U} Y \tilde{U}^\dagger \rho_Y)$$
$$tr(\tilde{U} Z \tilde{U}^\dagger \rho_Z) \qquad (6.2)$$

However we know from the Pauli matrix algebra that $XY = iZ$ hence the last equation in Eqs. 6.1 can be written as

$$\begin{aligned} U_t Z U_t^\dagger &= U_t(-iXY)U_t^\dagger \\ &= -iU_t X U_t U_t^\dagger Y U_t^\dagger \\ &= -i\rho_X \rho_Y \equiv \rho_Z \qquad (6.3) \end{aligned}$$

also, $\rho_Z \equiv i\rho_Y \rho_X$. This means the evolution of $Z$ state is fixed given the evolution of $X, Y$ states, this is a powerful result and implies we don't have to optimize for $Z$ state. In other words if $tr(\tilde{U} X \tilde{U}^\dagger \rho_X) = 1$ and $tr(\tilde{U} Y \tilde{U}^\dagger \rho_Y) = 1$ this implies $tr(\tilde{U} Z \tilde{U}^\dagger \rho_Z) = 1$, before proving this claim let us first prove another result,

*Claim* — If $tr(\tilde{U} X \tilde{U}^\dagger \rho_X) = 1$ it implies $\tilde{U} X \tilde{U}^\dagger = \rho_X$

*Proof* — Let us write $\rho_X$ as $\vec{a}_X \cdot \vec{\sigma}$. Similarly, we can write $\tilde{U} X \tilde{U}^\dagger$ as $\vec{\tilde{a}}_X \cdot \vec{\sigma}$ where, where $\vec{a}_X$ and $\vec{\tilde{a}}_X$ are unit vectors with components $a_{1X}, a_{2X}, a_{3X}$ etc.  . This implies $tr(\tilde{U} X \tilde{U}^\dagger \rho_X) = \vec{a}_X \cdot \vec{\tilde{a}}_X$. The dot product of two unit vectors is one only when they

66

coincide. Hence, $tr(\tilde{U}X\tilde{U}^\dagger\rho_X) = 1$ implies $\tilde{U}X\tilde{U}^\dagger = \rho_X$.

Now, coming back to our original claim that $tr(\tilde{U}X\tilde{U}^\dagger\rho_X) = 1$ and $tr(\tilde{U}Y\tilde{U}^\dagger\rho_Y) = 1$ implies $tr(\tilde{U}Z\tilde{U}^\dagger\rho_Z) = 1$

$$
\begin{aligned}
tr(\tilde{U}Z\tilde{U}^\dagger\rho_Z) &= tr(\tilde{U}(-iXY)\tilde{U}^\dagger(i\rho_Y\rho_X)) \\
&= tr(\tilde{U}XY\tilde{U}^\dagger\rho_Y\rho_X) \\
&= tr(\tilde{U}X\tilde{U}\tilde{U}^\dagger Y\tilde{U}^\dagger\rho_Y\rho_X) \\
&= tr(\rho_X\tilde{U}X\tilde{U}\tilde{U}^\dagger Y\tilde{U}^\dagger\rho_Y) \\
&= 1
\end{aligned}
\tag{6.4}
$$

where in the second last line we have used the previously provided proof and the fact that $X^2 = Y^2 = Z^2 = \mathbb{I}$.

We now look at a two qubit case to give an idea of how we can extend this idea of optimizing for less number of basis states. The basis states are given by

|     | $X\mathbb{I}$ | $Y\mathbb{I}$ | $Z\mathbb{I}$ |
|-----|-----|-----|-----|
| $\mathbb{I}X$ | $XX$ | $YX$ | $ZX$ |
| $\mathbb{I}Y$ | $XY$ | $YY$ | $ZY$ |
| $\mathbb{I}Z$ | $XZ$ | $YZ$ | $ZZ$ |

It can be easily shown than any of the blue colored basis state can be written as a product or is proportional to the product of two or all of red colored operators ($X\mathbb{I}, Y\mathbb{I}, \mathbb{I}X, \mathbb{I}Y$). This, along with the results obtained in equations 6.1-6.4, prove that we only need to optimize state-to-state pulses for 4 input states. Now, we can easily see the generalization is that $2n$ state need to be optimized to find a unitary pulses. If we represent

$$
A_j = \mathbb{I}^{\otimes j-1} \otimes A \otimes \mathbb{I}^{\otimes N-(j+1)}
\tag{6.5}
$$

then we need to optimize for $j \in 1:n$ and $A \in X, Y$. Note that $X, Y$ is not a unique choice, any two of the three non-commuting Pauli matrices will do. This significantly reduces the number of optimizations we have to do and the number varies polynomially now with the number of qubits.

Although this is well and good, in real world it is very hard to reach the max value of fitness function, for example, $tr(\tilde{U}X\tilde{U}^\dagger\rho_X) = 1$. Going back to our one qubit example, it becomes much more important to ask the question of what can we say about $tr(\tilde{U}Z\tilde{U}^\dagger\rho_Z)$

in such a case then. We again represent the states as dot product of a unit vector with Pauli vector,

$$
\begin{aligned}
\rho_X &= \vec{a}_X \cdot \vec{\sigma} \\
\tilde{U}X\tilde{U}^\dagger &= \vec{\tilde{a}}_X \cdot \vec{\sigma} \\
\rho_Y &= \vec{a}_Y \cdot \vec{\sigma} \\
\tilde{U}Y\tilde{U}^\dagger &= \vec{\tilde{a}}_Y \cdot \vec{\sigma}
\end{aligned}
$$

Then as proved earlier the fitness functions

$$
\begin{aligned}
tr(\tilde{U}X\tilde{U}^\dagger \rho_X) &= \vec{a}_X \cdot \vec{\tilde{a}}_X = cos(\theta_X) \\
tr(\tilde{U}Y\tilde{U}^\dagger \rho_Y) &= \vec{a}_Y \cdot \vec{\tilde{a}}_Y = cos(\theta_Y)
\end{aligned}
\tag{6.6}
$$

Using these we try to find what the fitness function for the $Z$ state look like

$$
\begin{aligned}
tr(\tilde{U}Z\tilde{U}^\dagger \rho_Z) &= tr(\tilde{U}(-iXY)\tilde{U}^\dagger(i\rho_Y\rho_X)) \\
&= tr(\tilde{U}XY\tilde{U}^\dagger\rho_Y\rho_X) \\
&= tr(\tilde{U}X\tilde{U}^\dagger\tilde{U}Y\tilde{U}^\dagger\rho_Y\rho_X) \\
&= tr(\rho_X\tilde{U}X\tilde{U}^\dagger\tilde{U}Y\tilde{U}^\dagger\rho_Y) \\
&= tr\left((\vec{a}_X \cdot \sigma)(\vec{\tilde{a}}_X \cdot \sigma)(\vec{a}_Y \cdot \sigma)(\vec{\tilde{a}}_Y \cdot \sigma)\right) \\
&= (\vec{a}_X \cdot \vec{\tilde{a}}_X)(\vec{a}_Y \cdot \vec{\tilde{a}}_Y) - (\vec{a}_X \times \vec{\tilde{a}}_X) \cdot (\vec{a}_Y \times \vec{\tilde{a}}_Y) \\
&= cos(\theta_X)cos(\theta_Y) - sin(\theta_X)sin(\theta_Y)(\vec{a}_X^\perp \cdot \vec{a}_Y^\perp)
\end{aligned}
\tag{6.7}
$$

where, $\vec{a}_X^\perp$ is the unit vector perpendicular to $\vec{a}_X$ and $\vec{\tilde{a}}_X$ and $\vec{a}_Y^\perp$ is the unit vector perpendicular to $\vec{a}_Y$ and $\vec{\tilde{a}}_Y$. This implies we can put a limit to the value of the third fitness function,

$$
cos(\theta_X)cos(\theta_Y) - sin(\theta_X)sin(\theta_Y) \le tr(\tilde{U}Z\tilde{U}^\dagger\rho_Z) \le cos(\theta_X)cos(\theta_Y) + sin(\theta_X)sin(\theta_Y) \tag{6.8}
$$

Hence, we can faithfully say if the calculated fitness function is close to 1 the rest of the fitness function will be in acceptable range. We see a visual representation of this bound in Fig. 6.1.

When we go to higher number of qubits, $\vec{a}_X$ and other unit vectors represented are now unit vectors in a higher dimensional state. The bound still follows the same proof for the states which are related to 2 of the optimized states, by which we mean: we optimize for

$XI, YI, IX, IY$ and fitness function for any state that can be obtained from two of these four states follows the same proof( for example, $ZI = -iXI \cdot YI$). The things become different for the states which are obtained from three of these four states. The proof goes as follows:

$$
\begin{aligned}
tr(\tilde{U}ZX\tilde{U}^\dagger \rho_{ZX}) &= tr(\tilde{U}(-iXI \cdot YI \cdot IX)\tilde{U}^\dagger (i\rho_{YI}\rho_{XI}\rho_{IX})) \\
&= tr(\tilde{U}XI \cdot YI \cdot IX\tilde{U}^\dagger \rho_{YI}\rho_{XI}\rho_{IX})) \\
&= tr(\tilde{U}XI\tilde{U}^\dagger \tilde{U}YI\tilde{U}^\dagger \tilde{U}IX\tilde{U}^\dagger \rho_{YI}\rho_{XI}\rho_{IX}) \\
&= tr\left((\vec{a}_{XI} \cdot \sigma)(\vec{\tilde{a}}_{XI} \cdot \sigma)(\vec{a}_{YI} \cdot \sigma)(\vec{\tilde{a}}_{YI} \cdot \sigma)(\vec{a}_{IX} \cdot \sigma)(\vec{\tilde{a}}_{IX} \cdot \sigma)\right) \\
&= cos(\theta_{XI})cos(\theta_{YI})cos(\theta_{IX}) - sin(\theta_{XI})sin(\theta_{YI})sin(\theta_{IX})(\vec{a}_{XI}^\perp \cdot \vec{a}_{YI}^\perp \cdot \vec{a}_{IX}^\perp)
\end{aligned}
$$

Thus the bound now is

$$
\begin{aligned}
cos(\theta_{XI})cos(\theta_{YI})cos(\theta_{IX}) - sin(\theta_{XI})sin(\theta_{YI})sin(\theta_{IX}) &\leq tr(\tilde{U}ZX\tilde{U}^\dagger \rho_{ZX}) \\
&\leq cos(\theta_{XI})cos(\theta_{YI})cos(\theta_{IX}) + sin(\theta_{XI})sin(\theta_{YI})sin(\theta_{IX})
\end{aligned} \tag{6.9}
$$

Similarly the bound can be obtained for any state that is not optimized.

## 6.3   Experimental proposals and simulation results

### 6.3.1   Measurement of fitness function

As described in earlier chapters measuring $f$ is straightforward. For an $n$-qubit system, the total number of elements in the Pauli basis is $4^n - 1$ (without the identity term). If the target state $\rho_f$ has some decomposition, say, $\rho_f = \sum_{\gamma=1}^{\mathcal{G}} x_\gamma P_\gamma$ with respect to the Pauli basis, then the fitness function is

$$
f = tr\left(\tilde{\rho}\rho_f\right) = \sum_{\gamma=1}^{\mathcal{G}} x_\gamma \, tr\left(\tilde{\rho}P_\gamma\right). \tag{6.10}
$$

Here, $1 \leq \mathcal{G} \leq 4^n$ denotes the number of nonzero components, $P_\gamma$ is the $\gamma$-th element of the Pauli basis, and $x_\gamma$ is its corresponding coefficient.
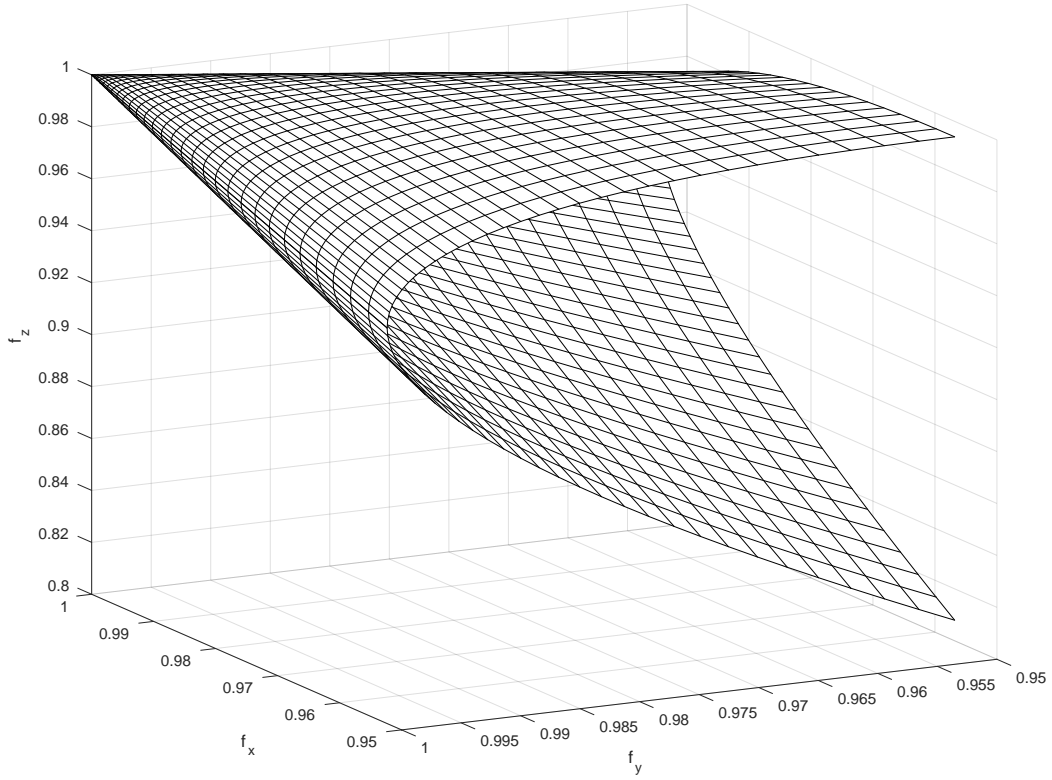
Figure 6.1: Plot of the bound on the fitness function $f_z = tr(\tilde{U}Z\tilde{U}^\dagger \rho_Z)$ given the values of the fitness functions $f_x = tr(\tilde{U}X\tilde{U}^\dagger \rho_X)$ and $f_y = tr(\tilde{U}Y\tilde{U}^\dagger \rho_Y)$

### 6.3.2 Slepian Basis

We utilize the finite difference(FD) method of calculating gradients, mainly, since we can utilize a Slepian basis which have much less number of control parameter. A Slepian basis is composed of Slepian sequances which are also called discrete prolate spheroidal sequences [84]. Slepian sequences with a sequence length $N$ and half bandwidth $W \in (0, 0.5]$ are defined to be the real solutions to the eigenvalue problem

$$\sum_{m=0}^{N-1} \frac{\sin 2\pi W(l-m)}{\pi(l-m)} v_k(m; N, W)$$
$$= \lambda_k(N, W) v_k(l; N, W). \tag{6.11}$$

Here, $k, l \in \{0, 1, ..., N-1\}$, and $v_k(l; N, W)$ is the $l^{\text{th}}$ element of the $k^{\text{th}}$ order Slepian sequence. The Slepian sequences are spectrally concentrated in the frequency range $[-W/\Delta t, W/\Delta t]$, especially the first $2NW$ ones. Ref. [86] used the first $2NW$ Slepian sequences to approximate the space of bandwidth limited sequences of length $N$. Slepian sequences also have the property of beginning and ending smoothly to zero, which is favorable for experimental setup, since the amplitude of the RF pulses can only smoothly increase in real world. First four sequences for a chosen value of $N$ and $NW$ is plotted in Fig 6.2

### 6.3.3 Improvement in the technique when using NMR

Till now the implementation is general and can be easily adapted to any quantum processor, however we can have even more improvement to this general method when implementing such a procedure in NMR. Since the initial state of a homonuclear NMR system is written as

$$\rho_{in} = \sum_j Z_j, \tag{6.12}$$

we can instead of optimizing lets say for 2 qubits $Z_1$ and $Z_2$ we can perform one optimization for $Z_1 + Z_2$, and similarly instead of $X_1$ and $X_2$ we can optimize $X_1 + X_2$. This decreases the number of state-to-state pulsed to be optimized to 2 irrespective on number of qubits, which greatly reduces the amount of experiments needed and time required for optimization. The single qubit gates do not change the coherence of the state, hence this technique will work on any molecule. However, for two qubit gates the coupling between the spin should be resolvable and in practice we choose to apply the two qubit only between such spins, hence, this technique is valid for any molecule.
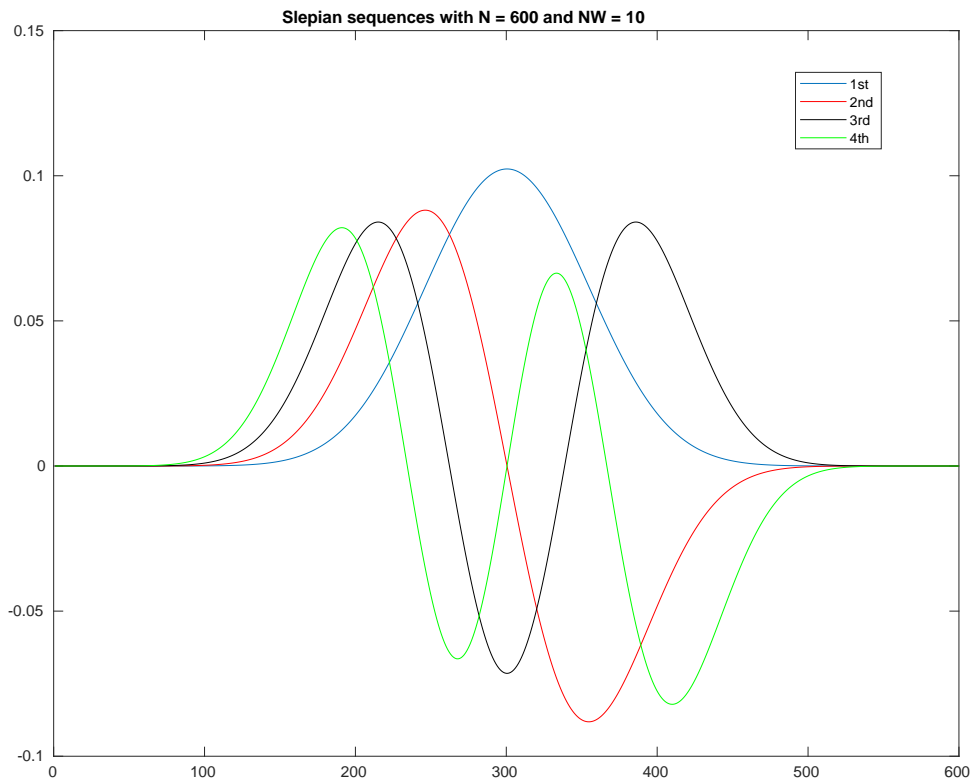
Figure 6.2: Plot of first four slepian sequences for $N = 600$ and $NW = 10$, notice the smooth beginning of the sequences.

## 6.3.4 Simulation

We used the aforementioned methods to find a unitary on a 4-qubit quantum processor. We again used the $^{13}C$ of crotonic acids. The simulation were performed with the Hamiltonian parameters as shown in Fig. 6.3



| | C1 | C2 | C3 | C4 |
|---|---|---|---|---|
| C1 | -2989 | | | |
| C2 | 41.62 | -25459 | | |
| C3 | 1.46 | 69.66 | -21592 | |
| C4 | 7.02 | 1.18 | 72.16 | -29342 |
| T1 | 1.02 | 0.92 | 0.87 | 0.94 |
| T2 | 5.7 | 5.3 | 5.6 | 10.2 |
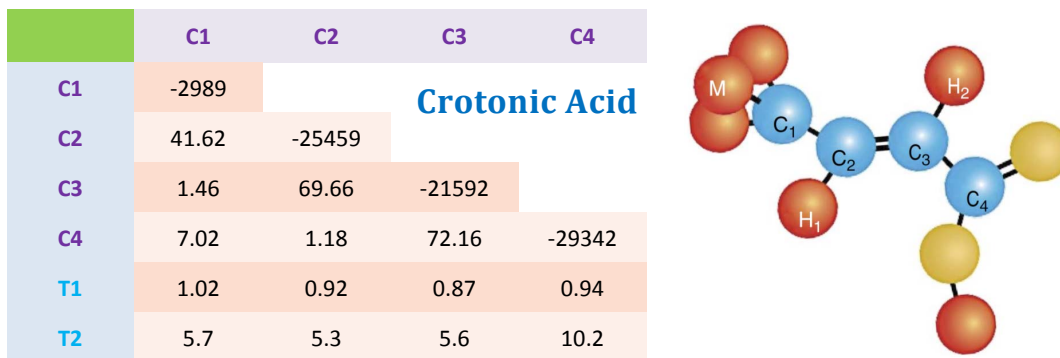
Figure 6.3: $^{13}$C-labeled trans-crotonic acid. The table shows the resonance frequencies (diagonal elements, in hertz), the J-coupling constants (off-diagonal elements, in hertz), and the relaxation times $T_1$ and $T_2$ (in seconds).

We first show that a single qubit rotation gate on a 4-qubit processor can be found, with reasonable experimental expectations, see Fig 6.4 and the properties of the optimized pulse is shown in Fig. 6.5. We also show we can find a Cnot gate using the same method the results are show in Fig. 6.6 along with the optimized pulse obtained in Fig. 6.7. The control Hamiltonian is written as,

$$H_c(t) = A(t)\cos(\phi(t)) \sum_{j=1:4} \sigma_x^j + A(t)\sin(\phi(t)) \sum_{j=1:4} \sigma_y^j. \tag{6.13}$$

$A$ is the amplitude of the pulse, and $\phi$ is the phase. The guess pulse was obtained as a linear combination of 19 slepian sequences,

$$u_x(t) = \sum_{j=1:19} k_x^j v_j(t) \quad \& \quad u_y(t) = \sum_{j=1:19} k_y^j v_j(t), \tag{6.14}$$

where, $k$ is the random number sampled from a uniform distribution between 0 and 1, and

$v$ is the slepian sequence. These controls were converted into amplitude and phase by

$$A(t) = \sqrt{u_x(t)^2 + u_y(t)^2} \quad \& \quad \phi(t) = atan(u_y(t)/u_x(t)) \tag{6.15}$$
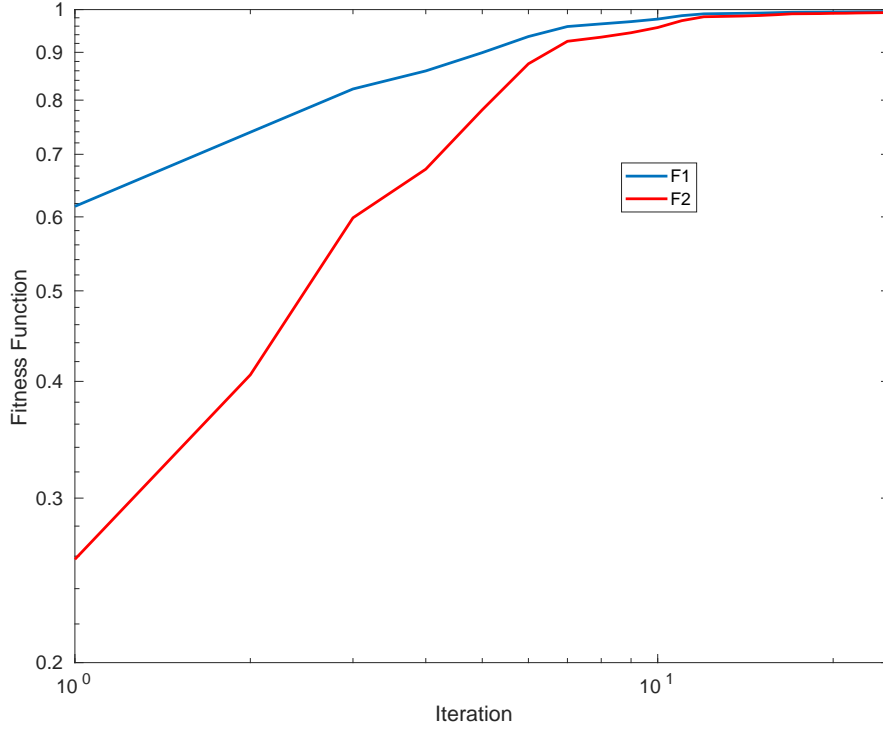


Figure 6.4: (log-log scale) Optimization to find a single qubit unitary gate $(R^y_{90})$ on C1 of crotonic acid, F1 is the sum of the state to state fitness functions, $F1 = \sum_{j,A}(tr(\tilde{U}A_j\tilde{U}^\dagger\rho_{Aj}))$, where $A_j$ is from eq. (6.5) and $\rho_{Aj}$ is $U_t A_j U_t^\dagger$, and $j \in 1:4$, $A \in (X, Z)$. $F2$ is the unitary fitness function which is our goal and is given by $F2 = tr(U_t^\dagger\tilde{U})$
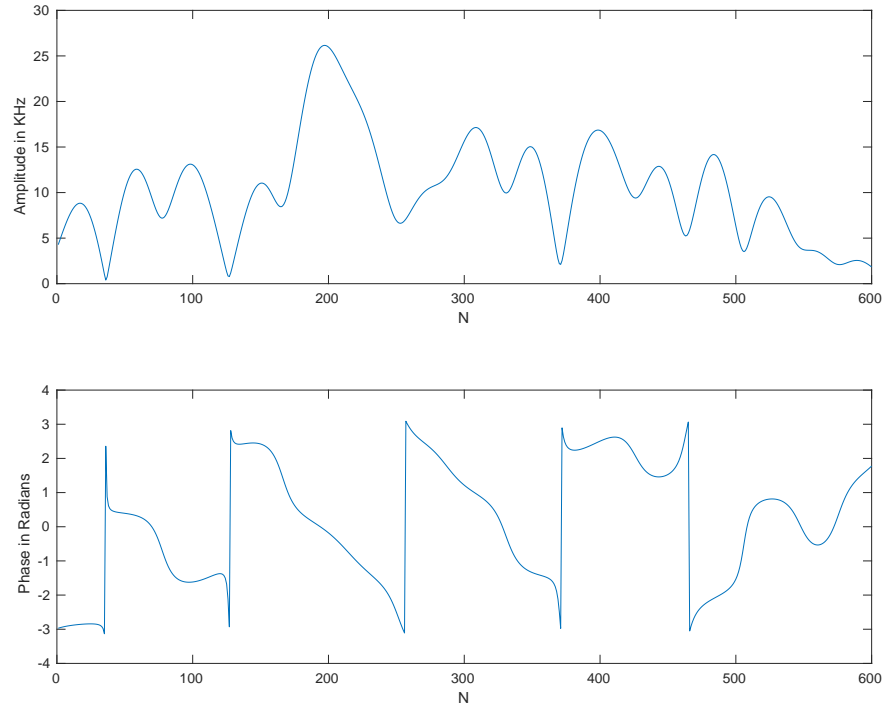
Figure 6.5: Pulse amplitude (top) and phase (bottom) obtained from the optimization of single qubit unitary gate $(R_{90}^y)$ on C1 of crotonic acid. The pulse is divided into 600 time steps, each of length $1\mu s$
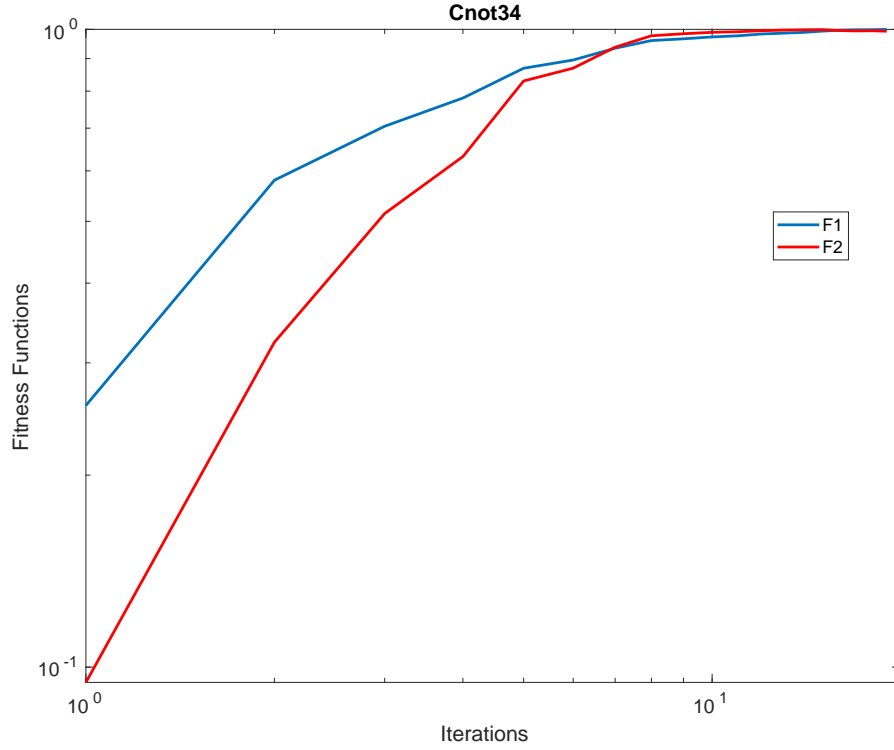
Figure 6.6: (log-log scale) Optimization to find CNOT gate controlled on C3 and target on C4 of the crotonic acid, F1 is the sum of the state to state fitness functions, $F1 = \sum_{j,A}(tr(\tilde{U}A_j\tilde{U}^\dagger\rho_{Aj}))$, where $A_j$ is from eq. (6.5) and $\rho_{Aj}$ is $U_tA_jU_t^\dagger$, and $j \in 1:4$, $A \in (X, Z)$. $F2$ is the unitary fitness function which is our goal and is given by $F2 = tr(U_t^\dagger\tilde{U})$
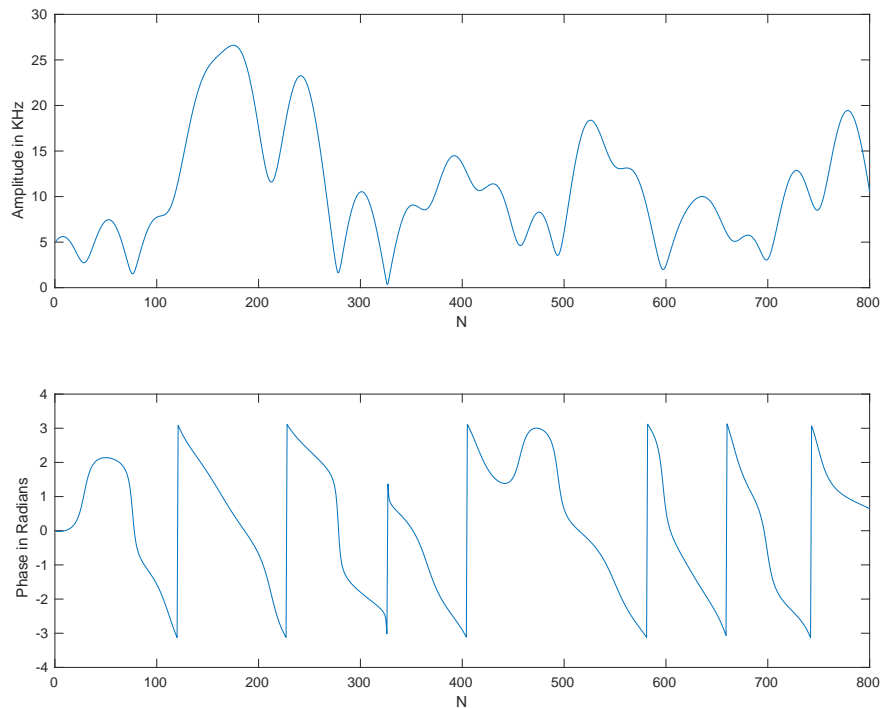
Figure 6.7: Pulse amplitude (top) and phase (bottom) obtained from the optimization of CNOT gate controlled on C3 and target on C4 of the crotonic acid. The pulse is divided into 800 time steps, each of length $10\mu$s

## 6.4 Experiments

We ran an experiment to search for gate that performs $\pi/2$ rotation on $C_3$ around $x$-axis. The number of slepian sequences used in eq. 6.14 were 19, and the time was discretized into 600 steps with each step of $1us$. We first prepare the two initial states for which the optimization was made, namely $\sum Z_i$ and $\sum X_i$, where $i$ runs from 1 to 4. Former is the thermal state of the system and is naturally available, later was prepared using state-to-state method and the results are shown in fig. 6.8
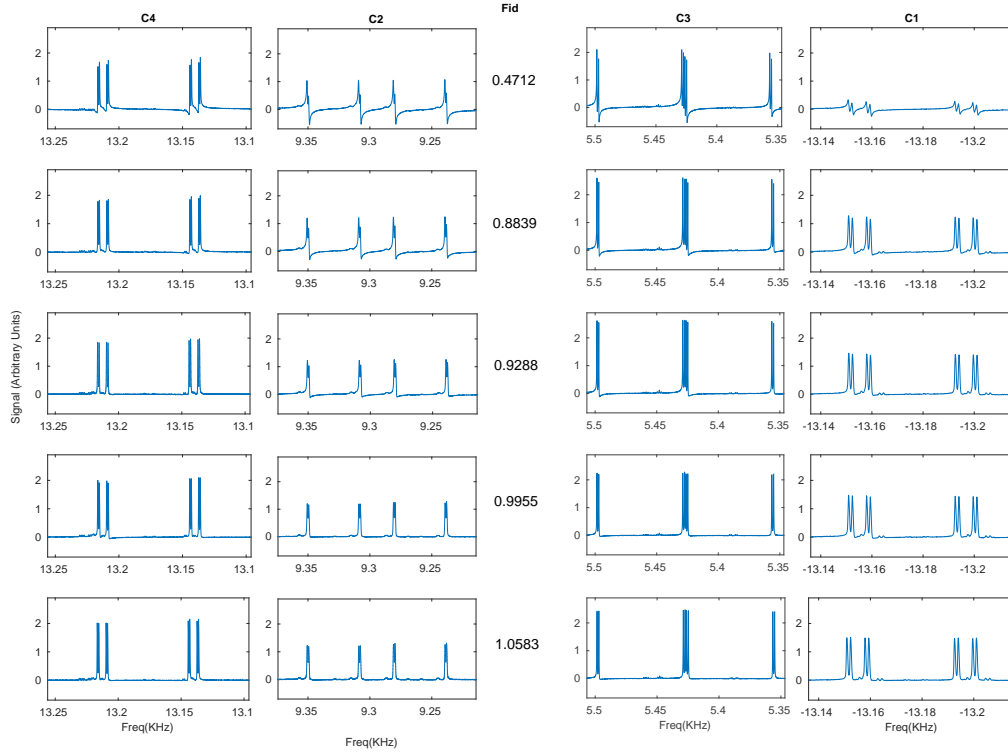
Figure 6.8: Driving system from thermal state to $\sum X_i$, the iteration of optimization runs from top to bottom and each row shows the spectra at the particular iteration. The fidelity is the fitness function and since it is normalized with respect to a hard pulse, it can go greater than 1. When the fitness function is greater than one it means the pulse is better than the hard pulse which is a short duration non-selective square pulse.

After preparing the state we perform our optimization to find the target gate : $\pi/2$ rotation on $C_3$ around $x$-axis. Such a gate takes $\sum_{i=1:4} Z_i$ to $Z_1 + Z_2 - Y_3 + Z_4$ and $\sum_{i=1:4} X_i$ to $\sum i = 1 : 4 X_i$ simultaneously. The optimization is shown in fig. 6.9 and 6.10.
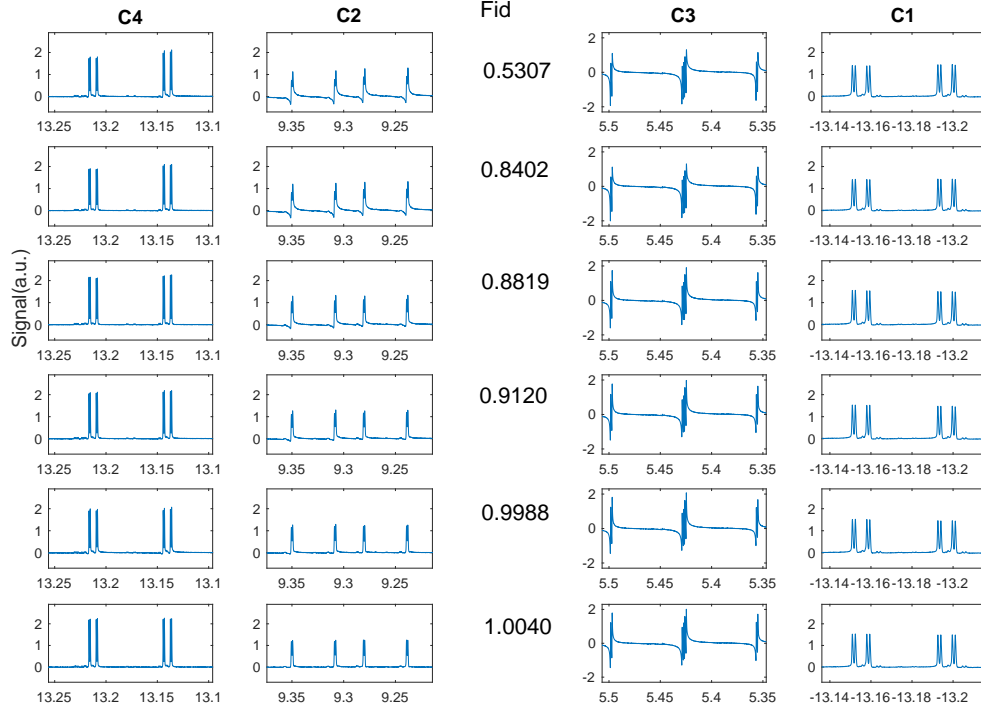
Figure 6.9: Driving system from $\sum_{i=1:4} Z_i$ to $Z_1+Z_2-Y_3+Z_4$ , the iteration of optimization runs from top to bottom and each row shows the spectra at the particular iteration. A $\pi/2$ rotation along $y$-axis was performed to obtain these spectra. The fidelity is the fitness function and since it is normalized with respect to a hard pulse, it can go greater than 1. When the fitness function is greater than one it means the pulse is better than the hard pulse which is a short duration non-selective square pulse.
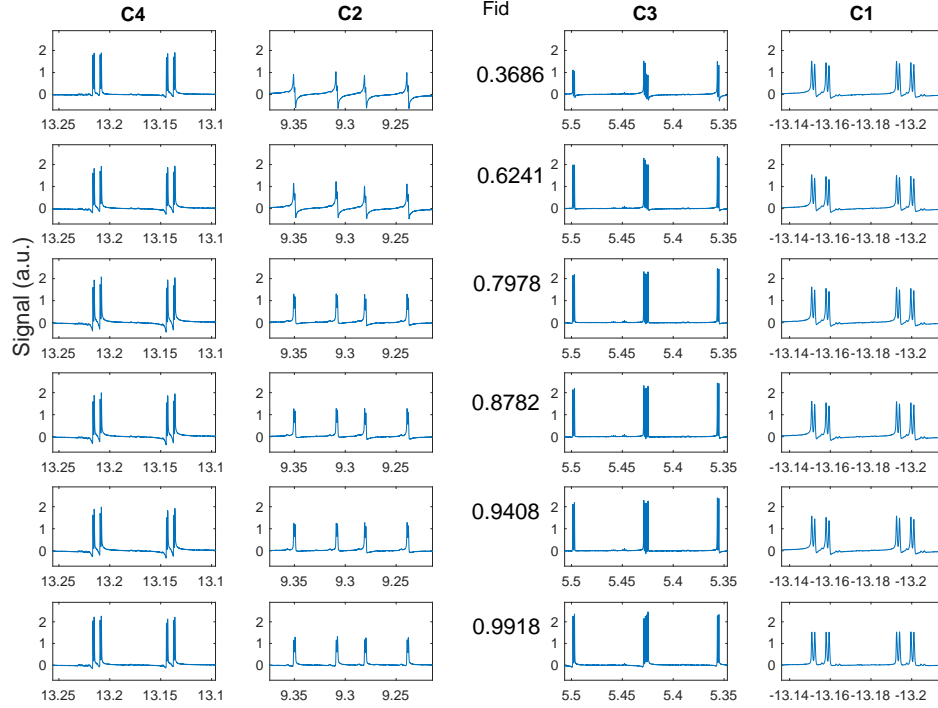
Figure 6.10: Driving system from $\sum_{i=1:4} X_i$ to $\sum i = 1 : 4X_i$, the iteration of optimization runs from top to bottom and each row shows the spectra at the particular iteration. The fidelity is the fitness function and since it is normalized with respect to a hard pulse, it can go greater than 1. When the fitness function is greater than one it means the pulse is better than the hard pulse which is a short duration non-selective square pulse.

The gate obtained in such a way is a $\pi/2$ rotation on $C_3$ around $x$-axis. To see whether this is true or not, we apply the final obtained gate(pulse) on the thermal state, $\sum_{i=1:4} Z_i$ and expect only $C_3$ to rotate. The result is shown in fig. 6.11
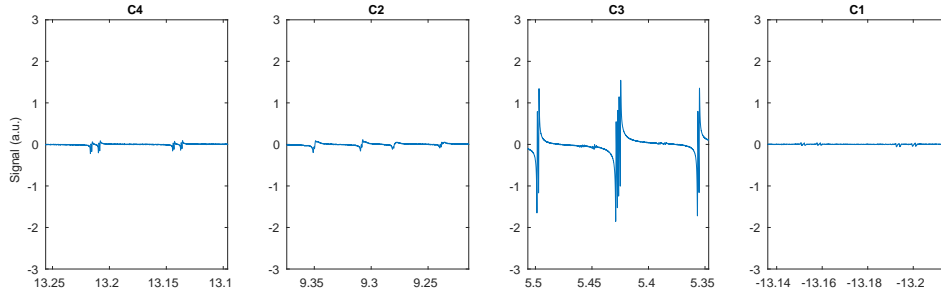
Figure 6.11: Final gate obtained from the optimization applied on the thermal state selectively rotates C$_3$ as desired.

## 6.5  Discussion and future work

The simulations suggest the feasibility of doing experiments and finding a gate on the quantum processor. Although for 4 qubits a classical computer can find a gate much more faster, the time required to find a gate from onward of 10 qubits becomes impractical due to exponential increase in the Hilbert space. There is a future plan of implementing the technique with a hybrid way of first optimizing a pulse classically, which essentially means we start from a good guess and then use the quantum optimization to produce the final gates. There are many advantages of doing so, starting from an good initial guess helps lower down the time for optimization which tough faster than classical still long. Second, even small imperfections matter when we are dealing with 12 qubits and its highly likely to be not having exact knowledge of the system this requirement is waived when the optimization is performed on the quantum system itself, since the procedure takes care of it. We hope this work will shortly lead to an experimental implementation.

# Chapter 7

# Conclusions

Nuclear magnetic resonance (NMR) has been a faithful test-bed to test many quantum information processing ideas for years. For moderately sized quantum processor NMR has proven to show high fidelity control. With time our desire to control more and more number of spins, we have reached a regime where classical methods for optimizing the control parameters have been proved to be impractical. With classical methods requiring full Hilbert space simulation, the amount of time needed to simulate 12 spins is unrealistic. Classical simulations for obtaining the control parameters suffer not only from unreasonable time, but also depend on our knowledge of the Hamiltonian, experimental imperfections. Moving forward, a solid state electron spin resonance (ESR) the knowledge of Hamiltonian and experimental imperfections play a huge role. The transfer function present in ESR system must be known upto a faithful extent to use classical methods of optimizing quantum control.

We know quantum systems are efficient for simulation of quantum evolution, while classical computers are far efficient in performing everyday calculation. This naturally poses a question : can we employ a hybrid classical-quantum optimization which is efficient for large number of qubits. This is the main question addressed in this thesis. On the way to answering this question, we performed NMR experiment showing the violation of Leggett-Garg inequalities (LGIs). LGIs put bounds on the correlation of system with itself at different point in time depending on the assumption that the evolution is classical. This bound is violated by quantum systems and the value of violation increases with dimensionality of the system. We show that we can achieve the highest experimentally achievable bound till date, to the best of our knowledge and perform rigorous error analysis to justify the claim. This experiment also serves as a justification of NMR having precise quantum control to test foundational question of quantum mechanics.

We move on to showing the optimal control of 12 qubits. We are used to performing classical methods of optimization to find pulses that perform certain quantum information processing task. These methods suffer from the requirement that they have to simulate the evolution of a quantum system, and we know that this task become exponentially harder. When in the regime of 12 qubits, it is almost impractical to utilize classical methods of control. We showed a hybrid classical-quantum control technique, utilizing best of both worlds to reach a 12-coherence state which is produced by entangling operation on a 12 qubit NMR processor. This experiment was not possible before with the classical methods of control and shows the importance of moving forward with hybrid schemes.

We show that we can utilize the hybrid control scheme on a 2 qubit solid state ESR system. Although much smaller than the NMR system, they still pose a challenge for optimal control. The Hamiltonian of the solid state molecule we used depend upon its relative orientation with the external magnetic field, the nuclei spins present. The transfer function also poses a challenge, hybrid scheme providing less strict condition on our knowledge of the system proves invaluable for performing such an experiment on an ESR system. We explicitly show an experimental comparison of all the schemes available with the best control to date provided by the hybrid scheme thus showing their superiority.

We have shown how to find optimal control pulses utilizing a hybrid scheme experimentally. These pulses are state-to-state pulses, *i.e.* the take a known initial state to a desired final state. Such a task is of high importance and many tasks in QIP can be performed in such a way, an example of such a task being algorithmic cooling. But, an universal quantum computation requires state independent gates. The hybrid scheme we utilized earlier to not trivially export to the gate finding. The reason being the fitness function and gradients for such a task are not in a form that can be measured efficiently on a quantum processor. We modify this hybrid scheme and show that these hybrid control scheme till now only possible for driving our system from an initial state to a desired final state can be utilized to optimize for state independent gates. We prove that such a task is efficient as in the number of optimization required grow polynomially with the number of qubits and is achievable by current experimental techniques.

In short term future, it would be great to implement these optimization for finding state independent gates on a 4 and 12 qubit processor. We have shown it is feasible to optimize single qubit gates and two qubit gates using the techniques presented in the thesis and current state of experimental techniques. A multi-control gate however using this method seems unlikely right now due the amount of control parameters needed, this is something to work towards in long term. Approximating the circuit using quantum circuit learning tasks is a exciting option and can provide some of the answers towards this problem [91].

# References

[1] Erwin Schrödinger. Die gegenwärtige situation in der quantenmechanik. die naturwissenschaften 23, s. 807–812. *S.*, 823:844–849, 1935.

[2] A. J. Leggett and A. Garg. *Phys. Rev. Lett.*, 54:857, 1985.

[3] Costantino Budroni and Clive Emary. Temporal quantum correlations and leggett-garg inequalities in multilevel systems. *Phys. Rev. Lett.*, 113:050401, Jul 2014.

[4] Navin Khaneja, Timo Reiss, Cindie Kehlet, Thomas Schulte-Herbrüggen, and Steffen J. Glaser. Optimal control of coupled spin dynamics: design of NMR pulse sequences by gradient ascent algorithms. *Journal of Magnetic Resonance*, 172(2):296, 2005.

[5] Jun Li, Xiaodong Yang, Xinhua Peng, and Chang-Pu Sun. Hybrid quantum-classical approach to quantum optimal control. *Phys. Rev. Lett.*, 118(15):150503, 2017.

[6] C Negrevergne, TS Mahesh, CA Ryan, M Ditty, F Cyr-Racine, W Power, N Boulant, T Havel, DG Cory, and R Laflamme. Benchmarking quantum control methods on a 12-qubit system. *Physical Review Letters*, 96(17):170501, 2006.

[7] Thomas Monz, Philipp Schindler, Julio T Barreiro, Michael Chwalla, Daniel Nigg, William A Coish, Maximilian Harlander, Wolfgang Hänsel, Markus Hennrich, and Rainer Blatt. 14-qubit entanglement: Creation and coherence. *Physical Review Letters*, 106(13):130506, 2011.

[8] Hyungjoon Cho, Thaddeus D Ladd, Jonathan Baugh, David G Cory, and Chandrasekhar Ramanathan. Multispin dynamics of the solid-state nmr free induction decay. *Physical Review B*, 72(5):054427, 2005.

[9] Christopher Ferrie and Osama Moussa. Robust and efficient in situ quantum control. *Physical Review A*, 91(5):052306, 2015.

[10] John Cavanagh, Wayne J Fairbrother, Arthur G Palmer III, and Nicholas J Skelton. *Protein NMR spectroscopy: principles and practice*. Elsevier, 1995.

[11] R Laflamme, E Knill, DG Cory, EM Fortunato, T Havel, C Miquel, R Martinez, C Negrevergne, G Ortiz, MA Pravia, et al. Introduction to nmr quantum information processing. *arXiv preprint quant-ph/0207172*, 2002.

[12] Ivan Oliveira, Roberto Sarthour Jr, Tito Bonagamba, Eduardo Azevedo, and Jair CC Freitas. *NMR quantum information processing*. Elsevier, 2011.

[13] Viswanathan V Krishnan and Nagarajan Murali. Radiation damping in modern nmr experiments: progress and challenges. *Progress in nuclear magnetic resonance spectroscopy*, 68:41, 2013.

[14] David G Cory, Amr F Fahmy, and Timothy F Havel. Ensemble quantum computing by nmr spectroscopy. *Proceedings of the National Academy of Sciences*, 94(5):1634–1639, 1997.

[15] Neil A Gershenfeld and Isaac L Chuang. Bulk spin-resonance quantum computation. *science*, 275(5298):350–356, 1997.

[16] Arthur Schweiger and Gunnar Jeschke. *Principles of pulse electron paramagnetic resonance*. Oxford University Press on Demand, 2001.

[17] Clive Emary, Neill Lambert, and Franco Nori. Leggett garg inequalities. *Reports on Progress in Physics*, 77(1):016001, Dec 2013.

[18] George C Knee, Kosuke Kakuyanagi, Mao-Chuang Yeh, Yuichiro Matsuzaki, Hiraku Toida, Hiroshi Yamaguchi, Shiro Saito, Anthony J Leggett, and William J Munro. A strict experimental test of macroscopic realism in a superconducting flux qubit. *Nature communications*, 7:13253, 2016.

[19] OJE Maroney. Detectability, invasiveness and the quantum three box paradox. *arXiv preprint arXiv:1207.3114*, 2012.

[20] Mao-Chung Yeh. *, PhD thesis, University of of Illinois at Urbana-Champaign*. 2016.

[21] Gerhart Lüders. Concerning the state-change due to the measurement process. *Annalen der Physik*, 15(9):663–670, 2006.

[22] John Von Neumann. *Mathematical foundations of quantum mechanics: New edition*. Princeton university press, 2018.

[23] Agustin Palacios-Laloy, François Mallet, François Nguyen, Patrice Bertet, Denis Vion, Daniel Esteve, and Alexander N Korotkov. Experimental violation of a bell's inequality in time with weak measurement. *Nature Physics*, 6(6):442, 2010.

[24] Neill Lambert, Robert Johansson, and Franco Nori. Macrorealism inequality for optoelectromechanical systems. *Phys. Rev. B*, 84:245421, Dec 2011.

[25] Jin-Shi Xu, Chuan-Feng Li, Xu-Bo Zou, and Guang-Can Guo. *Sci. Rep.*, 1:101, 2011.

[26] M. E. Goggin, M. P. Almeida, M. Barbieri, B. P. Lanyon, J. L. O'Brien, A. G. White, and G. J. Pryde. *Proc. Natl. Acad. Sci. USA*, 108:1256, 2011.

[27] J. Dressel, C. J. Broadbent, J. C. Howell, and A. N. Jordan. Experimental violation of two-party leggett-garg inequalities with semiweak measurements. *Phys. Rev. Lett.*, 106:040402, Jan 2011.

[28] Vikram Athalye, Soumya Singha Roy, and T. S. Mahesh. Investigation of the leggett-garg inequality for precessing nuclear spins. *Phys. Rev. Lett.*, 107:130402, Sep 2011.

[29] A. M. Souza, I. S. Oliveira, and R. S. Sarthour. *New J. Phy.*, 13:053023, 2011.

[30] Y. Suzuki, M. Iinuma, and H. F. Hofmann. *New J. Phys.*, 14:103022, 2012.

[31] Sun Yong-Nan, Zou Yang, Ge Rong-Chun, Tang Jian-Shun, and Li Chuan-Feng. Violation of leggett—garg inequalities in single quantum dots. *Chinese Physics Letters*, 29(12):120302, 2012.

[32] Zong-Quan Zhou, Susana F Huelga, Chuan-Feng Li, and Guang-Can Guo. Experimental detection of quantum coherent evolution through the violation of leggett-garg-type inequalities. *Physical review letters*, 115(11):113002, 2015.

[33] George C. Knee, Stephanie Simmons, Erik M. Gauger, John J.L. Morton, Helge Riemann, Nikolai V. Abrosimov, Peter Becker, Hans-Joachim Pohl, Kohei M. Itoh, Mike L.W. Thewalt, Andrew G. Briggs, and Benjamin C. Simon. Violation of a leggett-garg inequality with ideal non-invasive measurements. *Nat Comms*, 3:606, Jan 2012.

[34] Hemant Katiyar, Abhishek Shukla, K Rama Koteswara Rao, and TS Mahesh. Violation of entropic leggett-garg inequality in nuclear spins. *Physical Review A*, 87(5):052102, 2013.

[35] Carsten Robens, Wolfgang Alt, Dieter Meschede, Clive Emary, and Andrea Alberti. Ideal negative measurements in quantum walks disprove theories based on classical trajectories. *Phys. Rev. X*, 5:011003, Jan 2015.

[36] Richard E. George, Lucio M. Robledo, Owen J. E. Maroney, Machiel S. Blok, Hannes Bernien, Matthew L. Markham, Daniel J. Twitchen, John J. L. Morton, G. Andrew D. Briggs, and Ronald Hanson. Opening up three quantum boxes causes classically undetectable wavefunction collapse. *Proceedings of the National Academy of Sciences*, 110(10):3777–3781, 2013.

[37] Ramamurti Shankar. *Principles of quantum mechanics.* Springer Science & Business Media, 2012.

[38] David G Cory, Mark D Price, and Timothy F Havel. Nuclear magnetic resonance spectroscopy: An experimentally accessible paradigm for quantum computing. *Physica D: Nonlinear Phenomena*, 120(1-2):82–101, 1998.

[39] Evan M. Fortunato *et. al.* Design of strongly modulating pulses to implement precise effective hamiltonians for quantum information processing. *The Journal of Chemical Physics*, 116(17):7599–7606, 2002.

[40] T. S. Mahesh and Dieter Suter. Quantum-information processing using strongly dipolar coupled nuclear spins. *Phys. Rev. A*, 74:062312, Dec 2006.

[41] Garett M Leskowitz and Leonard J Mueller. State interrogation in nuclear magnetic resonance quantum-information processing. *Physical Review A*, 69(5):052302, 2004.

[42] Laforest, Martin. Error characterization and quantum control benchmarking in liquid state nmr using quantum information processing techniques, 2008.

[43] N. C. Menicucci and Carlton M. Caves. Local realistic model for the dynamics of bulk-ensemble nmr information processing. *Physical Review Letters*, 88(16), Apr 2002.

[44] Navin Khaneja, Timo Reiss, Cindie Kehlet, Thomas Schulte-Herbrüggen, and Steffen J Glaser. Optimal control of coupled spin dynamics: design of nmr pulse sequences by gradient ascent algorithms. *J. Magn. Reson.*, 172(2):296–305, 2005.

[45] CA Ryan, C Negrevergne, M Laforest, E Knill, and R Laflamme. Liquid-state nuclear magnetic resonance as a testbed for developing quantum control methods. *Phys. Rev. A*, 78(1):012328, 2008.

[46] Yingjie Zhang, Colm A Ryan, Raymond Laflamme, and Jonathan Baugh. Coherent control of two nuclear spins using the anisotropic hyperfine interaction. *Phys. Rev. Lett.*, 107(17):170503, 2011.

[47] G Waldherr, Y Wang, S Zaiser, M Jamali, T Schulte-Herbrüggen, H Abe, T Ohshima, J Isoya, JF Du, P Neumann, et al. Quantum error correction in a solid-state hybrid spin register. *Nature*, 506(7487):204–207, 2014.

[48] Florian Dolde, Ville Bergholm, Ya Wang, Ingmar Jakobi, Boris Naydenov, Sébastien Pezzagna, Jan Meijer, Fedor Jelezko, Philipp Neumann, Thomas Schulte-Herbrüggen, et al. High-fidelity spin entanglement using optimal control. *Nature communications*, 5:3371, 2014.

[49] F Motzoi, JM Gambetta, P Rebentrost, and Frank K Wilhelm. Simple pulses for elimination of leakage in weakly nonlinear qubits. *Phys. Rev. Lett.*, 103(11):110501, 2009.

[50] Daniel J Egger and Frank K Wilhelm. Optimized controlled-z gates for two superconducting qubits coupled through a resonator. *Supercond. Sci. Technol.*, 27(1):014001, 2013.

[51] V Nebendahl, H Häffner, and CF Roos. Optimal control of entangling operations for trapped-ion quantum computing. *Phys. Rev. A*, 79(1):012312, 2009.

[52] Philipp Schindler, Julio T Barreiro, Thomas Monz, Volckmar Nebendahl, Daniel Nigg, Michael Chwalla, Markus Hennrich, and Rainer Blatt. Experimental repetitive quantum error correction. *Science*, 332(6033):1059–1061, 2011.

[53] Patrick Rebentrost, Maria Schuld, Francesco Petruccione, and Seth Lloyd. Quantum gradient descent and newton's method for constrained polynomial optimization. *arXiv:1612.01789*, 2016.

[54] R Vijay, Chris Macklin, DH Slichter, SJ Weber, KW Murch, Ravi Naik, Alexander N Korotkov, and Irfan Siddiqi. Stabilizing rabi oscillations in a superconducting qubit using quantum feedback. *Nature*, 490(7418):77–80, 2012.

[55] Masashi Hirose and Paola Cappellaro. Coherent feedback control of a single qubit in diamond. *Nature*, 532(7597):77–80, 2016.

[56] Dawei Lu, Hang Li, Denis-Alexandre Trottier, Jun Li, Aharon Brodutch, Anthony P Krismanich, Ahmad Ghavami, Gary I Dmitrienko, Guilu Long, Jonathan Baugh, et al.

Experimental estimation of average fidelity of a clifford gate on a 7-qubit quantum processor. *Phys. Rev. Lett.*, 114(14):140505, 2015.

[57] Andrew J Daley. Quantum trajectories and open many-body quantum systems. *Adv. Phys.*, 63(2):77–149, 2014.

[58] Eduardo Mascarenhas, Hugo Flayac, and Vincenzo Savona. Matrix-product-operator approach to the nonequilibrium steady state of driven-dissipative quantum arrays. *Phys. Rev. A*, 92(2):022116, 2015.

[59] S Lloyd and S Montangero. Information theoretical analysis of quantum optimal control. *Phys. Rev. Lett.*, 113(1):010502, 2014.

[60] John Preskill. Quantum computing and the entanglement frontier. *arXiv:1203.5813*, 2012.

[61] Hui Wang, Yu He, Yu-Huai Li, Zu-En Su, Bo Li, He-Liang Huang, Xing Ding, Ming-Cheng Chen, Chang Liu, Jian Qin, et al. High-efficiency multiphoton boson sampling. *Nat. Photon.*, 11(6):361–365, 2017.

[62] Chao Song, Kai Xu, Wuxin Liu, Chuiping Yang, Shi-Biao Zheng, Hui Deng, Qiwei Xie, Keqiang Huang, Qiujiang Guo, Libo Zhang, et al. 10-qubit entanglement and parallel logic operations with a superconducting circuit. *arXiv:1703.10302*, 2017.

[63] Ashley Montanaro. Quantum algorithms: an overview. *npj Quantum Information*, 2:15023, 2016.

[64] Constantin Brif, Raj Chakrabarti, and Herschel Rabitz. Control of quantum phenomena: past, present and future. *New Journal of Physics*, 12(7):075008, 2010.

[65] Steffen J Glaser, Ugo Boscain, Tommaso Calarco, Christiane P Koch, Walter Köckenberger, Ronnie Kosloff, Ilya Kuprov, Burkhard Luy, Sophie Schirmer, Thomas Schulte-Herbrüggen, et al. Training schrödinger's cat: quantum optimal control. *The European Physical Journal D*, 69(12):279, 2015.

[66] Rami Barends, Julian Kelly, Anthony Megrant, Andrzej Veitia, Daniel Sank, Evan Jeffrey, Ted C White, Josh Mutus, Austin G Fowler, Brooks Campbell, et al. Superconducting quantum circuits at the surface code threshold for fault tolerance. *Nature*, 508(7497):500, 2014.

[67] M Veldhorst, JCC Hwang, CH Yang, AW Leenstra, Bob de Ronde, JP Dehollain, JT Muhonen, FE Hudson, Kohei M Itoh, A Morello, et al. An addressable quantum dot qubit with fault-tolerant control-fidelity. *Nature nanotechnology*, 9(12):981, 2014.

[68] Xing Rong, Jianpei Geng, Fazhan Shi, Ying Liu, Kebiao Xu, Wenchao Ma, Fei Kong, Zhen Jiang, Yang Wu, and Jiangfeng Du. Experimental fault-tolerant universal quantum gates with solid-state spins under ambient conditions. *Nature communications*, 6:8748, 2015.

[69] Alejandro Bermudez, Xiaosi Xu, Ramil Nigmatullin, Joe O'Gorman, Vlad Negnevitsky, Philipp Schindler, Thomas Monz, UG Poschinger, Cornelius Hempel, J Home, et al. Assessing the progress of trapped-ion processors towards fault-tolerant quantum computation. *Physical Review X*, 7(4):041061, 2017.

[70] Thomas Kaufmann, Timothy J Keller, John M Franck, Ryan P Barnes, Steffen J Glaser, John M Martinis, and Songi Han. Dac-board based x-band epr spectrometer with arbitrary waveform control. *Journal of Magnetic Resonance*, 235:95–108, 2013.

[71] Simon Gustavsson, Olger Zwier, Jonas Bylander, Fei Yan, Fumiki Yoshihara, Yasunobu Nakamura, Terry P Orlando, and William D Oliver. Improving quantum gate fidelities by using a qubit to measure microwave pulse distortions. *Physical Review Letters*, 110(4):040502, 2013.

[72] Guanru Feng, Joel J Wallman, Brandon Buonacorsi, Franklin H Cho, Daniel K Park, Tao Xin, Dawei Lu, Jonathan Baugh, and Raymond Laflamme. Estimating the coherence of noise in quantum control of a solid-state qubit. *Physical Review Letters*, 117(26):260501, 2016.

[73] Murphy Yuezhen Niu, Sergio Boixo, Vadim N Smelyanskiy, and Hartmut Neven. Universal quantum control through deep reinforcement learning. In *AIAA Scitech 2019 Forum*, page 0954, 2019.

[74] Jun Li, Xiaodong Yang, Xinhua Peng, and Chang-Pu Sun. Hybrid quantum-classical approach to quantum optimal control. *Physical Review Letters*, 118(15):150503, 2017.

[75] Dawei Lu, Keren Li, Jun Li, Hemant Katiyar, Annie Jihyun Park, Guanru Feng, Tao Xin, Hang Li, Guilu Long, Aharon Brodutch, et al. Enhancing quantum control by bootstrapping a quantum processor of 12 qubits. *npj Quantum Information*, 3(1):45, 2017.

[76] Daniel J Egger and Frank K Wilhelm. Adaptive hybrid optimal quantum control for imprecisely characterized systems. *Physical Review Letters*, 112(24):240503, 2014.

[77] Julian Kelly, R Barends, B Campbell, Y Chen, Z Chen, B Chiaro, A Dunsworth, Austin G Fowler, I-C Hoi, E Jeffrey, et al. Optimal quantum control using randomized benchmarking. *Physical Review Letters*, 112(24):240504, 2014.

[78] MA Rol, CC Bultink, TE O'Brien, SR De Jong, LS Theis, Xiang Fu, F Luthi, RFL Vermeulen, JC de Sterke, Alessandro Bruno, et al. Restless tuneup of high-fidelity qubit gates. *Physical Review Applied*, 7(4):041001, 2017.

[79] Re-Bing Wu, Bing Chu, David H Owens, and Herschel Rabitz. Data-driven gradient algorithm for high-precision quantum control. *Physical Review A*, 97(4):042122, 2018.

[80] David L Goodwin, William K Myers, Christiane R Timmel, and Ilya Kuprov. Feedback control optimisation of esr experiments. *Journal of Magnetic Resonance*, 297:9–16, 2018.

[81] Shai Machnes, Elie Assémat, David Tannor, and Frank K Wilhelm. Tunable, flexible, and efficient optimization of control pulses for practical qubits. *Physical Review Letters*, 120(15):150401, 2018.

[82] Jonathan S Hodges, Jamie C Yang, Chandrasekhar Ramanathan, and David G Cory. Universal control of nuclear spins via anisotropic hyperfine interactions. *Physical Review A*, 78(1):010303, 2008.

[83] Daniel K Park, Guanru Feng, Robabeh Rahimi, Stéphane Labruyère, Taiki Shibata, Shigeaki Nakazawa, Kazunobu Sato, Takeji Takui, Raymond Laflamme, and Jonathan Baugh. Hyperfine spin qubits in irradiated malonic acid: heat-bath algorithmic cooling. *Quantum Information Processing*, 14(7):2435–2461, 2015.

[84] David Slepian. Prolate spheroidal wave functions, fourier analysis, and uncertainty—v: The discrete case. *Bell System Technical Journal*, 57(5):1371–1430, 1978.

[85] Dennis Lucarelli. Quantum optimal control via gradient ascent in function space and the time-bandwidth quantum speed limit. *Physical Review A*, 97(6):062346, 2018.

[86] David Slepian. Some comments on fourier analysis, uncertainty and modeling. *SIAM review*, 25(3):379–393, 1983.

[87] Daniel K Park, Guanru Feng, Robabeh Rahimi, Jonathan Baugh, and Raymond Laflamme. Randomized benchmarking of quantum gates implemented by electron spin resonance. *Journal of Magnetic Resonance*, 267:68–78, 2016.

[88] Einar Sagstuen, Anders Lund, Yoshiteru Itagaki, and Jean Maruani. Weakly coupled proton interactions in the malonic acid radical: Single crystal endor analysis and epr simulation at microwave saturation. *The Journal of Physical Chemistry A*, 104(27):6362–6371, 2000.

[89] James C Spall et al. Multivariate stochastic approximation using a simultaneous perturbation gradient approximation. *IEEE transactions on automatic control*, 37(3):332–341, 1992.

[90] Payman Sadegh and James C Spall. Optimal random perturbations for stochastic approximation using a simultaneous perturbation gradient approximation. *IEEE Transactions on Automatic Control*, 43(10):1480–1484, 1998.

[91] Kosuke Mitarai, Makoto Negoro, Masahiro Kitagawa, and Keisuke Fujii. Quantum circuit learning. *Physical Review A*, 98(3):032309, 2018.